POLITECNICO DI TORINO

Corso di Laurea Magistrale in Ingegneria Energetica e Nucleare

and

KTH ROYAL INSTITUTE OF TECHNOLOGY

MSc Sustainable Energy Engineering

Master of Science Thesis

Design and Optimization of a Sodium-Molten Salt Heat Exchanger for Concentrating Solar Power Applications

Advisors:
Prof. Laura Savoldi
Dr. Rafael Guédez
Dr. John Pye
Prof. Roberto Zanino

Candidate:
Salvatore Guccione

Academic year 2019/2020

Authors

Salvatore Guccione <salvatoreguccione@yahoo.com>

Place for Project

The Australian National University, Canberra, Australia
Politecnico di Torino, Turin, Italy
KTH Royal Institute of Technology, Stockholm, Sweden

Supervisors

Dr. Rafael Guédez, KTH Royal Institute of Technology

Prof. Laura Savoldi, Politecnico di Torino

Prof. Roberto Zanino, Politecnico di Torino

Dr. John Pye, The Australian National University

To my Family,
the fuel of my life.

Acknowledgements

I would like to thank The Australian National University and the Solar Thermal Group and, particularly, my supervisor Dr. John Pye for his professionalism, availability and help throughout the realization of the present work.
I am sincerely thankful to my advisors, Prof. Laura Savoldi and Prof. Roberto Zanino, for the opportunity, constant help and teachings, but also for the guidance and the wise and precious pieces of advice. I would like to thank my advisor Dr. Rafael Guedez for all the support, valuable suggestions and technical help.
I am also grateful to the ERASMUS+ program and the Australian Solar Thermal Research Institute for providing the financial support to carry out this international experience in Sweden and in Australia.

I should like to thank my family for being my strength and my shield during the challenges of these years. I am grateful to my brother for always being there for me as a friend, helpful and supportive. I am forever thankful to my parents for their unconditional love and for giving me the opportunities and experiences that have made me who I am.

I am grateful to my grandma, to my uncles, and to my cousins which, with their love, has accompanied and supported me in this journey. I say a special thank you to my grandparents who I can no longer hug.

I am sincerely thankful to my dear friend Rosario, who taught me what true friendship is. Thank you for being a loyal friend, my reference point, always at my side.

I convey special thank to my team mates and my friends, Alessandro, Antonio B., Antonio G., and Luca. University years would not have been the same without you. Thank you for always been there to help me, to support morally and to give scientific suggestions between several beers and carbonara pasta.

I am grateful to Vincenzo both for his trustworthy friendship and for his inspiring professionalism. Thank you for your suggestions and for filling my time in Stockholm with persuasive craziness.

Many thanks to my dear friends Giuseppe, Salvatore, Marianna, Giorgia C., and Giorgia R. who have accompanied me also along this important phase of my life. Thank you for your support, your being present and for our strong bond.

I am thankful to Davide and Gabriele, whose exasperated attention to details taught me a lot, while driving me crazy. Thank you for being such trusted and honest friends.

Thank you to all the people that made my time at KTH an amazing and unforgettable experience. Particularly, I thank to my wonderful friends: Marta, Simone, Pietro, Alex, and Mara.

I wish to say a special thank you to Letizia, Claudio, Virginia and Pietro for their empathy, for being supportive and for their continuous affection.

In the end, my deep and sincere gratitude to my touchstone, to my strength: Enrica. Thank you for believing in me and for standing by me regardless the distance between us. Thank you for encouraging me to face successfully the major challenges of these years. This journey would not have been so satisfying if not for you.

Abstract

Concentrating Solar Power (CSP) is one of the most promising renewable energy-based electricity generation technologies to deal with the increasing demand of power consumption and environmental sustainability. With the aim of achieving the 2020 SunShot cost target for CSP of 60 USD/MWh, the United States Department of Energy presented, in May 2018, the Gen3 CSP initiative. In particular, the CSP Gen3 Liquid-Phase Pathway proposes to design a CSP system adopting liquid sodium as Heat Transfer Fluid (HTF) in the receiver, advanced high-temperature molten chloride salt as storage fluid and supercritical CO_2 (sCO_2) Brayton cycle as power cycle.

Within this framework, the aim of this master thesis was to design the sodium-chloride salt Heat Exchanger (HX) by developing both a heat exchanger model and a sodium-salt-sCO_2 system model.

To pursue these purposes, a completely new Modelica-based *HX* model was developed and added to the *SolarTherm* library. Furthermore, as an extension of earlier models, the sodium-salt-sCO_2 CSP system (*NaSaltsCO2System*) was implemented in *SolarTherm*, by incorporating the HX model and linking it with other new and existing component models. As for the HX, a general model was developed for shell and tube heat exchangers, based on the TEMA guidelines, with the possibility of being customized in terms of media adopted, constraints, boundary conditions, and correlations. The model performs an optimization in order to select the internal geometry configuration that optimizes a user-defined objective-function. By employing the implemented HX model in the *NaSaltsCO2System*, the sodium-salt heat exchanger was designed aiming at minimizing the Levelized Cost of Electricity (LCOE), providing a complete geometry description, and an estimation of the performances and costs. The resulting *NaSaltsCO2System* model was found to be robust and able to perform annual simulations that allowed to estimate the energy performances of the CSP plant, as well as the LCOE. Considering the sodium-salt-sCO_2

CSP system characterized by a receiver capacity of 543 MWth, 12 hours of Thermal Energy Storage (TES), and a 100 MWe power block, the LCOE resulted equal to 72.66 USD/MWh. The sodium-salt HX design that minimizes the LCOE resulted in a single-shell/single tube pass configuration, with vertical alignment, characterized by an overall height of 15 m, and a shell diameter of 1.8 m. It represents the 3.2% of the total capital cost of the plant. An interesting system-level optimization was then carried out on the combined receiver-heat exchanger block. It regarded the variation of the Log Mean Temperature Difference (LMTD) of the HX and highlighted the possibility to drop the LCOE down to 68.54 USD/MWh. The techno-economic investigations and the sensitivity analysis showed the flexibility and robustness of the HX model, as well as the importance of the *NaSaltsCO2System*. The latter lays the groundwork to explore potential improvements of this new generation of CSP systems, which can play a fundamental role in the future global energy mix.

Keywords

Concentrating solar power (CSP), liquid sodium, advanced molten salt, chloride salt, heat exchanger (HX), shell and tube, CSP Gen3 Liquid-Phase Pathway, Modelica

Abstract

Termisk solkraft (CSP) är en av de mest lovande elproduktionsteknologierna baserade på förnybar energi. Den kan bidra till hanteringen av den ökande efterfrågan på energi och miljömässig hållbarhet. I syfte att uppnå 2020 SunShot-kostnadsmålet för CSP på 60 USD/MWh presenterade USA:s energidepartement Gen3 CSP-initiativet. I synnerhet föreslår CSP Gen Liquid-Phase Pathway att utforma ett CSP-system som använder flytande natrium som värmeöverföringsvätska i mottagaren, smält kloridsalt med hög temperatur som lagringsvätska, samt superkritisk CO2 (sCO2) Brayton-cykel som kraftcykel. Syftet för detta examensarbete var att utforma natriumkloridsaltets primära värmeväxlare genom att utveckla både en värmeväxlarmodell (HX) modell och en natriumsalt-sCO2-systemmodell. För att fullfölja dessa syften utvecklades HX-modellen först, sedan implementerades natrium-salt-sCO2 CSP-systemet *NaSaltsCO2System*. Båda verktygen utvecklades med hjälp av Modelica som programmeringsspråk. De finns nu tillgängliga i det öppna *SolarTherm*-biblioteket. När det gäller HX utvecklades en allmän modell för skal- och rörvärmeväxlare med möjligheten att anpassas när det gäller antagna medium, begränsningar, gränsvillkor och korrelationer. Dessutom utförde modellen en optimering för att välja den interna geometri-konfigurationen som optimerar en användardefinierad objektiv-funktion. Genom att använda den implementerade HX-modellen i *NaSaltsCO2System* designades natriumsalt-värmeväxlaren, vilket gav en fullständig konfiguration-beskrivning och en uppskattning av prestanda och kostnader. Den utvecklade *NaSaltsCO2System*-modellen visade sig vara robust och kapabel till att utföra simuleringar på årsbasis. Detta gjorde det möjligt att uppskatta CSP-anläggningens energiprestanda samt LCOE. Det utvecklade natrium-salt-sCO2 CSP-systemet som kännetecknas av en mottagarkapacitet på 543 MWth, 12 timmars TES och ett 100 MWe power block, resulterade i en LCOE på 72.66 USD/MWh. Natrium-salt HX-konstruktionen som minimerade LCOE resulterade i

en enskalig/enkel rörpassningskonfiguration, med vertikal inriktning, kännetecknad av en total höjd av 15 m och en skaldiameter på 1.8 m. Det motsvarade 3.2% av anläggningens totala kapitalkostnad. Den mest intressanta systemoptimeringen genomfördes på det kombinerade blocket bestående av mottagare och värmeväxlare. Den behandlade variationen av HX:s LMTD och framhöll möjligheten att sänka LCOE till 68.54 USD/MWh. De teknisk-ekonomiska undersökningarna och känslighetsanalysen visade flexibiliteten och robustheten i HX-modellen, liksom vikten av *NaSaltsCO2System*et. Den senare lägger grunden för att utforska potentiella förbättringar av denna nya generation av CSP-system, som kan spela en grundläggande roll i den framtida globala energimixen.

Nyckelord

Termisk solkraft, CSP, flytande natrium, avancerat smält salt, kloridsalt, värmeväxlare (HX), skal och rör, CSP Gen3 Liquid-Phase Pathway, Modelica

Acronyms

ASME	American Society of Mechanical Engineers
ANU	Australian National University
ASTRI	Australian Solar Thermal Research Institute
BCs	Boundary Conditions
CEPCI	Chemical Engineering Plant Cost Index
CSP	Concentrating Solar Power
DNI	Direct Normal Irradiance
FBR	Fast Breeder Reactors
HTC	Heat Transfer Coefficient
HTF	Heat Transfer Fluid
HX	Heat Exchanger
IHX	Intermediate Heat Exchanger
JSFR	Japan Sodium-cooled Fast Reactor
MAPS	Madras Atomic Power Station
LCOE	Levelized Cost of Electricity
LMTD	Log Mean Temperature Difference
NREL	National Renewable Energy Laboratory
PV	Photo-Voltaic
SAM	System Advisor Model
SG	Steam Generator
SM	Solar Multiple
STHE	Shell and Tube Heat Exchanger
TAC	Total Annualized Cost
TEMA	Tubular Exchanger Manufacturers Association
TES	Thermal Energy Storage
USD	United States Dollars

Contents

Chapter 1

Introduction

Nowadays, the development of renewable energy technologies for power production represents a focal interest point for nations worldwide. The main driving force are the climate change and the drawbacks associated with consumption of fossil fuels. In the last decade, the Paris agreement signed a global engagement to take climate action and to propose a more sustainable energy development scenario. In the transition from fossil-fuel-based technologies to sustainable and renewable ones, solar energy plays a fundamental role.

Currently, the solar energy sector is dominated by PV technology because it represents the most cost-efficient way to convert solar energy into electricity. Concentrating Solar Power (CSP) is the other leading solar technology and it shows lots of potential to meet a part of future energy demand and that could play a promising role in helping to reach ambitious climate protection goals. Its strong-point is the higher levels of stability, dispatchability and increased duration of energy output that can be achieved incorporating the thermal energy storage. Among different CSP technologies, the solar thermal power plant with central receiver and TES is expected to be the key technology of the next future [1]. Indeed, central tower systems, like dish systems, can reach significantly higher temperatures compared to the parabolic trough and linear Fresnel, resulting in higher thermal-to-electric conversion efficiency in the power block and, therefore, in a reduction of the TES cost [2].

The state-of-the-art solar tower power plants often use molten nitrate salt (Solar salt) as HTF, that is heated up in the receiver and stored in a direct two tank salt system. The principal limit of solar salt used in the current generation plants concerns their maximum operating temperature (up to 565°C). Accordingly, conventional Rankine

cycle with steam turbine is generally adopted.

In May 2018, the United States Department of Energy - Solar Energy Technologies Office presented the Gen3 CSP initiative. The main goal of this project is to improve concentrating solar thermal power technology to enable the industry to achieve the 2020 SunShot cost target for CSP of 60 USD/MWh [3]. In particular, the CSP Gen3 Liquid-Phase Pathway proposes to use liquid sodium as HTF in the receiver, advanced high-temperature molten chloride salt as storage fluid and supercritical CO2 (sCO2) Brayton cycle as power cycle.

The big advantages of liquid sodium are the higher maximum acceptable temperatures (98-890°C, melting - boiling at atmospheric pressure) and the high heat conductivity that leads to very high heat transfer coefficients compared to Solar Salt. High conductivity and high heat transfer means that the receiver can operate at high solar heat fluxes, while maintaining an acceptable temperature difference between the absorber inner surface and the fluid. High conductivity also alleviates thermal stress issues by reducing front-to-back tube temperature difference [4]. Consequently, there is the possibility to reduce the size, resulting in cheaper and more thermally efficient receivers. On the contrary, the main disadvantage of sodium concerns its reactivity with water and oxygen which could result in fires. Hence, safety guidelines for both construction and operating phases need to be followed. Since the temperature of both the receiver and the hot storage can be raised, sCO2 power cycles can replace conventional steam Rankine cycles, improving the power conversion efficiency.

The work presented herein is a contribution to the CSP Gen3 Liquid Pathway, Sodium Pathway. It was carried out at the Australian National University (ANU), in collaboration with the ANU Solar Thermal group and the Australian Solar Thermal Research Institute (ASTRI). The aim of this work is to propose a suitable design for the sodium-chloride salt heat exchanger. Using the object-oriented Modelica programming language, a heat exchanger model is built and integrated in the open source *SolarTherm* library. In addition, the sodium-chloride-salt-sCO2 CSP system model (NaSaltsCO2System) is implemented in order to evaluate the annual energy performances and the expected LCOE value. In addition, a sensitivity analysis on the HX cost is also carried out to further understand how it significantly affects the total investment plant cost and its relative LCOE.

1.1 Aim of the study

The aim of this thesis project is to design a suitable heat exchanger for the Gen3 sodium-molten chloride salt HX. A model of the heat exchanger and a model of the sodium-salt-sCO2 CSP system are expected to be implemented using Modelica as programming language. Techno-economic optimisations are carried out to propose the HX design that minimize the plant LCOE. In summary, the specific objectives of the thesis are:

- To develop a heat exchanger model that fulfils the following tasks:
  - To design a heat exchanger based on nominal conditions;
  - To simulate the performance of the heat exchanger during operation;
- To develop a sodium-salt-sCO2 CSP system model;
- To determine an optimum sodium-salt HX design that minimizes the LCOE of the CSP system;
- To investigate the impact of the HX on the CSP plant as function of techno-economic parameters.

1.2 Methodology

The present research work is structured as follows. A literature review is presented about working principle and state-of-the-art of CSP systems, previous experiences with sodium or molten salt heat exchangers, and high-efficient power cycles. Based on the theoretical background, the heat exchanger type is selected and the important aspects that need to be taken into account for a good design are pointed out. The following chapters, *Heat Exchanger Model* and *Sodium-Salt-sCO2 CSP system model* shows the assumptions, methodology and design strategy adopted to implement the model of the HX and of the multi-component CSP system. As a result of a component-level optimization, a proposed design of the sodium-salt heat exchanger is presented in the chapter *Design Sodium-Salt HX*. After this chapter, the system-level investigations and the sensitivity analysis on the HX cost are shown. In the end, the conclusions of the work are presented.

Chapter 2

Theoretical background

2.1 Concentrating Solar Power Technology

Concentrating solar power (CSP) is one of the most promising renewable energy-based electricity generation technologies to deal with the increasing demand of power consumption and environmental sustainability. Among many renewable energy systems, such as Photo-Voltaic (PV) or wind turbines farms, CSP stands out for the possibility to incorporate a TES that decouples electricity production from the intermittent solar resource availability. On the contrary, one of the major obstacles for the commercialization of CSP technology is the relatively high cost of the electricity generation.

CSP technologies can be distinguished in two macro-categories: line focusing and point focusing systems. *Parabolic Trough* and *Linear Fresnel* represent two major types of line focusing systems, while *Parabolic Dish* and *Power Tower* are point focusing systems. Solar thermal power plant with central receiver and TES is expected to be one key technology in future [1] thanks to the high operating temperatures, resulting in high thermal-to-electric conversion efficiencies in the power block.

The basic concept for a solar power tower technology is shown in figure 2.1.1. The heliostats, equipped with double axis tracking system, follow the movement of the sun and reflect the sunlight to the receiver to produce high temperature heat. The energy in the fluid can be stored in tanks and can be used in a power block to generate electricity.

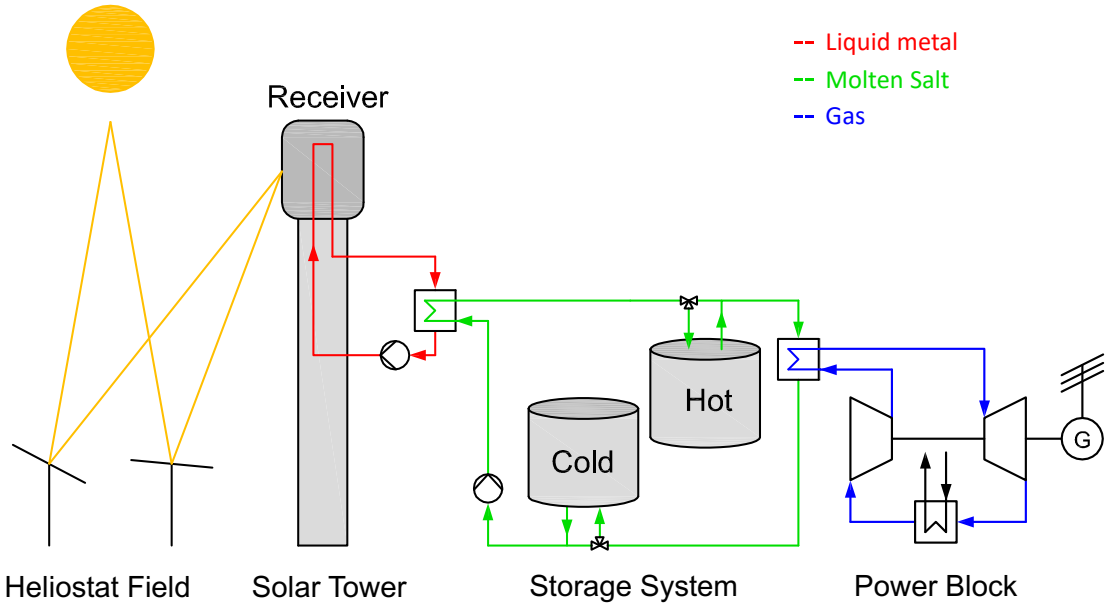

Figure 2.1.1: Solar thermal power plant with central receiver representation [5]

State-of-the-art solar power plants often use molten nitrate salts (Solar salt) as HTF, that are heated up in the receiver and stored in a direct two tank salt system. The principal limit of solar salt utilized in the current generation plants regards their maximum operating temperature. According to [6], they are chemically stable up to 600°C, but due to corrosion concerns the maximum temperature is limited to 565 °C in commercial plants. Therefore, conventional Rankine cycle with steam turbine is generally adopted with this HTF.

For the purpose of making CSP technology more competitive, respect to the state-of-the-art, further cost reduction is necessary. In particular, in order to reduce the LCOE, basically, two options can be identified:

- Reduce the investment cost of the plant;
- Increase the overall efficiency of the plant;

The use of liquid metals as HTF in the solar receiver acts on both options to reduce the LCOE. The big advantages of liquid metals are the higher maximum acceptable temperatures (figure 2.1.2a) and the high heat conductivity, that leads to very high heat transfer coefficients compared to Solar Salt (figure 2.1.2b).

Although liquid metals are very attractive as HTF, due to their low heat capacity and high material cost, they are less suitable as storage media. Hence, direct one tank sodium system, generally, is not cost-efficient. Alternatively, as shown in the system

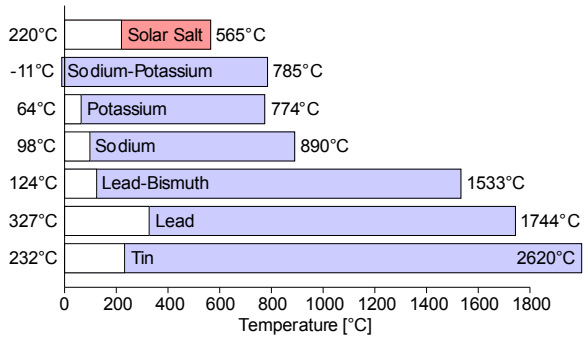

(a) liquid state temperature range

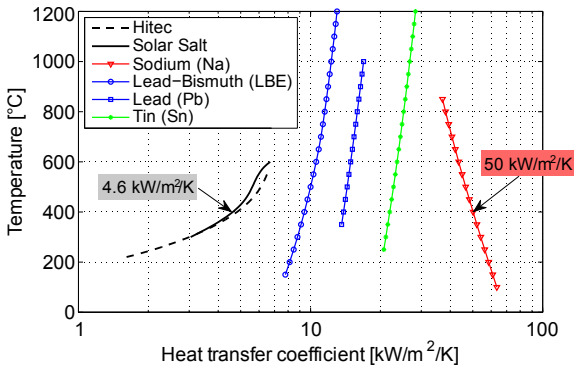

(b) Heat transfer coefficient for tubes with D = 12 mm, u = 1 m/s and tube roughness = 0.1 mm

Figure 2.1.2: Acceptable temperature range (a) and heat transfer coefficient (b) for liquid metals and molten salts [5]

in figure 2.1.1, indirect two tank thermal storage with high-temperature molten salts with high thermal stability, acceptable thermo-physical properties, and low cost are preferred.

2.1.1 Advantages and disadvantages of sodium

Among different liquid metal candidates, according to [7], sodium is the most technologically ready due to previous experience concerning materials compatibility and safety issues from nuclear industry. The first advantage of sodium as HTF regards its high temperature range. Indeed, high boiling point make sodium suitable for high-temperature high-efficient energy conversion systems, such as ultra-supercritical steam power cycles (590–620°C) or sCO2 Brayton cycle (>650°C). Moreover, the low melting point minimizes freezing problems and leads to less trace heating compared to solar salt and therefore lower parasitic losses [1].

Another point is that sodium implies no corrosion problems below the boiling point, thus there are no relevant compatibility problems with structural materials. On the contrary, corrosion problems are relevant for salt mixtures [8].

As cited above, the high thermal conductivity is the other big advantage. In particular, for sodium, the thermal conductivity is over 100 times larger than with Solar Salt, resulting in 10 times higher heat transfer coefficients, as shown in figure 2.1.2b.

High conductivity and high heat transfer means that the receiver can operate at high solar heat flux, keeping an acceptable temperature difference between the absorber

inner surface and the fluid. Therefore, receiver size can be reduced, resulting in cheaper and more thermally efficient receivers. Additionally, high conductivity makes the aiming strategy less relevant for sodium compares to molten salts receiver. In the end, according to [4], since high conductivity reduces front-to-back tube temperature difference, thermal stress issues for sodium receivers become less relevant.

The main disadvantage of sodium regards its reactivity with water and oxygen which could result in fires that are difficult to extinguish. In literature, several sodium fires are reported. An emblematic example is the sodium fire on the Plataforma Solar de Almería (DFVLR, 1987). However, mainly thank to the nuclear power sector, a lot of experience was gained in the handling with sodium. Safety operating and construction guidelines are available in order to avoid such accidents and to minimize damage in case of a sodium fire. The fail-drain-principle is one of the most important construction guidelines that plans to drain fast all the liquid sodium into the sump tank, as soon fails are detected.

Currently, nuclear energy is the main field where liquid sodium is involved. The biggest grid-connected fast breeder reactor is the BN-800 in World Nuclear Association (2015) with a power of 864 MWel. For what concerns the solar energy field, in 2015, VastSolar built a grid-connected solar thermal power plant with sodium as HTF.

2.1.2 Advanced high-temperature molten salt

According to [4], fluoride, chloride and carbonate salts are possible candidate for use in CSP plants. In particular, [9] assesses that a ternary chloride salt eutectic mixture of NaCl-KCl-MgCl2 has been identified as a promising thermal storage material for sensible energy storage in CSP systems requiring temperatures above 600°C in a closed tank design. The material cost results significantly lower than conventional 'solar salt'. Nevertheless, material compatibility and corrosion issues are fundamental aspects that need to be taken into account.

2.1.3 High-efficient power block systems

Concerning the power block configuration, supercritical CO2 (sCO2) Brayton cycle is indicated as the future of the thermal to electric conversion technology. This statement is in agreement with several research programs and key international energy stakeholders ([10], [11], [12], [13], and [14]). Supercritical CO2 cycles, traditionally

utilized for application in nuclear power plants, are becoming interesting for CSP applications because they have the potential to drive down the LCOE of the CSP plant. Indeed, using sCO2 cycles, is possible to overcome the temperature limit imposed by standard Rankine cycle, improving the power conversion efficiency in the temperature range of 550–750 °C. Another interesting point of sCO2 power block is their compactness. Compact turbomachinery design implies advantages both from the economic and transient operation points of view [15]. Additionally, high performances are preserved with the scale, avoiding scale-down effects typical of steam cycles. In the end, for what concern safety issues, CO2 is environmental harmless and a corrosion neutral working fluid, implying compatibility with structural material and no other relevant risks. In [16], it is investigated the compatibility of sCO2 cycles with advanced molten salts, resulting in higher power cycle performance with respect to conventional steam cycle.
In conclusion, the potential reduction of cost and increase of conversion efficiency make sCO2 cycles the most promising option when the receiver maximum temperature ranges between 650 °C and 750 °C [17].

2.2 HX Background

According to [18], a heat exchanger is a device in which heat is exchanged between a hot medium and a cold medium. HXs are used extensively and regularly in process and allied industries and represent one of the most important devices of mechanical systems in modern society. The most commonly used type of HX is the shell and tube heat exchanger [19], thanks to their robust geometry construction, easy maintenance, and possible upgrades.
U-tube type HXs are well suited for stable operation loads and minimum temperature changes, typical of continuous operating applications. Nevertheless, in agreement with [20], large-scale CSP plants are characterized by daily system starts/stops operations, by loads fluctuation and consequently by important variations in the heat transfer fluid temperature. Since the latter contribute to unwanted vertical stresses in the tube plates, leakages and needed repairs, shell and tube HX type is not the perfect configuration that fits the CSP plant requirements. In [21], Aalborg CSP presented the header-and-coil heat exchanger type that eliminates the constraints of the fragile tube plate in transient operation, typical of TEMA U-tube HX type. Figure 2.2.1 shows the header-and-coil HX and under construction and a 3D representation.

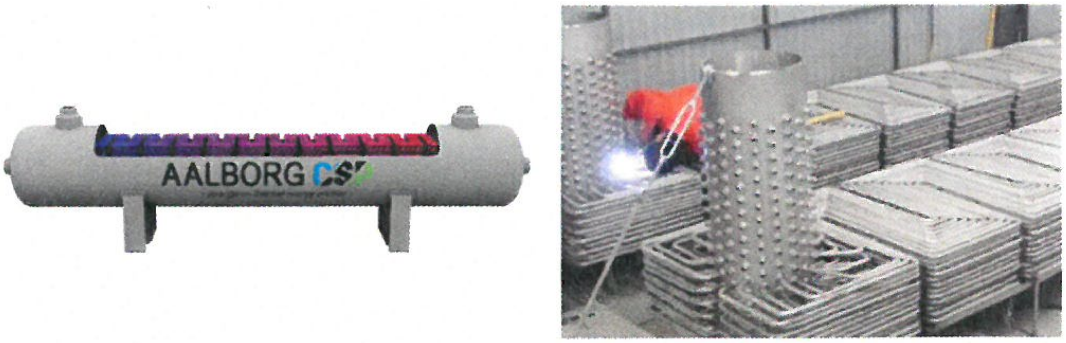

Figure 2.2.1: Aalborg CSP header-and-coil HX [21]

In literature, no example of a sodium-chloride salt HX was found, while several HX designs adopted singularly for sodium and molten salts are available and they are presented in the following.

2.2.1 Sodium experiences

As cited in section 2.1.1, the nuclear sector represents the major field where sodium has been employed so far. Because of its high conductivity and excellent heat transfer features, liquid sodium is a universally accepted coolant for Fast Breeder Reactors (FBR). Typically, in a FBR plant, a sodium-to-sodium Intermediate Heat Exchanger (IHX) constitutes a fundamental barrier and interface between the primary sodium (radioactive) and the secondary one (non-radioactive).

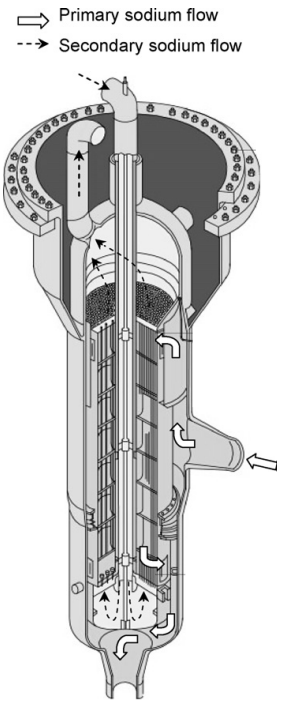

Figure 2.2.2: Schematic representation of the IHX employed in Monju [22]

Figure 2.2.2 shows a schematic representation of the IHX employed in the Japanese sodium-cooled fast reactor Monju, now closed. Shell and tube HX was selected for this application, and, in detail, primary sodium flows and is contained in the central tube, while the secondary sodium is placed in the shell-side.

Similar IHX configurations were adopted also for the 500 MWe prototype FBR part of the Madras Atomic Power Station (MAPS) and for the 3 MW test-case HX located both at Kalpakkam. In these cases, primary sodium is placed in the shell-side, while the secondary sodium flows into the central down-comer of the shell and tube IHX. The two examples are reported in figure 2.2.3.

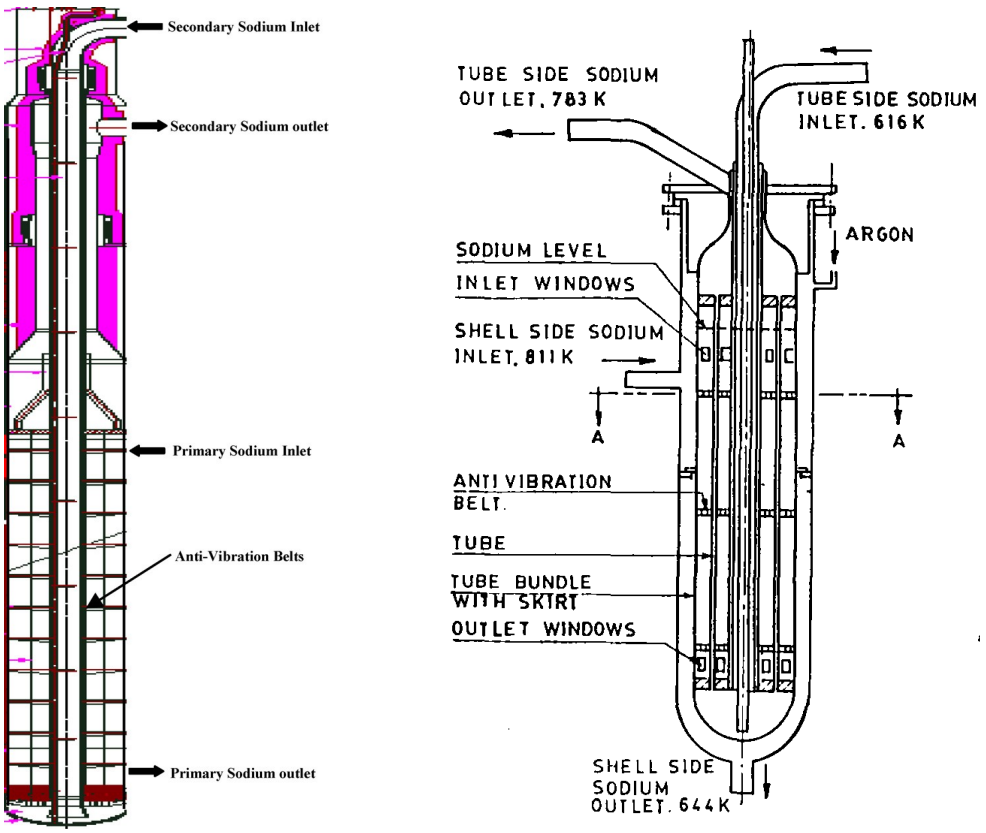

(a) IHX used in MAPS, Kalpakkam [23]

(b) 3 MW test-case HX [24]

Figure 2.2.3: Sodium-to-Sodium HX schematic representations

Another relevant example of HX adopted for sodium applications is the double-walled straight tubes Steam Generator (SG) designed in [25] for the Japan Sodium-cooled Fast Reactor (JSFR) implemented in the "Fast Reactor Cycle Technology Development (FaCT)" project. Figure 2.2.4 shows its conceptual design representation.

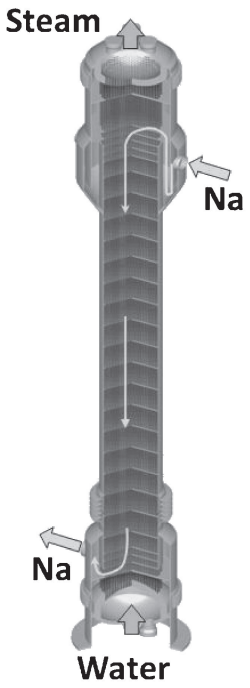

Figure 2.2.4: SG employed in JSFR [25]

2.2.2 Molten Salt experiences

In order to provide a stable and reliable power supply, many commercial solar thermal power plants rely on indirect thermal storage systems. Up to date, almost all commercial parabolic trough CSP plants use synthetic oil as the heat transfer fluid [26] and conventional molten salts as storage fluid According to [27], shell-and-tube heat exchangers are the most common type of heat exchangers used in these facilities. The thermal oil - molten salt heat exchanger shown in figure 2.2.5 is part of the CIEMAT-PSA molten salt test loop for thermal energy systems (MOSA) facility.

Figure 2.2.5: Thermal oil - molten salt HX [27]

Figure 2.2.6 provides a schematic representation of this HXwhich is composed of two counter-flow multi-pass shell-and-tube units. In this application, molten salt (*SolarSalt*) flows on the shell-side, while thermal oil (*Therminol VP-1*) on the tube-side.

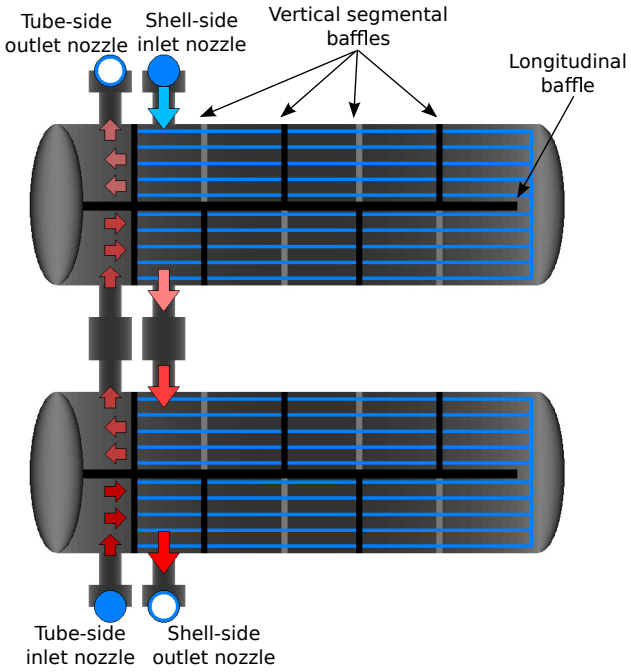

Figure 2.2.6: HX schematic representation [28]

In [29], it is provided another example of a molten salt-thermal oil heat exchanger design. In detail, a special flow layout with U-shaped tubes applied in the laboratory was designed for testing the heat transfer performances. of molten salt in the shell side of a shell-and-tube heat exchanger with segmental baffles. As shown in figure 2.2.7, the tube-side fluid employed is thermal oil.

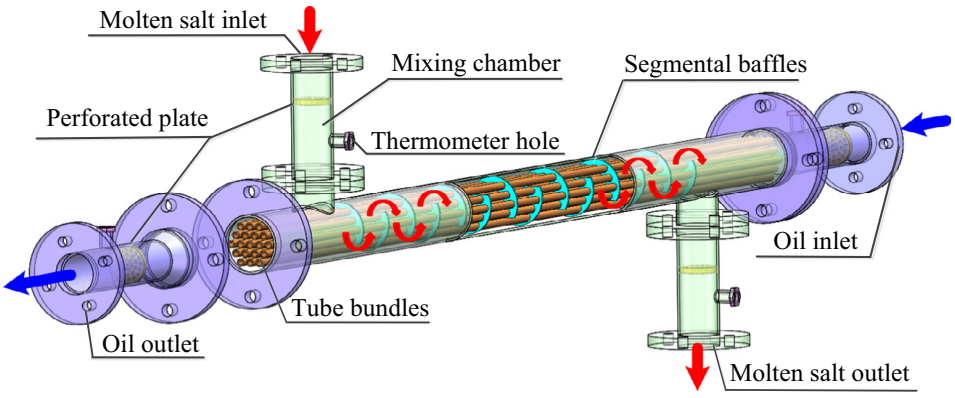

Figure 2.2.7: Diagram of the test case thermal oil - molten salt HX [29]

In the end, different SG designs employing molten salts for solar applications were found in literature. One model, proposed by *ABB Lummus*, consists of a U-tube kettle boiler and U-tube/straight shell HX for the pre-heater, super-heater and re-heater. Another example is provided by the *Foster Wheeler*design that assumes straight tube /straight shell HX with the molten salt placed on the shell side. A U-tube/U-shell HX design is instead proposed by *Babcock and Wilcox* with the molten salt placed again on the shell side.

Figure 2.2.8 shows a conceptual SG design proposed in [30] for solar power tower plants using molten salt as heat transfer fluid. The SG is characterized by a U-tube/U-shell HX design with single segmental baffle for the pre-heater, the super-heater and the re-heater. The salt is placed on the shell side and the high-pressure water/steam is placed on the tube side. For what concerns the evaporator, a vertical straight shell/straight tube was chosen.

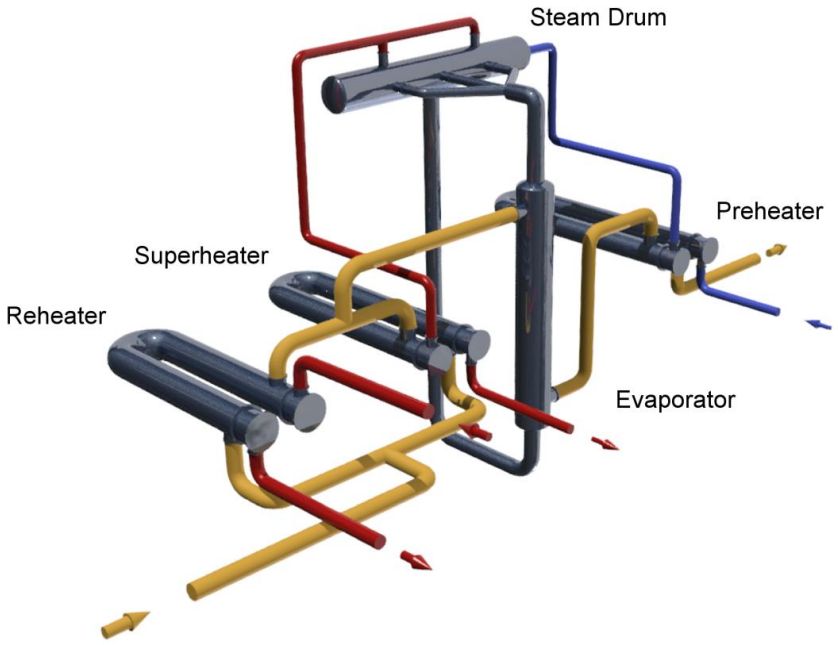

Figure 2.2.8: Molten salt SG [30]

Chapter 3

Heat Exchanger Model

This chapter presents how the heat exchanger model is implemented, describing the main goals, the methodology, and the main assumptions. The model is tailored for shell and tube heat exchangers and it is implemented using Modelica as programming language. Figure 3.0.1 reports the HX symbol utilized on the open source *SolarTherm* library, where the model is available[1].

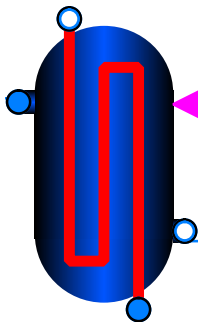

Figure 3.0.1: Symbol of HX model on *SolarTherm* library

3.1 Preliminary assumptions

Although the heat exchanger model tends to be a versatile and general model that can be employed for several applications and using different media, the assumptions of the model were adopted coherently with the primary goal of this research work: designing a sodium-salt HX and performing annual simulations.

- The heat exchanger *thermal losses* were considered negligible;

[1] https://github.com/SolarTherm/SolarTherm/blob/na-salt-hx/SolarTherm/Models/Fluid/HeatExchangers/HX.mo

- The principal assumption concerns the heat exchanger type selection. In particular, *shell and tube configuration* was chosen. According to the literature, no previous experiences with sodium-chloride salt heat exchangers were found. As for sodium is generally utilized in tube-in-tube heat exchangers in nuclear applications, while, for what concerns the molten salt, shell and tube configurations are generally preferred. On top of that, compare to other heat exchanger configurations, larger literature data is available for shell and tube. In addition, Tubular Exchanger Manufacturers Association (TEMA) standard can be used to guide the design process, and a simple and robust design guarantees wide range of operational temperatures and pressures;
- The *LMTD approach* was adopted;
- The limited variation of the fluid properties of sodium and chloride salt in the temperature range proposed (less then 5%) justified the decision to implement a *lumped-parameter model*;
- Transitional processes such as switch on/off of the heat exchanger were considered of secondary importance compare to the main operating condition; therefore, a *quasi-static model* was developed.

3.2 General description of the model

The model aims to propose a suitable design of a shell and tube heat exchanger and to simulate its operating conditions for a specific application. Two running modes of the model are distinguished:

- *Design mode*: it aims to propose an HX design;
- *Operating mode*: it aims to evaluate the expected performances of the defined HX design.

The implementation of the afore mentioned running modes requires to solve the three equations presented henceforth: thermal power balance on tube-side (equation (3.1)), thermal power balance on shell-side (equation (3.2)), and the estimation of the heat load using LMTD method (equation (3.3)).

$$Q = \dot{m}_{hot} \cdot (h_{in,hot} - h_{out,hot}) \tag{3.1}$$

$$Q = \dot{m}_{cold} \cdot (h_{out,cold} - h_{in,cold}) \tag{3.2}$$

$$Q = U \cdot A_{HX} \cdot F \cdot \Delta T_{lm} \tag{3.3}$$

where $\dot{m}$ is the mass flow rate, h_{in} and h_{out} are respectively inlet and outlet enthalpies, U is the heat transfer coefficient, A_{HX} is the heat transfer area, F is the temperature correction factor and ΔT_{lm} is the LMTD. According to [31], it is safer to allocate the cold fluid around the hot fluid, as well as, it will reduce energy loses and the overall the equipment cost. Thus, in absence of specific requirements, the hot fluid will be placed in tube-side (subscript hot), while the cold one on the shell-side (subscript $cold$).

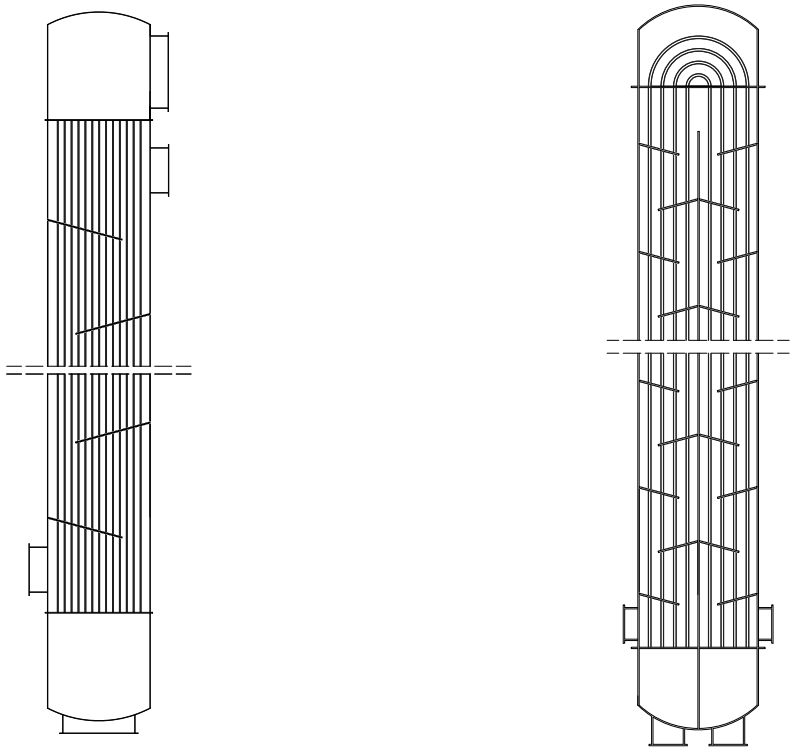

(a) 1:1 TEMA E STHE

(b) 2:2 TEMA F STHE

Figure 3.2.1: Two possible HX configurations

The possible shell and tube configurations considered in this model are:

- 1 shell pass, 1 tube pass (1:1 TEMA E STHE);
- 2 shell passes, 2 tube passes (2:2 TEMA F STHE);
- 1 shell pass, 2 tube passes (1:2 TEMA E STHE);
- 2 shell pass, 4 (or multiple) tube passes (2:4 TEMA F STHE).

Figure 3.2.1 shows a graphical representation of 1:1 TEMA E STHE and 2:2 TEMA F STHE. In detail, compared to the standard TEMA configurations, two design variations can be noticed: tilted and heated baffles to facilitate drainage and guarantee anti-freeze on the shell-side.

The model points to be flexible, robust and widely usable for different applications. For this purpose, it needs to be customized in term of media adopted, constraints, Boundary Conditions (BCs), and correlations. Moreover, an objective function can be user-defined according to specific requirements related to the particular application. In principle, the model offers a default procedure that can be customized, acting on the blocks of diagram 3.2.2, in order to achieve the most suitable HX design. The geometrical assumptions for the HX design are presented in section 3.3 and the adopted methodology is described in section 3.4.

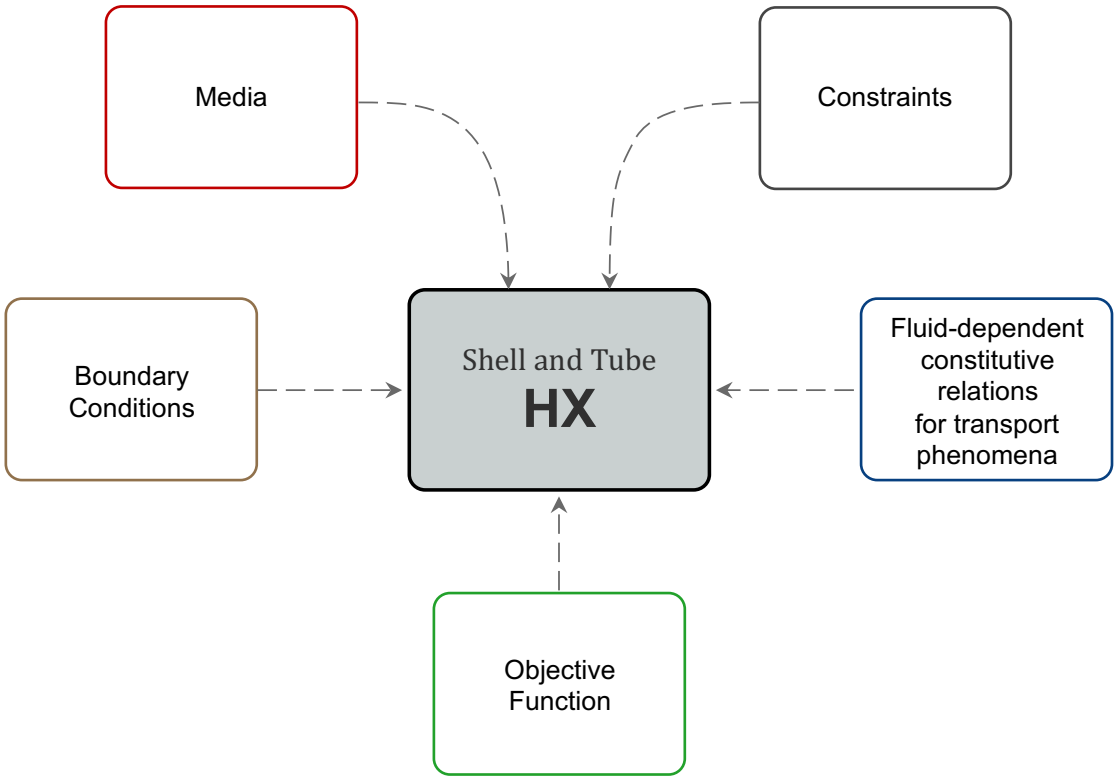

Figure 3.2.2: Block diagram customization HX

The block **Media** regards the fluids that flow in the shell and in the tube side, and the HX material. In detail, the correlations of the main properties such as density, thermal conductivity, specific heat capacity, and dynamic viscosity need to be defined according to the chosen media. Additionally, for the HX material, the mass specific cost should be provided.

The block **Boundary Conditions (BCs)** includes inlet/outlet fluid temperatures, operating pressures, and design thermal power.

In the block **Objective Function**, it should be defined what is the function that needs to be optimized during the design of the shell and tube HX. In other words, in this block it is possible to specify the goal of the HX optimization, e.g. minimizing the investment cost, or maximizing the heat transfer coefficient.

The block **Fluid-dependent constitutive relations for transport phenomena** regards the correlations that should be defined ad-hoc for the fluids, e.g. the HTC on the tube-side. Moreover, specific fluid dependent variables can be user-defined.

In the end, the block **Constraints** includes all the geometrical constraints that should be taken into account in the design process. In particular, it can be distinguished:

- Volume constraints:
  - Maximum HX lenght;
  - Maximum aspect-ratio.
- Velocity constraints:
  - Maximum/minimum hot fluid velocity;
  - Maximum/minimum cold fluid velocity;

Volume constraints are taken into account to fit the user requirements, while velocity constraints are needed for safety reasons. Indeed, the velocity must be high enough to prevent any suspended solids settling, but not that high to cause erosion [32]. Section 3.4, explains how these constraints impacts on the HX design.

3.3 Heat exchanger geometry description

In this section, a detailed description of the heat exchanger geometry is provided. In this work, particular focus was given on three major components: tubes, baffles, and shell. Other components, such as nozzles, expansion joints, and supports were considered of secondary importance and were neglected in the design of the shell and tube heat exchanger. A representation of the major components and of a cut section of a shell and tube heat exchanger are proposed respectively in figure 3.3.1 and 3.3.2.

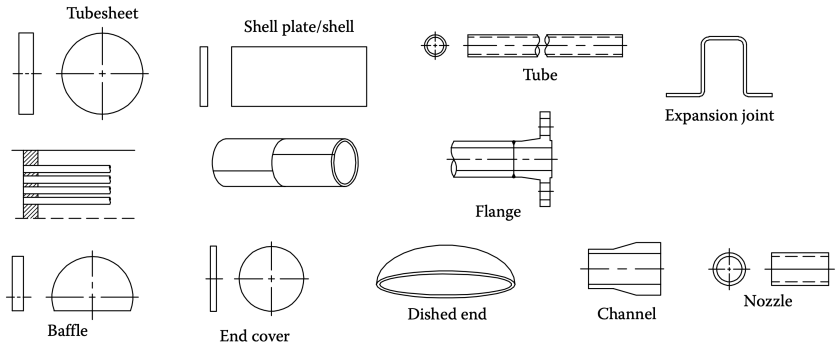

Figure 3.3.1: Major components of a shell and tube heat exchanger [33]

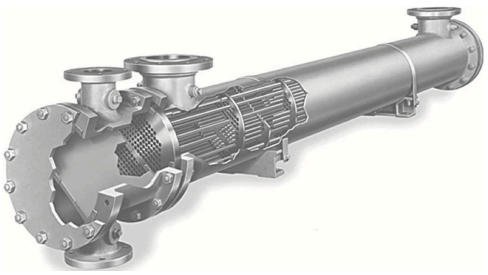

Figure 3.3.2: Cut section of a shell and tube heat exchanger [33]

3.3.1 Tubes

Since the tube surface is the place where the desired heat transfer takes place, the tube variables selection represents a focal point in the heat exchanger design. In order to completely define the tube bundle, the tube variables considered are:

- **tube outside diameter** (d_o): it is one of the most relevant variables for the HX design. In this model, only commercial tube diameters are considered. In detail, commercial tubing data proposed by TEMA are adopted. According to [33], they are $\frac{1}{4}$, $\frac{3}{8}$, $\frac{1}{2}$, $\frac{5}{8}$, $\frac{3}{4}$, $\frac{7}{9}$, 1, $1\frac{1}{4}$, $1\frac{1}{2}$, and 2 in. (6.35, 9.53, 12.70, 15.88, 19.05, 22.23, 25.40, 31.75, 38.10, and 50.80 mm). Additionally, a tube diameter of $2\frac{1}{2}$ in (63.5 mm) is utilized for some particular applications.

- **tube wall thickness** (t_{tube}): it is function of the tube outside diameter, of the pressure differences across the tube wall, and of the selected tube material alloy. These standard values are available in TEMA Table RCB-2.21 [34].
- **tube layout pattern** ($layout$): it impacts on the maximum number of tubes that can be included within the shell, on the pressure drops, on the heat transfer, and on the accessibility for mechanical cleaning [33]. Two types of tube arrangements are implemented in this model: triangular and square (figure 3.3.3).

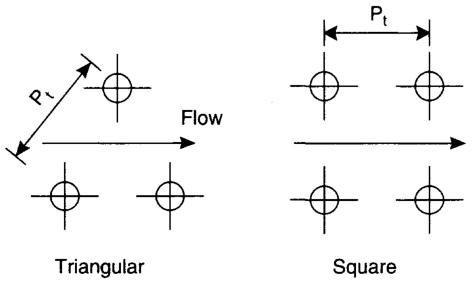

Figure 3.3.3: Tube layout arrangements [32]

- **tube pitch** (P_t): it is the distance between the centres of the tube hole. For the two tube layout arrangements considered, the tube pitch can be estimated as function of the tube outside diameter, as indicated in equation (3.4) [32].

$$P_t = 1.25 \cdot d_o \tag{3.4}$$

- **number of tube passes** (N_p): it impacts strongly on the tube bundle geometry. According to [33], the possible number of tube passes to select can be 1, 2, 4 or multiples, up to 16. Figure 3.3.4 shows two different tube bundles for number of tube passes respectively equal to 1 (a) and 2 (b).

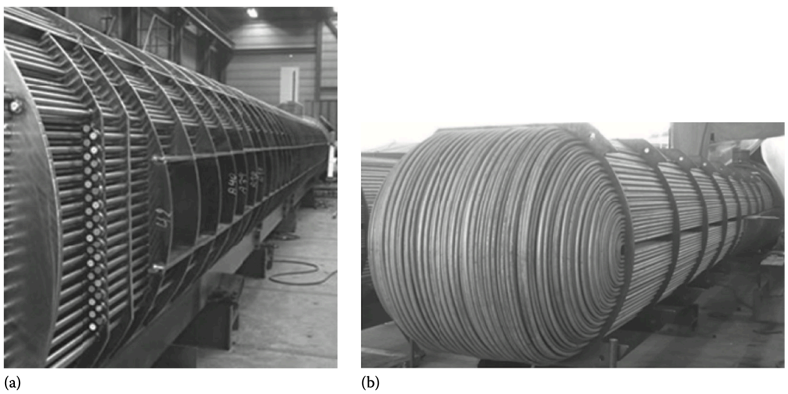

Figure 3.3.4: Examples of tube bundle: $N_p = 1$ (a) and $N_p = 2$ (b) [33]

- **number of tubes** (N_t): it is a fundamental variable for the tube bundle definition. According to [32], the tube bundle diameter (D_b) can be calculated as function of the number of tubes, tube outside diameter, number of tube passes, and tube arrangement types.
- **tube pass length** (L): it coincides with the tube length for a straight tube bundle. It is treated as a continuous variable and, for a fixed number of tubes and a specific number of tube passes, it will be used to fit the desired heat transfer area. The only restrictions applied on the length come from the volume constraints, user-defined. According to [35], an heat exchanger configuration with a small shell diameter and long tubes represents the most economical solution.
- **tube sheet thickness** (L_b): it is considered a constant and according to [34] its value can be assumed equal to 0.005 m.

3.3.2 Shell

The TEMA standard distinguishes five different shell types, reported in figure 3.3.5. They are identified with the letter E, F, G, H, and J. In this model, only the E and F shell type are implemented, because they are the two most commonly used. In particular, the E shell is the simplest one, characterized by a single shell pass, whilst the F shell has a longitudinal baffle that separates two shell passes.

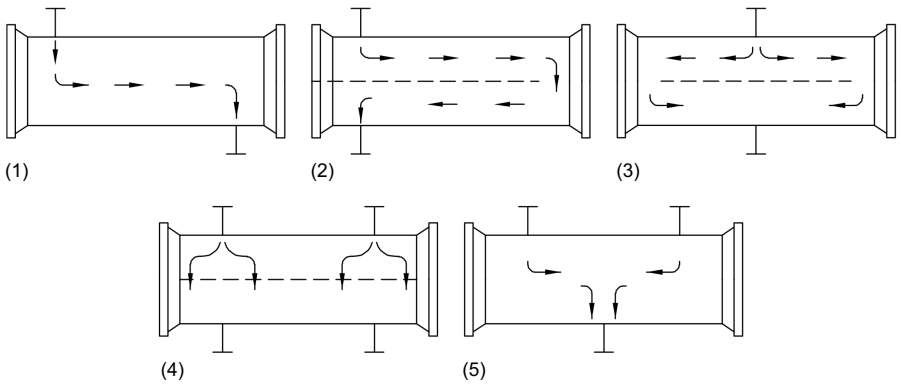

Figure 3.3.5: Shell types and shell-side flow distribution pattern. (1) E shell: One-pass, (2) F shell: two-pass with longitudinal baffle, (3) G shell: split flow, (4) H shell: double split flow, and (5) J shell: divided flow [33]

Generally, a single shell is preferred because the cost of the shell represents the largest share of the heat exchanger total investment cost [33]. Additionally, a more economical

heat exchanger configuration is usually characterized by a small shell diameter and the maximum tube pass length permitted by volume constraints [36].

The shell design can be completely defined starting from the following variables:

- **number of shell passes** (N_{sp}): it influences strongly the HX design. This variable is used to select the shell type. In particular, if the number of shell passes is equal to 1, it means that the E shell is adopted, whilst if its value is equal to 2, the F type is considered.
- **bundle-to-shell clearance** (L_{bb}): it is the distance between the shell inside diameter and the tube bank outer-line diameter (D_{otl}), as shown in figure 3.3.6. It is important to specify that the bundle diameter calculated in equation (3.19) is referred to the centre-line diameter (D_{ctl}). In order to estimate L_{bb}, the TEMA standard provides the following correlation:

$$L_{bb} = \frac{12.0 + 5 \cdot (D_b + d_o)}{1000} \tag{3.5}$$

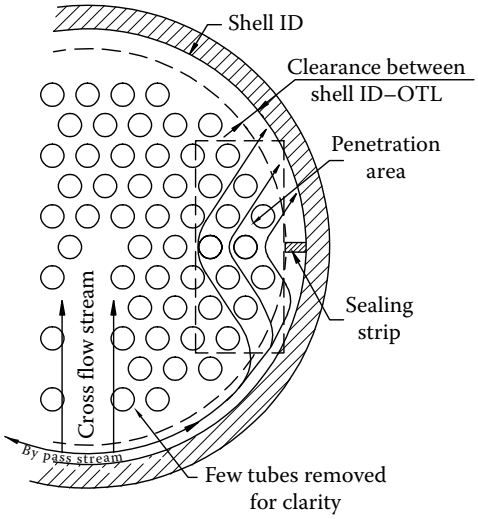

Figure 3.3.6: Heat exchanger cross section. Bundle to shell clearance (L_{bb}), shell inside diameter (D_s), shell wall thickness (t_{shell}), and sealing strips influence on the flow [33]

- **shell inside diameter** (D_s): it can be found as the sum of the tube bundle diameter (D_b), of the tube outside diameter (d_o), and of the bundle-to-shell clearance (L_{bb}).
- **shell wall thickness** (t_{shell}): it is function of the pressure and of the shell inside diameter. For pressure applications, it needs to be dimensioned following the

procedure for pressure vessels. Instead, for atmospheric pressure applications, shell thicknesses are furnished in the TEMA Tables R-3.13 and CB-3.13 [34].

- **number of sealing strips per crossflow row** (SS): The sealing strips aim to minimize the bypassing of fluid around the bundle. As shown in figure 3.3.5, they force the shell-side flow towards the tube field. According to TEMA, the *number of sealing strips per crossflow row* can be considered equal to 0.2.

3.3.3 Baffles

On the shell side, in order to channelize the fluid across or along the tube bundle, it is necessary to include several baffles. They can be classified as transverse or longitudinal. The longitudinal ones aim to split the shell side flow, distinguishing two shell passes, e.g. F shell. Thus, they are utilized only on multi-pass shell configurations. On the contrary, every shell and tube exchanger has transverse baffles. Indeed, besides the task of directing the flow, they are used to support the tubes and also to maintain the tube spacing [33]. The most commonly used transverse baffle type is the segmental baffle, therefore only this type was adopted in this model. This is a circular disk having a segment removed (baffle cut). Figure 3.3.7 shows that the shell side flow is strongly affected by the baffle cut and baffle spacing [37]. Thus, a wrong proportion of these parameters could lead to inefficient heat transfer and too high-pressure losses.

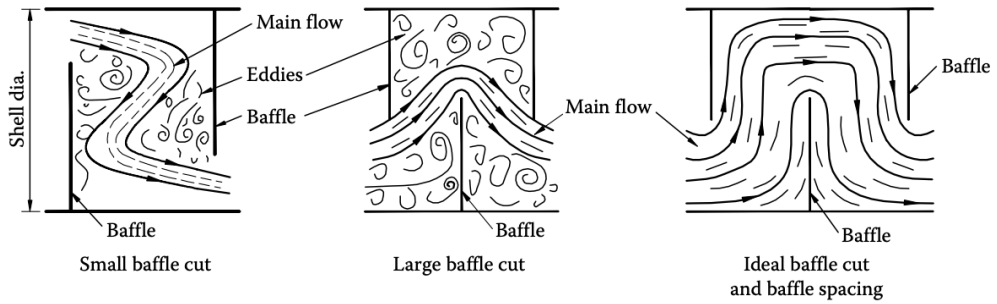

Figure 3.3.7: Baffle influence on the shell-side flow distribution [33]

In order to complete the heat exchanger design on the shell side, the baffle variables need to be properly defined.

- **Baffle cut** (B_c): it generally varies from 20% to 30%. TEMA recommends B_c equal to 20% as optimum baffle cut, because it can lead to the highest heat transfer for a given pressure drop [33]. Figure 3.3.8 shows segmental baffles with baffle cuts $B_c = 20\%$. It is possible to define the baffle cut length as $L_c = B_c \cdot D_s$.

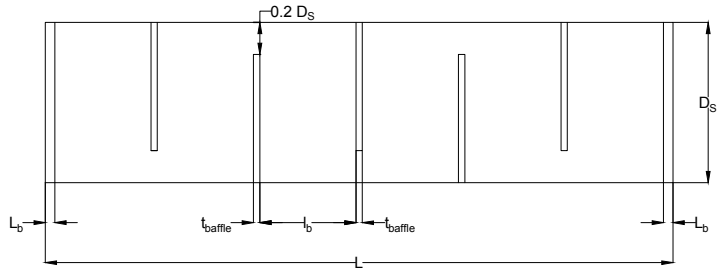

Figure 3.3.8: Baffles distribution. Tube pass length (L), tube sheet thickness (L_b), baffle thickness (t_{baffle}), shell inside diameter (D_s), and baffle spacing (l_b)

- **Baffle spacing** (l_b): it is the distance between two consecutive baffles. According to [38], the practical range of baffle spacing is between 15% and 100% of the shell inside diameter (D_s). Moreover, as it can be noticed from figure 3.3.8, the baffle spacing is strictly related to the **number of baffles** (N_b) (equation (3.6)). Thus, in this model, they are treated together and the constraints applied to the number of baffles influence directly the baffle spacing and vice versa.

$$(l_b + t_{baffle}) \cdot (N_b + 1) = L - t_{baffle} + 2 \cdot L_b \tag{3.6}$$

- **Baffle thickness** (t_{baffle}): it is function of the shell inside diameter, of the baffle spacing and of the heat exchanger material. TEMA provides the minimum baffle thickness in Tables R-4.41 [34].
- **Shell-to-baffle diametral clearance** (L_{sb}): it can be estimated, following TEMA correlation, as function of the shell inside diameter [34]:

$$L_{sb} = \frac{3.1 + 0.004 \cdot D_s}{1000} \tag{3.7}$$

- **Tube-to-baffle diametral clearance** (L_{tb}): it is considered a constant and according to [34] its value can be assumed equal to 0.0008 m.

The rest of the shell-side geometry is defined starting from the independent variables and assuming the parameters mentioned above. Some geometrical variables are still assumed according to TEMA standards, while all the flow areas are identified and calculated using the Bell-Delaware method. The shell-side auxiliary calculations are reported in appendix A.2.

3.4 Design Strategy

In this section, it is presented the detailed strategy implemented to propose a heat exchanger design that respects the adopted constraints, that results suitable with the utilized media and for the applied boundary conditions. To design a heat exchanger means to propose a heat transfer area (A_{HX}), a detailed description of its full geometry, the estimated investment cost (C_{inv}), and the expected performances at the design point. The heat exchanger is designed following the TEMA standards. In principle, some geometrical parameters are treated as independent variables, while the rest of the heat exchanger geometry is estimated using the proposed TEMA correlations. Therefore, five geometrical parameters can be identified as design variable and they are reported in table 3.4.1.

Design variable	**Symbol**	**UM**	**Assumed range**
Tube outside diameter	d_o	mm	[6.35 - 63.5]
Number of tube passes	N_p	-	[1, 2, 4 *or multiples*]
Number of shell passes	N_{sp}	-	[1, 2]
Tube layout	$layout$	-	[$triangular$, $square$]
Number of tubes	N_t	-	[$N_{t,min}$ - $N_{t,max}$]

Table 3.4.1: Geometrical design variables (where d_o range is assumed according to TEMA dimensional data for commercial tubing)

Moreover, if only three of four inlet/outlet temperatures are defined in the boundary conditions, an extra design variable can be the unknown temperature.

Design variable	**Symbol**	**UM**	**Assumed range**
Temperature unknown	$T_{unknown}$	K	To be defined

Table 3.4.2: Optional design variable

The block diagram reported in figure 3.4.1 outlines the procedure followed to select the optimal HX configuration. Each combination of design variable values leads to a different heat exchanger design. For the purpose of proposing the most suitable solution, an optimization process is carried out. In detail, in order to meet the specific requirements of the particular application, an objective function needs to be user-defined. Consequently, the model will evaluate all the possible combinations and will propose the heat exchanger design that optimizes the ad-hoc defined objective function.

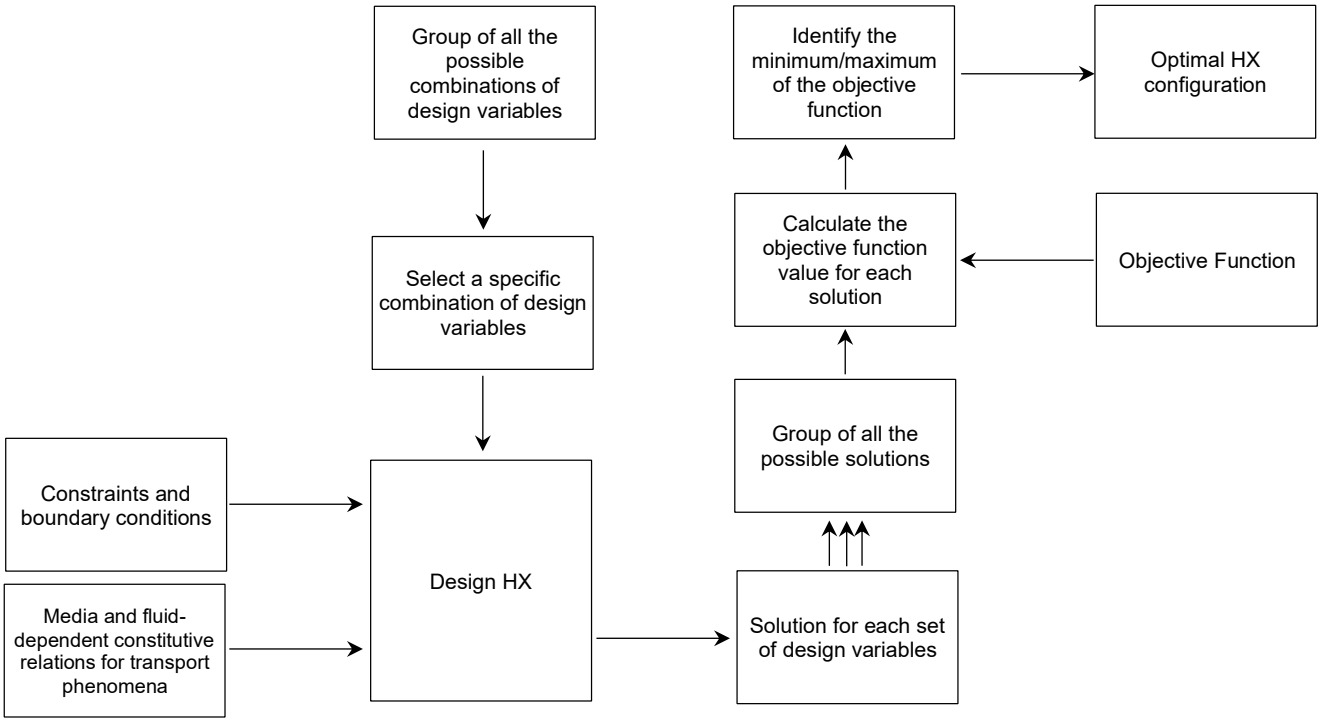

Figure 3.4.1: Block diagram of the design strategy

The block *Design HX* is the core of the design strategy, where for a specific set of assumed design variables, the HX design is fully chatacterized. The block diagram, presented in figure 3.4.2, provides a detailed description of the *Design HX* block.

In the following, the complete procedure is proposed and it can be divided in the undermentioned steps:

1. Preliminary calculations;
2. Geometry definition;
3. Heat transfer coefficients calculation ($HTCs$);
4. Pressure losses calculation (Δp_{losses});
5. Costs estimation;
6. Objective function calculation.

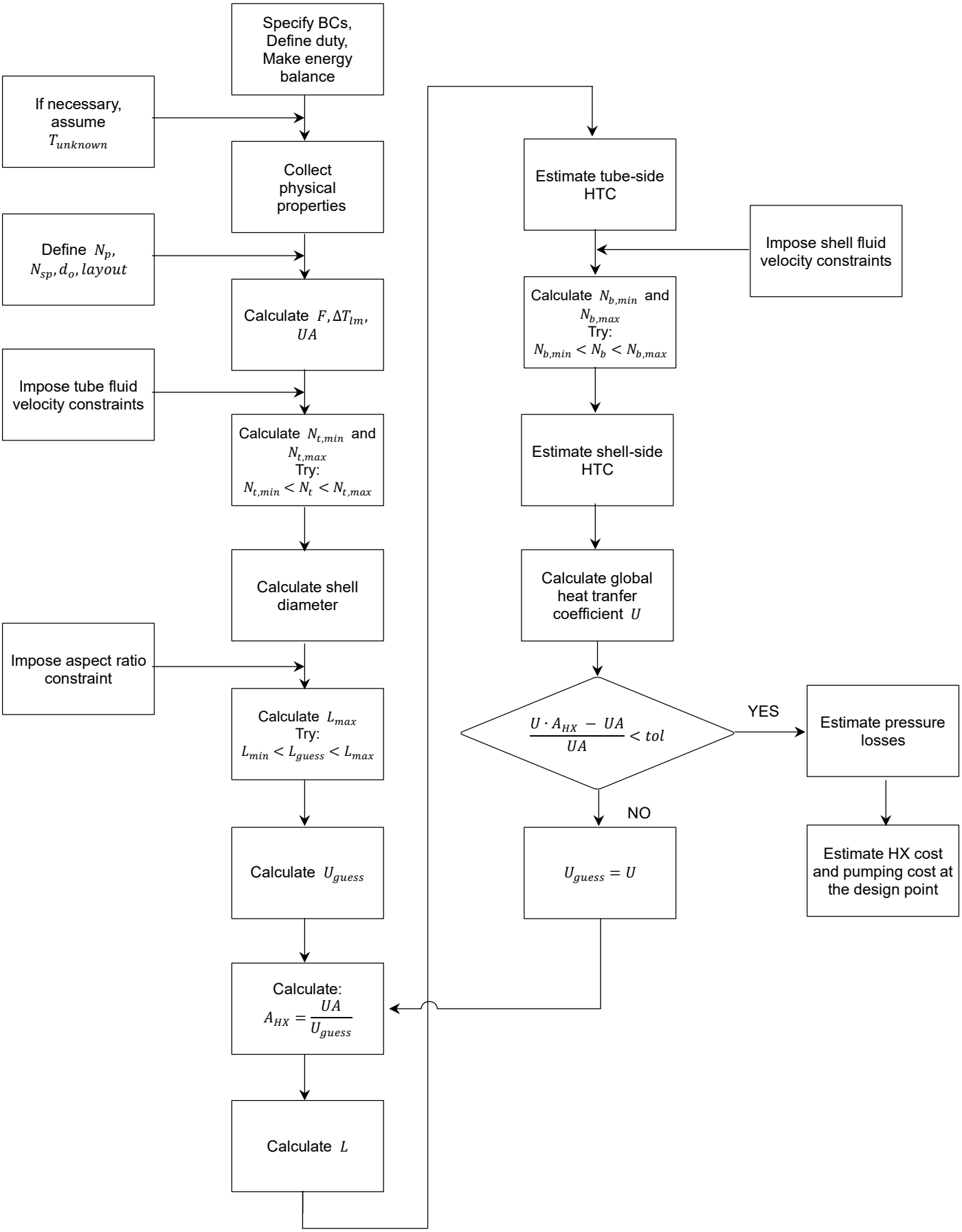

Figure 3.4.2: Block diagram of *Design HX* block

3.4.1 Preliminary calculations

In this section, the boundary conditions, such as thermal design power, inlet/outlet temperatures and pressures, are applied to the basic set of equations ((3.1), (3.2), (3.3)) in order to find the overall heat transfer coefficient required UA_{req}. Moreover, specific values for the following design variables are chosen and kept unchanged for the entire procedure:

- Tube outside diameter (d_o);
- Number of tube passes (N_p);
- Number of shell passes (N_{sp});
- Tube layout ($layout$).

According to the particular application, the following parameters need to be user-defined [2]:

- Thermal design power (Q);
- Hot-side inlet temperature ($T_{in,hot}$);
- Hot-side outlet temperature ($T_{out,hot}$);
- Hot-side inlet pressure ($p_{in,hot}$);
- Cold-side inlet temperature ($T_{in,cold}$);
- Cold-side outlet temperature ($T_{out,cold}$);
- Cold-side inlet pressure ($p_{in,cold}$);

Based on the inlet/outlet temperatures mentioned above and on the media adopted, the inlet/outlet enthalpies can be calculated. Moreover, the average hot-side and cold-side temperatures can be calculated as in the following:

$$T_{ave} = \frac{T_{in} + T_{out}}{2} \tag{3.8}$$

After that, all the physical properties can be calculated at the average temperature for both sides. The most relevant properties are:

- Density (ρ);

[2] if one of the temperature is unknown and it represents a design variable, a range of acceptable values should be user-defined

- Specific heat capacity (c_p);
- Dynamic viscosity (μ);
- Thermal conductivity (λ);

From equations (3.2) and (3.1), the hot-side and cold-side mass flow rates can be respectively found by:

$$\dot{m}_{hot} = \frac{Q}{h_{in,hot} - h_{out,hot}} \tag{3.9}$$

$$\dot{m}_{cold} = \frac{Q}{h_{out,cold} - h_{in,cold}} \tag{3.10}$$

Successively, knowing all the inlet/outlet temperatures, the log mean temperature difference (ΔT_{lm}) can be calculated using equation (3.11).

$$\Delta T_{lm} = \frac{(T_{hot,outlet} - T_{cold,inlet}) - (T_{hot,inlet} - T_{cold,outlet})}{\ln\left(\frac{T_{hot,outlet} - T_{cold,inlet}}{T_{hot,inlet} - T_{cold,outlet}}\right)} \tag{3.11}$$

Additionally, the temperature correction factor (F) can be calculated as function of the temperatures and HX configuration. In particular, for 1 shell pass/1 tube pass (1:1 TEMA E STHE) and for 2 shell passes/2 tube passes (2:2 TEMA F STHE), the flow arrangement is countercurrent, resulting in F factor 1.0 [33].

$$F = \begin{cases} 1 & \text{if countercurrent} \\ f(N_p, N_{sp}, T_{in,hot}, T_{out,hot}, T_{in,cold}, T_{out,cold}) & \text{otherwise} \end{cases}$$

The temperature correction factor correlations are available in Appendix A.1.

In the end, rewriting equation (3.3), the overall heat transfer coefficient can be calculated as indicated in equation (3.12).

$$UA_{req} = \frac{Q}{F \cdot \Delta T_{lm}} \tag{3.12}$$

In this way, the overall heat transfer coefficient UA_{req} is known, but the specific coefficients (U and A_{HX}) that give the required product need to be distinguished. This requires an iterative process. Indeed, it is necessary to guess the heat transfer coefficient to get the value of the required area, and once the HX geometry is determined, it is necessary to verify the condition $UA_{req} \approx U \cdot A_{HX}$. If the condition

is not respected, the calculated U will be the successive U_{guess} and the procedure will be repeated until convergence. In section 3.4.2, just the equations that lead to the HX geometry definition are presented.

3.4.2 Geometry definition

In this section, a HX geometry that fits the BCs imposed previously is presented. In addition, the configuration need to respect the volume and velocity constraints user-defined. According to [39], the recommended tube length to shell diameter aspect ratio is in the range 5 to 10. Thus, if no particular volume constraints are defined, the maximum acceptable HX length is calculated imposing a maximum L/D_s aspect ratio equal to 10.

Firstly, the tube inside diameter (d_i) is calculated knowing the tube wall thickness (t_{tube}) and the tube outside diameter (d_o) according to equation (3.13). Consequently, the single tube cross section (A_{cs}) can be found as indicated in equation (3.14).

$$d_i = d_o - 2 \cdot t_{tube} \tag{3.13}$$

$$A_{cs} = \frac{\pi}{4} \cdot (d_i)^2 \tag{3.14}$$

After that, the number of tubes (N_t) needs to be determined. In this model, it represents the design variable used to impose the tube side velocity constraints (equation (3.16)). Indeed, for a specific number of tube passes (N_p) and a fixed tube-side mass flow rate ($\dot{m}_{hot}$), it is possible to determine the minimum and maximum acceptable number of tubes, respectively function of maximum and minimum fluid velocity. The mass flow rate can be found as indicated in equation (3.15).

$$\dot{m}_{hot} = \rho_{hot} \cdot A_{tot,cs} \cdot v_{tube} \tag{3.15}$$

where ρ_{hot} is the tube-side fluid density, v_{tube} is the fluid velocity, and $A_{cs,tot}$ is the tube bundle cross section and it can be calculated as in equation (3.18). Therefore, combining equations (3.15), (3.17), and (3.18), the minimum and maximum number of tubes can be found as indicated henceforth (equation (3.16)).

$$N_{t,min} = \frac{\dot{m}_{hot} \cdot N_p}{\rho_{hot} \cdot A_{cs} \cdot v_{tube,max}} \qquad N_{t,max} = \frac{\dot{m}_{hot} \cdot N_p}{\rho_{hot} \cdot A_{cs} \cdot v_{tube,min}} \tag{3.16}$$

The number of tubes is picked between $N_{t,min}$ and $N_{t,max}$, and it is replaced cyclically in order to try all the acceptable values.

Then, for a specific number of tubes, it's possible to calculate Tep, the number of tubes for each pass (equation (3.17)), $A_{tot,cs}$, the tube bundle cross section (empirical equation (3.18)), D_b, the tube bundle diameter (equation (3.19)), and D_s, the shell inside diameter (equation (3.20)).

$$Tep = N_t/N_p \tag{3.17}$$

$$A_{tot,cs} = Tep \cdot A_{cs} \tag{3.18}$$

$$D_b = d_o\Big(\frac{N_t}{K_1}\Big)^{1/n_1} \tag{3.19}$$

where K_1 and n_1 are the two constants that are reported in table 3.4.3 [32].

Triangular arrangement					
No. passes	1	2	4	6	8
K_1	0.319	0.249	0.175	0.0743	0.0365
n_1	2.142	2.207	2.285	2.499	2.675
Square arrangement					
No. passes	1	2	4	6	8
K_1	0.215	0.156	0.158	0.0402	0.0331
n_1	2.207	2.291	2.263	2.617	2.643

Table 3.4.3: Constants for use in equation (3.19) [32]

$$D_s = D_b + L_{bb} + d_o \tag{3.20}$$

Then, knowing the shell wall thickness(t_{shell}), the shell outside diameter can be found as in equation (3.21).

$$D_{s,out} = D_s + 2 \cdot t_{shell} \tag{3.21}$$

At this point, it's necessary to face the iterative procedure to split the required overall heat transfer coefficient UA_{req} into a proposed heat transfer area (A_{HX}) and heat transfer coefficient (U).

In order to start this procedure, a heat transfer coefficient value, U_{guess}, is adopted and it is calculated as indicated in equation (3.24). A HX length guess value (L_{guess}) is picked between minimum and maximum acceptable length (L_{max}). It can be user-defined or calculated from the maximum aspect ratio. Consequently, guess values of the single tube area ($A_{st,guess}$), of the heat exchanger area (A_{guess}), and of the heat transfer coefficient (U_{guess}) are calculated as follow:

$$A_{st,guess} = \pi d_o \cdot L_{guess} \tag{3.22}$$

$$A_{guess} = N_t \cdot A_{st,guess} \tag{3.23}$$

$$U_{guess} = \frac{UA_{req}}{A_{guess}} \tag{3.24}$$

The heat transfer area is given by:

$$A_{HX} = \frac{UA_{req}}{U_{prev}} \tag{3.25}$$

where U_{prev} is the heat transfer coefficient found during the previous iteration or, at the starting point, the guess values U_{guess}.

Then, calculating the single tube area, A_{st} (3.26) and the HX length L (3.27), the tube bundle geometry is completely defined.

$$A_{st} = \frac{A_{HX}}{N_t} \tag{3.26}$$

$$L = \frac{A_{st}}{\pi d_o} \tag{3.27}$$

After that, the baffles configuration needs to be defined. As cited in section 3.3.3, the number of baffles (N_b) and baffle spacing (l_b) are strictly related to each other. In this model, the number of baffles represents the design variable used to impose the shell-side velocity constraints (equation (3.32)). Indeed, for a fixed tube bundle geometry (L, N_t, d_o, $layout$) and a fixed shell-side mass flow rate ($\dot{m}_{cold}$), it is possible to determine the minimum and maximum acceptable number of baffles, respectively function of minimum and maximum fluid velocity.

The mass flow rate can be found as indicated in equation (3.28).

$$\dot{m}_{cold} = \rho_{cold} \cdot S_m \cdot v_{shell} \tag{3.28}$$

where ρ_{cold} is the shell-side fluid density, v_{shell} is the shell-side fluid velocity, and S_m is the shell-side crossflow area and it can be calculated as in equation (3.29).

$$S_m = \frac{l_b}{N_{sp}}\Big(L_{bb} + \frac{D_b}{P_t}(P_t - d_o)\Big) = \frac{l_b}{N_{sp}} \cdot L_{cf} \tag{3.29}$$

where L_{cf} is the crossflow free length.

Applying the minimum and maximum shell-side fluid velocity and using (3.28) and (3.29), the resulting minimum and maximum baffle spacing can be calculated as follow:

$$l_{b,min} = \frac{N_{sp} \cdot \dot{m}_{cold}}{\rho_{cold} \cdot L_{cf}} \cdot \frac{1}{v_{shell,max}} \qquad l_{b,max} = \frac{N_{sp} \cdot \dot{m}_{cold}}{\rho_{cold} \cdot L_{cf}} \cdot \frac{1}{v_{shell,min}} \tag{3.30}$$

The relation between the number of baffles and the baffle spacing can be found rewriting equation (3.6) as:

$$N_b = \frac{L - t_{baffle} + 2 \cdot L_b}{l_b + t_{baffle}} - 1 \tag{3.31}$$

Thus, the minimum and maximum number of baffles can be found, from equation (3.30) and (3.31), as indicated in equation (3.32).

$$N_{b,min} = \frac{L - t_{baffle} + 2 \cdot L_b}{l_{b,max} + t_{baffle}} - 1 \qquad N_{b,min} = \frac{L - t_{baffle} + 2 \cdot L_b}{l_{b,max} + t_{baffle}} - 1 \tag{3.32}$$

The number of baffles is picked between $N_{b,min}$ and $N_{b,max}$, and it is replaced cyclically in order to try all the acceptable values. For a specific number of baffles, iteratively, the baffle thickness (t_{baffle}) and the baffle spacing (l_b) are calculated as in equation (3.31).

At this point, the most relevant parameters are known and all the shell-side flow areas can be evaluated following the equations reported in appendix A.2.

In the end, the overall volume and weight of the proposed configuration are estimated. For this purpose, the region occupied by the heat exchanger material is considered

characterized by the tube bundle, baffles and shell thickness overall dimensions. Besides the HX material, also the fluid weight and volume occupied are considered and calculated. The overall volume can be estimated as indicated in equation (3.33).

$$V_{HX} = V_{material} + V_{hot} + V_{cold} \tag{3.33}$$

where $V_{material}$ is the volume occupied by the heat exchanger material, while V_{hot} and V_{cold} are the regions occupied respectively by the hot and cold fluid.
Equation (3.34) shows how $V_{material}$ is calculated. In particular, V_{tubes} is calculated in equation (3.35), $V_{baffles}$ in equation (3.36), and $V_{shell,thickness}$ in equation (3.37).

$$V_{material} = V_{tubes} + V_{baffles} + V_{shell,thickness} \tag{3.34}$$

$$V_{tubes} = \pi \cdot \frac{d_o^2 - d_i^2}{4} \cdot L \cdot N_t \tag{3.35}$$

$$V_{baffles} = \pi \cdot \frac{D_s^2}{4} \cdot (1 - B) \cdot N_b \cdot t_{baffle} \cdot N_{sp} + t_{baffle} \cdot D_s \cdot L \cdot (N_{sp} - 1) \tag{3.36}$$

$$V_{shell,thickness} = \pi \cdot \frac{D_{s,out}^2 - D_s^2}{4} \cdot L \tag{3.37}$$

The hot-fluid region is the one confined by the tubes, therefore it can be estimated as follow:

$$V_{hot} = \pi \cdot \frac{d_i^2}{4} \cdot L \cdot N_t \tag{3.38}$$

Instead, the cold-fluid region can be estimated as the difference between the volume confined by the inside shell diameter and the one occupied by the tube bundle and the baffles.

$$V_{cold} = (D_s^2 - d_i^2 \cdot N_t)\frac{\pi}{4} \cdot L - V_{baffles} \tag{3.39}$$

Similarly, the HX weight can be estimated as indicated in equation (3.40)

$$m_{HX} = m_{material} + m_{hot} + m_{cold} \tag{3.40}$$

Where $m_{material}$, m_{hot}, and m_{cold} can be found as shown respectively in equation (3.41) and (3.42).

$$m_{material} = V_{material} \cdot \rho_{wall} \tag{3.41}$$

$$m_{hot} = V_{hot} \cdot \rho_{hot} \qquad m_{cold} = V_{cold} \cdot \rho_{cold} \tag{3.42}$$

where ρ_{wall} is the heat exchanger material density, calculated at the wall temperature, estimated as follow:

$$T_{wall} = \frac{T_{ave,hot} + T_{ave,cold}}{2} \tag{3.43}$$

Thus, for a set of assumed design variables, the heat exchanger configuration is completely defined.

3.4.3 Heat transfer coefficients calculation

In this section, the procedure to estimate the tube-side (h_s), the shell-side (h_s), and the overall HTC (U) is presented

Tube-side heat transfer coefficient

In order to estimate the tube-side heat transfer coefficient, a single tube can be investigated. Generally, the heat transfer coefficient can be calculated as function of the dimensionless Nusselt number Nu:

$$h_t = \frac{Nu_{hot} \cdot \lambda_{hot}}{d_i} \tag{3.44}$$

Since the hot-fluid flows inside a pipe, several correlations available in literature can be utilized to estimate the dimensionless Nusselt number. Generally, they are provided as function of two dimensionless numbers: Reynolds (Re) and Prandtl (Pr).

$$Nu_{hot} = f(Re_{hot}, Pr_{hot}) \tag{3.45}$$

According to the fluid utilized, the most suitable correlation should be user-defined. The above mentioned dimensionless numbers can be calculated as follow:

$$Re_{hot} = \frac{\rho_{hot} \cdot v_{tube} \cdot d_i}{\mu_{hot}} \qquad Pr_{hot} = \frac{\mu_{hot} \cdot c_{p,hot}}{\lambda_{hot}} \tag{3.46}$$

where the tube-side fluid velocity, v_{tube}, can be calculated rewriting equation (3.15):

$$v_{tube} = \frac{\dot{m}_{hot}}{A_{cs,tot} \cdot \rho_{hot}} \tag{3.47}$$

Shell-side heat transfer coefficient

The shell-side heat transfer coefficient can be estimated using the Bell-Delaware method. According to [40], this method is the most widely recognized standard for the design of heat exchangers. The Bell-Delaware method estimates the shell-side heat transfer coefficient (h_s) calculating first the ideal heat transfer coefficient and applying successively three correction factors. The ideal heat transfer coefficient ($h_{s,id}$) is found assuming complete crossflow between the fluid in the shell-side and tube bundle. The correction factors take into account the following aspects:

- effect of the baffles: baffle cut and spacing. This correction factor is used to take into account that only a fraction of the tubes are in pure cross-flow (J_C);
- leakage due to shell-to-baffle and tube-to-baffle clearances (J_L);
- bundle bypass flow due to the gap between tube bundle and shell (C stream in figure A.2.1) (J_B).

Therefore, the resulting shell-side heat transfer coefficient (h_s) is given by:

$$h_s = h_{s,id} \cdot J_C \cdot J_L \cdot J_B \tag{3.48}$$

The ideal heat transfer coefficient ($h_{s,id}$) can be calculated as function of the Nusselt number:

$$h_{s,id} = \frac{Nu_{cold} \cdot \lambda_{cold}}{d_o} \tag{3.49}$$

According to [40], the Nusselt number can be calculated using the following correlation:

$$Nu_{cold} = a \cdot Re_{cold}^{m} \cdot Pr_{cold}^{0.34} \cdot \left(\frac{\mu_{cold,bulk}}{\mu_{cold,wall}}\right)^{0.26} \tag{3.50}$$

Tube layout	a	m	Reynolds
$Square$	0.742	0.431	$Re \leq 300$
	0.211	0.651	$300 < Re \leq 2 \cdot 10^5$
	0.116	0.7	$2 \cdot 10^5 < Re \leq 2 \cdot 10^6$
$Triangular$	1.309	0.36	$Re \leq 300$
	0.273	0.635	$300 < Re \leq 2 \cdot 10^5$
	0.124	0.7	$2 \cdot 10^5 < Re \leq 2 \cdot 10^6$

Table 3.4.4: Constants for use in equation (3.50) [40]

where Reynolds (Re_{cold}) and Prandtl (Pr_{cold}) numbers can be calculated as indicated in equation (3.51). The constants a and m are reported in Table 3.4.4 as function of tube layout and Reynolds number. The ratio $\mu_{cold,bulk}/\mu_{cold,wall}$ corrects for the variation in dynamic viscosity between the surface and the bulk. In detail, $\mu_{cold,bulk}$ is calculated at the average shell-side fluid temperature, while $\mu_{cold,wall}$ is found at the wall temperature.

$$Re_{cold} = \frac{\rho_{cold} \cdot v_{shell} \cdot d_o}{\mu_{cold}} \qquad Pr_{cold} = \frac{\mu_{cold} \cdot c_{p,cold}}{\lambda_{cold}} \tag{3.51}$$

where the shell-side fluid velocity, v_{shell}, can be calculated rewriting equation (3.28):

$$v_{shell} = \frac{\dot{m}_{cold}}{S_m \cdot \rho_{cold}} \tag{3.52}$$

where S_m is the minimal crossflow area calculated in equation (3.29).

The segmental baffle window correction factor, J_C, the shell-to-baffle and tube-to-baffle clearances factor, J_L, the correction factors for bundle bypass effects for heat transfer J_B are calculated respectively in equation (A.17), (A.21), and (A.22) in appendix A.3.1.

Overall heat transfer coefficient

The overall heat transfer coefficient can be evaluated as function of the shell-side and tube-side HTC.

$$U = \left(\frac{1}{h_s} + R_s + \frac{1}{h_t} \cdot \frac{d_o}{d_i} + \frac{d_o \cdot \ln(\frac{d_o}{d_i})}{2 \cdot \lambda_{wall}}\right)^{-1} \tag{3.53}$$

where R_s is the fouling resistance that can be user-defined according to the fluid utilized.

3.4.4 Pressure losses calculation

In this section, the procedure to estimate pressure losses on the shell and tube side is presented.

Tube-side pressure drop

In order to estimate the tube-side pressure drop, Frank's method is adopted. It takes into account the friction loss in the tubes and the pressure drop due to geometry discontinuities that the fluid faces through the tube bundle. In detail, Frank's method recommends a velocity head per pass value equal to 2.5 and according to [32], it is the most realistic value to use. The pressure drop can be calculated using equation (3.54).

$$\Delta p_t = N_p \cdot \left(8 \cdot j_f \frac{L}{d_i} \left(\frac{\mu_{hot,bulk}}{\mu_{hot,wall}}\right)^{-m} + 2.5\right) \cdot \frac{\rho_{hot} \cdot v_{tube}^2}{2} \tag{3.54}$$

where j_f is the dimensionless friction factor (equation (3.56)), and the exponent m (equation (3.55)) assumes different values for laminar or turbulent flow:

$$m = \begin{cases} 0.25 & \text{if } Re \leq 2100 \\ 0.14 & \text{if } Re > 2100 \end{cases} \tag{3.55}$$

$$j_f = \begin{cases} 8.1274 \cdot Re^{-1.011} & \text{if } Re \leq 855 \\ 0.046 \cdot Re^{-0.244} & \text{if } Re > 855 \end{cases} \tag{3.56}$$

The dimensionless friction factor was interpolated from figure A.4.1, available in appendix A.4.1.

Shell-side pressure drop

According to [41], the shell-side pressure drop given by Bell-Delaware method is the most realistic because it considers bypass and leakage streams caused by the baffles in the heat exchanger. The elements of the shell-side pressure drop are presented in figure 3.4.3.

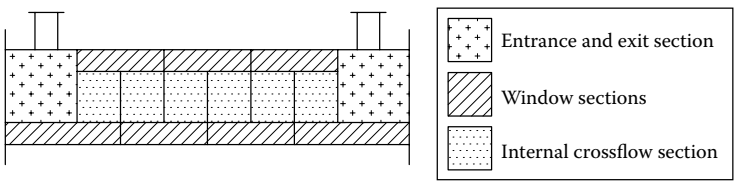

Figure 3.4.3: Shell-side pressure drop elements [33]

As suggested by [42], the total shell-side pressure drop (Δp_s) consists of the sum of the pressure drop due to crossflow (Δp_c), window region (Δp_w) and entrance and exit regions (Δp_e).

Thus, in formula the total pressure drop can be expressed as:

$$\Delta p_s = \Delta p_c + \Delta p_w \cdot N_b \cdot R_L + \Delta p_e \tag{3.57}$$

The pressure drop due to crossflow (Δp_c) can be calculated as shown in equation (3.58).

$$\Delta p_c = (N_b - 1) \cdot \Delta p_{b,i} \cdot R_B \cdot R_L \tag{3.58}$$

where $\Delta p_{b,i}$ is the ideal tube bank pressure drop (equation (3.59)), while R_B is the correction factor for bundle bypass effects for pressure drop and R_L is the correction factor for baffle leakage effects for pressure drop (both available in appendix A.4.2, equation (A.23) and (A.24)).

$$\Delta p_{b,i} = N_c \cdot K_f \cdot \frac{\rho_{cold} \cdot v_{shell}^2}{2} \tag{3.59}$$

where K_f is the friction factor which depends on the Reynolds number and on the tube layout. The correlations are reported in appendix A.4.2 for the tube arrangements considered (equation (A.25) and (A.26)).

The pressure drop due to the window region Δp_w, can be found as:

$$\Delta p_w = \frac{2 + 0.6 \cdot N_{cw}}{2 \cdot S_m \cdot S_w \cdot \rho_{cold}} \cdot \dot{m}_{cold}^2 \tag{3.60}$$

Instead, the pressure drop due to entrance and exit regions Δp_e is given by:

$$\Delta p_e = 2 \cdot \Delta p_{b,i} \cdot R_B \cdot \left(1 + \frac{N_{cw}}{N_c}\right) \tag{3.61}$$

Therefore, the total shell-side pressure drop can be expressed as in equation (3.62).

$$\Delta p_s = N_{sp} \cdot \left[((N_b - 1) \cdot \Delta p_{b,i} \cdot R_B + N_b \cdot \Delta p_w) \cdot R_L + 2 \cdot \Delta p_{b,i} \cdot R_B \cdot \left(1 + \frac{N_{cw}}{N_c}\right)\right] \tag{3.62}$$

3.4.5 Cost estimation

The aim of this section is to present the cost functions implemented in the HX model to estimate investment cost and annual costs.

Investment cost

The first approach implemented to estimate the HX investment cost is the one suggested by Turton [43]. Turton proposes a methodology, which is based on a survey of equipment manufacturers, to calculate the purchased cost of several conventional equipment types typically utilized in chemical processes. In detail, the heat exchanger investment cost is function of the heat transfer area, chosen configuration, material selected, and pressure. Turton's method proposes equation (3.63) to calculate the purchased cost of the equipment, at ambient operating pressure and using carbon steel construction, on top of which it applies several correction factors.

$$\log_{10} C_p^0 = K_1 + K_2 \cdot \log_{10} A_{HX} + K_3 \cdot [\log_{10} A_{HX}]^2 \tag{3.63}$$

where K_1, K_2, and K_3 are chosen for fixed tube heat exchanger and their values are respectively 4.3247, -0.3030, and 0.1634. According to [43], the cost function is valid only for $10 < A_{HX} < 1000\,[m^2]$. This represents the most critical limit of this approach. The first correction factor that needs to be applied is the pressure factor F_P. It takes into account the extra material, and, thus, the extra cost required if the pressure on the shell or on the tube side is higher than the atmospheric pressure. F_P can be calculated as indicated in equation (3.64).

$$\log_{10} F_P^0 = C_1 + C_2 \cdot \log_{10} P_{cost} + C_3 \cdot [\log_{10} P_{cost}]^2 \tag{3.64}$$

where P_{cost} is the pressure in $barg$ and the constant C_1, C_2, and C_3 are reported in table 3.4.5 as function of the pressure range and of theHX area pressurized. Then, the

Equipment description	C_1	C_2	C_3	Pressure range [barg]
Both shell and tube	0 0.03881	0 -0.11272	0 0.08183	$P_{cost} < 5$ $5 < P_{cost} < 140$
Tube only	0 -0.00164	0 -0.0627	0 0.0123	$P_{cost} < 5$ $5 < P_{cost} < 140$

Table 3.4.5: Constants for pressure correction factor equation [43]

material correction factor (F_M) needs to be applied. It takes into account the extra cost due to different HX material considered. F_M value can be found utilizing figure A.5.1 and table A.5.2, in Appendix A.5.
Finally, the last correction factor is utilized to update the equipment purchased cost to 2020. Equation (3.65) shows how the updated cost is calculated using the widely accepted Chemical Engineering Plant Cost Index (CEPCI). Turton's cost function refers to year 2001 (CEPCI=397), while the most recent available CEPCI is the one from 2018 and it is equal to 603 [44].

$$C^0_{p,2018} = C^0_p \cdot \frac{CEPCI_{2018}}{CEPCI_{2001}} \tag{3.65}$$

Thus, the HX investment cost can be estimated using equation (3.66).

$$C_{inv} = C^0_{p,2018} \cdot (B_1 + B_2 \cdot F_M \cdot F_P) \tag{3.66}$$

For a shell and tube configuration, the constants B_1 and B_2 are respectively equal to 1.63 and 1.66.
The principal limit of the Turton cost function is its applicability. Indeed, since it can be utilized for heat exchanger with a heat transfer area up to of 1000 m^2, an alternative approach needs to be outlined.
For this purpose, for larger heat exchangers, a new cost function needs to be defined. In particular, it is expected to have an investment cost that, increasing the heat transfer area, always increases and that respects the economy scale: the investment cost as function of the heat transfer area should be concave downward. Equation (3.67) shows how the new cost function is defined.

$$C_{inv} = c_{material} \cdot F_{ma} \cdot M_a \cdot A_{HX} \tag{3.67}$$

where $c_{material}$ is the mass specific material cost, F_{ma} is the manufacturing factor, M_a is the mass over area factor, and A_{HX} is the heat transfer area.
In detail, the *mass specific material cost* is the bare material cost per kilogram and it needs to be user-defined according to the selected HX material.
The *manufacturing factor* is a correction factor to convert the bare material cost into the equipment specific cost, as equation (3.68). This factor is assumed to be function of the heat transfer area and tends asymptotically to F_{min}. The minimum manufacture

factor is assumed equal to 1.65 according to experts from University of South Australia.

$$F_{ma} = F_{min} + c \cdot A_{HX}^{-m} \tag{3.68}$$

where the two constants c and m need to be found using two known cost values for two heat transfer areas. In order to respect the economy scale, the exponent m needs to be between 0 and 1, and the constant c needs to be larger then 0.
Finally, the *mass over area factor* is assumed equal to $9.6\ kg/m^2$ according to the average heat exchanger mass over area value for the assumed tube diameter range.

Pumping cost

The pumping cost is considered the only HX annual cost and it is calculated using equation (3.69). According to [45], it is assumed an annual operating time (H_y) of 4500 hours/year, electricity cost (c_{power}) of 0.14 USD/kWhe, and pump efficiency (η_{pump}) of 70%. These values are assumed as starting point and a fine tuning is required based on the particular application.

$$C_{pump} = c_{power} \cdot \frac{H_y}{\eta_{pump}} \cdot \left(\frac{\dot{m}_{cold} \cdot \Delta p_{shell}}{\rho_{cold}} + \frac{\dot{m}_{hot} \cdot \Delta p_{tube}}{\rho_{hot}} \right) \tag{3.69}$$

3.4.6 Objective function calculation

The objective function needs to be user-defined according to the requirements of the particular application in which the model will be utilized. In case of absence of specific requirements, according to [45] theTotal Annualized Cost (TAC) can be utilized as objective function. The TAC takes into account both capital and operation costs and it can be calculated as indicated in equation (3.70). Minimize the TAC means find a HX configuration that represents a compromise between minimum investment cost and minimum pumping cost.

$$TAC = f \cdot C_{inv} + C_{pump} \tag{3.70}$$

where f is the annuity factor and it is given by:

$$f = \frac{r \cdot (1+r)^n}{(1+r)^n - 1} \tag{3.71}$$

where n is the considered heat exchanger lifetime, assumed equal to 30 years, and r is the real interest rate, assumed equal to 5%.

Chapter 4

Sodium-Salt-sCO2 CSP system model

In this chapter, the sodium-salt-sCO2 CSP system model is presented, describing the components developed and introducing the principal techno-economic assumptions. The model is now available in the *SolarTherm* library[1] and a schematic representation is provided in figure 4.0.1.

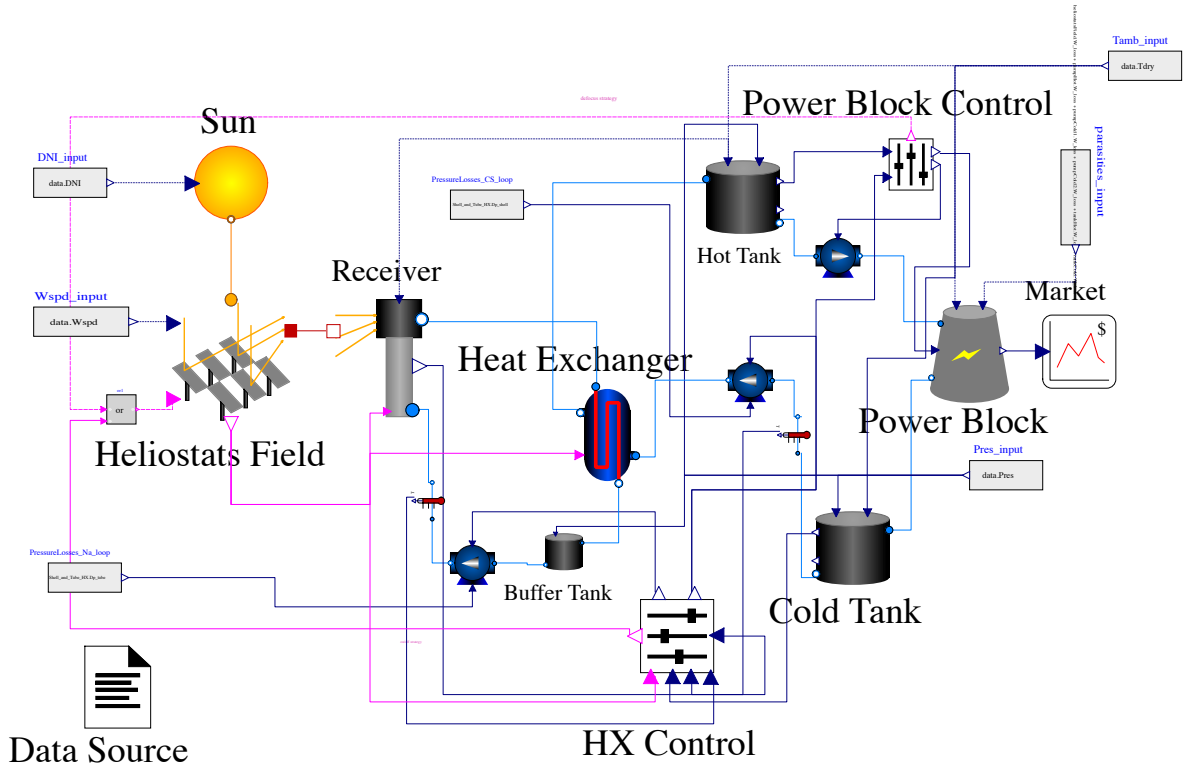

Figure 4.0.1: *NaSaltsCO2System* model

[1] https://github.com/SolarTherm/SolarTherm/blob/SaltCO2System/examples/NaSaltsCO2System.mo

The *NaSaltsCO2System* model was developed starting from an existing model implemented by A. Shirazi and A. Fontalvo, the *SaltsCO2System*, which was adopting conventional solar salts in a direct two tanks storage system (appendix B.1, figure B.1.1). In the *NaSaltsCO2System* model, liquid sodium is used as HTF in the receiver, allowing receiver operating temperatures of 740 - 520 °C, and a novel ternary eutectic chloride salt is adopted as storage fluid in a two tank indirect system. The advanced chloride salt allows to store thermal energy at temperatures around 720°C. The sodium loop, localized between the sodium receiver and the heat exchanger, represents the main difference compared with the reference system. Therefore, the existing components were adapted to the new media and to the new temperature set-point values, and new component models were developed and integrated. The *Heat Exchanger* model was the focus point of this work and a description of the model is available in chapter 3. The *HX Control* model and the *Buffer Tank* were developed ad-hoc for the *NaSaltsCO2System* model. The integration of the components was a challenging process that demanded a lot of effort in order to achieve the model stability and robustness required to estimate performances and costs of the system. In the following, all the components employed in the model are described, providing inputs, outputs, characteristic parameters, main equations and cost assumptions.

4.1 Sun

The *Sun* model receives as input location information (latitude and longitude) and the weather file, manually provided by the user for the specific place where the CSP plant is sited. For each time-step, the *Sun* model provides as output the Direct Normal Irradiance (DNI) value and the sun position (declination and hour angle).

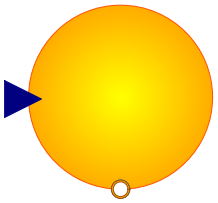

Figure 4.1.1: *Sun* model

4.2 Heliostats Field

The *Heliostats Field* model needs to be customized providing the single heliostat area (A_h), the number of heliostats (n_h) and the heliostat availability as a percentage of the total operating hours (he_{av}). The model, receiving as input the DNI and the sun position from the *Sun*, the wind speed (w_{sp}) from the weather file, and the *defocus* boolean variable from the control system, provides for each time step the heat flux concentrated on the surface of the receiver (Q_{net}) and a boolean variable *on* that indicates when the heliostats field is operating. Moreover, the power consumed by the tracking system (W_{loss}) is calculated and included in the parasitic losses of the system.

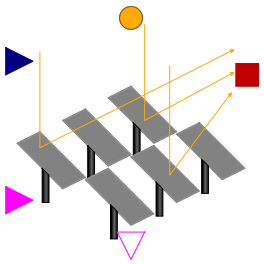

Figure 4.2.1: *Heliostats Field* model

The heliostats field layout needs to be externally defined and the corresponding average optical efficiency ($\eta_{opt,av}$) is then provided as a lookup table function of the sun position. Technical parameters are pre-set based on National Renewable Energy Laboratory (NREL) Gen3 SAM model v14.02.2020 and they are summarized in table 4.2.1.

Parameter	Description	UM	Value
A_h	Heliostat area	m^2	144
he_{av}	Heliostat availability	%	99
ν_{start}	Receiver energy start-up fraction	-	0.6
ν_{min}	Minimum receiver turn-down energy fraction	-	0.3
$\nu_{defocus}$	Receiver limiter energy fraction at defocus state	-	1
W_{track}	Tracking power for a single heliostat	W	55
E_{start}	Start-up energy of a single heliostat	kJ	90
ele_{min}	Heliostat stow deploy angle	deg	14
$w_{spd,max}$	Maximum wind stow speed	m/s	15

Table 4.2.1: Technical parameters - *Heliostat Field* model

4.2.1 Main equations

The heat flux that the heliostats field can concentrate on the receiver surface is calculated as provided in equation (4.1).

$$Q_{raw} = A_h \cdot n_h \cdot he_{av} \cdot DNI \cdot \eta_{opt} \tag{4.1}$$

In reality, the heliostats field can operate only when the following conditions are satisfied: the sun elevation needs to be higher than the minimum acceptable value ($ele > ele_{min}$), the wind speed needs to be lower than the maximum value ($w_{sp} < w_{sp,max}$), and the heat flux concentrated on the receiver surface needs to be higher than the minimum necessary to operate the receiver ($Q_{raw} > Q_{min}$). Only when all the aforementioned conditions are verified, the boolean variable *on* will be equal to true. The heat flux actually concentrated on the surface of the receiver is calculated as indicated in equation (4.2).

$$Q_{net} = \begin{cases} Q_{raw} & \text{if } on = true \text{ and } defocus = false \\ \min(Q_{raw}, Q_{defocus}) & \text{if } on = true \text{ and } defocus = true \\ 0 & \text{if } on = false \end{cases} \tag{4.2}$$

The power demand for the tracking system (W_{loss}) is calculated summing up two contributes: the start-up consumption ($W_{loss,start}$) and the consumption during operating conditions ($W_{loss,op}$). Each contribution can be calculated as provided respectively in equation (4.3) and (4.4).

$$W_{loss,start} = n_h \cdot he_{av} \cdot damping \cdot E_{start}/t_{start} \tag{4.3}$$

$$W_{loss,op} = \begin{cases} n_h \cdot he_{av} \cdot damping \cdot W_{track} & \text{if } ele > 0 \\ 0 & \text{if } ele = 0 \end{cases} \tag{4.4}$$

where t_{start} is the time necessary to start-up the heliostats and the $damping$ is calculated as the fraction between the net heat flux reflected by the heliostats (Q_{net}) over the maximum heat flux that can be reflected (Q_{raw}).

4.2.2 Cost function

The heliostats field investment cost is estimated (in USD) according to [13], as indicated in equation (4.5).

$$C_{field} = 75 \cdot A_{field} \tag{4.5}$$

where A_{field} is the area of the solar field calculated as the product between the number of the heliostats and the area of the single heliostat.

4.3 Receiver

The *Receiver* model receives as input the incoming heat concentrated by the solar field on the receiver surface (Q_{flow}), the boolean on from the *Heliostats Field* model, and the sodium flowing into the receiver with a specific mass flow rate ($m_{flow,Na}$) and inlet enthalpy value ($h_{Na,in}$). For each time-step, the *Receiver* model provides as output the outlet enthalpy value ($h_{Na,out}$) and the heat extracted (Q_{out}). The receiver design is externally defined in terms of receiver height (H_{rec}) and diameter (D_{rec}), taking into account the solar field layout, the receiver operating temperatures, and the maximum heat flux allowable on the receiver surface resulting from thermal stresses analysis for a specific material. Accordingly, for the specific design proposed, the receiver thermal efficiency (η_{th}) is estimated and provided as a function of the incoming heat (Q_{flow}) and of the ambient temperature (T_{amb}).

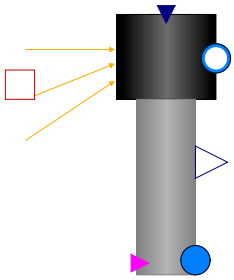

Figure 4.3.1: *Receiver* model

4.3.1 Main equations

The thermal efficiency can be calculated as indicated in equation (4.6).

$$\eta_{th} = C_0 + C_1 \cdot \log_{10} Q_{flow} + C_2 \cdot (\log_{10} Q_{flow})^2 + C_3 \cdot (\log_{10} Q_{flow})^3 + C_4 \cdot (\log_{10} Q_{flow})^4 \tag{4.6}$$

where the constants C_0, C_1, C_2, C_3, C_4 needs to be provided according to the specific use case. Then, the thermal losses in the receiver (Q_{loss}) and the heat extracted (Q_{out}) are estimated following respectively equation (4.7) and equation (4.8)

$$Q_{loss} = Q_{flow} \cdot (1 - \eta_{th}) \tag{4.7}$$

$$Q_{out} = Q_{flow} \cdot \eta_{th} \tag{4.8}$$

The sodium outlet enthalpy value (h_{out}) is calculated from the thermal power balance indicated in equation (4.9)

$$Q_{flow} = Q_{loss} + m_{flow,Na} \cdot (h_{Na,out} - h_{Na,in}) \tag{4.9}$$

For what concerns the tower, the diameter is considered equal to the receiver diameter, while the height (H_{tower}) is calculated as function of the gross solar field area ($A_{field,gross}$) following equation (4.10)

$$H_{tower} = 0.154 \cdot (1.25 \cdot A_{field,gross}/\pi)^{0.5} \tag{4.10}$$

4.3.2 Cost function

The receiver cost is estimated following SAM default approach assuming a receiver reference cost of 105.1 MUSD and a reference receiver area equal to 1571 m^2. The cost function is shown in equation (4.11)

$$C_{receiver} = C_{receiver,ref} \cdot (A_{receiver}/A_{receiver,ref})^{0.7} \tag{4.11}$$

The tower cost is estimated using equation (4.12). For tower height larger than 120 m, a concrete tower is preferred, while latticework steel towers are utilized for smaller sizes. The cost function for concrete tower is chosen based on the analysis of tower costs according to the Abengoa report, while for the latticework steel tower different constants are considered in order to fit 125 kUSD for a 50 m tower.

$$C_{tower} = \begin{cases} 80816 \cdot \exp(0.00879 \cdot H_{tower}) & \text{if } H_{tower} \leq 120 \\ 7612816 \cdot \exp(0.0113 \cdot H_{tower}) & \text{if } H_{tower} > 120 \end{cases} \tag{4.12}$$

4.4 Buffer Tank

The *Buffer Tank* model is included to be a loop-breaker for the sodium loop. The model receives as inputs the pressure (p_{top}) of the sodium loop and the inlet enthalpy ($h_{in,bt}$) and mass-flow rate ($m_{flow,in,bt}$) from the heat-exchanger model. According to the required sodium mass flow rate, imposed by the control system, the outlet mass flow rate ($m_{flow,out,bt}$) is provided. Thus, the model provides as output the receiver inlet enthalpy (h_{stored}).

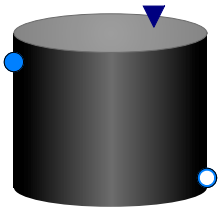

Figure 4.4.1: *Buffer Tank* model

The model is only a fictitious model that simplifies the resolution of the set of equations that models the sodium loop. Consequently, no cost data and no dimensions of the tank are considered.

4.4.1 Main equations

Equation (4.13) and equation (4.14) shows respectively the mass flow rate and the thermal power balance. m_{stored} represents the sodium mass stored in the buffer tank.

$$\frac{dm_{stored}}{dt} = m_{flow,in,bt} - m_{flow,out,bt} \tag{4.13}$$

$$m_{stored} \cdot \frac{dh_{stored}}{dt} + \frac{dm_{stored}}{dt} \cdot h_{stored} = m_{flow,in,bt} \cdot h_{in,bt} + m_{flow,out,bt} \cdot h_{stored} \tag{4.14}$$

4.5 Pump

The *pump* model receives as input the medium mass flow rate (m_{flow}) calculated in the control system at any time steps, the pressure losses of the circuit (Δp_{losses}) and the inlet fluid enthalpy ($h_{in,pump}$). The model imposes the fluid mass flow rate in the

circuit where it is employed and it provides the outlet fluid enthalpy value ($h_{out,pump}$). Moreover, it estimates the electricity needed to circulate the fluid (W_{loss}).

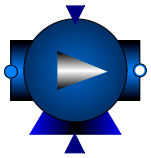

Figure 4.5.1: *Pump* model

4.5.1 Main equations

Mass flow rate and enthalpy continuities are imposed in the model as indicated in equation (4.15) and equation (4.16).

$$m_{flow,pump,in} = m_{flow,pump,out} = m_{flow} \tag{4.15}$$

$$h_{out,pump} = h_{in,pump} \tag{4.16}$$

The electricity required by the pump is calculated following equation (4.17). The electric-to-mechanic efficiency of the pump (η_{pump}) was assumed equal to 0.75, the loss factor (k_{loss}) that takes into account the piping losses was assumed equal to 0.21 kJ/kg for the sodium pump, 0.15 kJ/kg for the chloride salt pump (cold tank - HX), and 0.55 kJ/kg for the chloride salt pump (power block). The pressure losses (Δp_{losses}) estimated in the components of the circuit needs to be provided as input.

$$W_{loss} = m_{flow} \cdot k_{loss} + m_{flow} \cdot \Delta p_{losses} / \rho_{medium} / \eta_{pump} \tag{4.17}$$

4.6 HX Control

The *HX Control* model imposes the mass flow rate flowing in the sodium loop circuit ($m_{flow,rec}$) and the mass flow rate of the chloride salt heated up in the heat exchanger ($m_{flow,hs}$), in order to achieve the set-point temperatures. The model receives as input the heat extracted from the receiver ($Q_{out,rec}$), the receiver sodium inlet temperature ($T_{input,rec}$), and the cold tank chloride salt outlet temperature ($T_{output,cs}$). Consequently, the mass flow rates are calculated in order to transfer in the heat exchanger the same

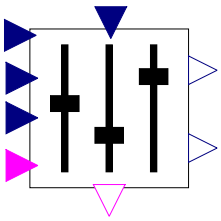

Figure 4.6.1: *HX Control* model

thermal power extracted from the receiver. Moreover, the control system checks the cold storage level (L_{mea}) to impose defocus mode if the level exceeds min/max acceptable limits. The boolean variable on from the heliostats field model is another input that guarantees that the mass flow rates will be different than zero only when the solar resource is available. A detailed description of the control system is provided in figure 4.6.2.

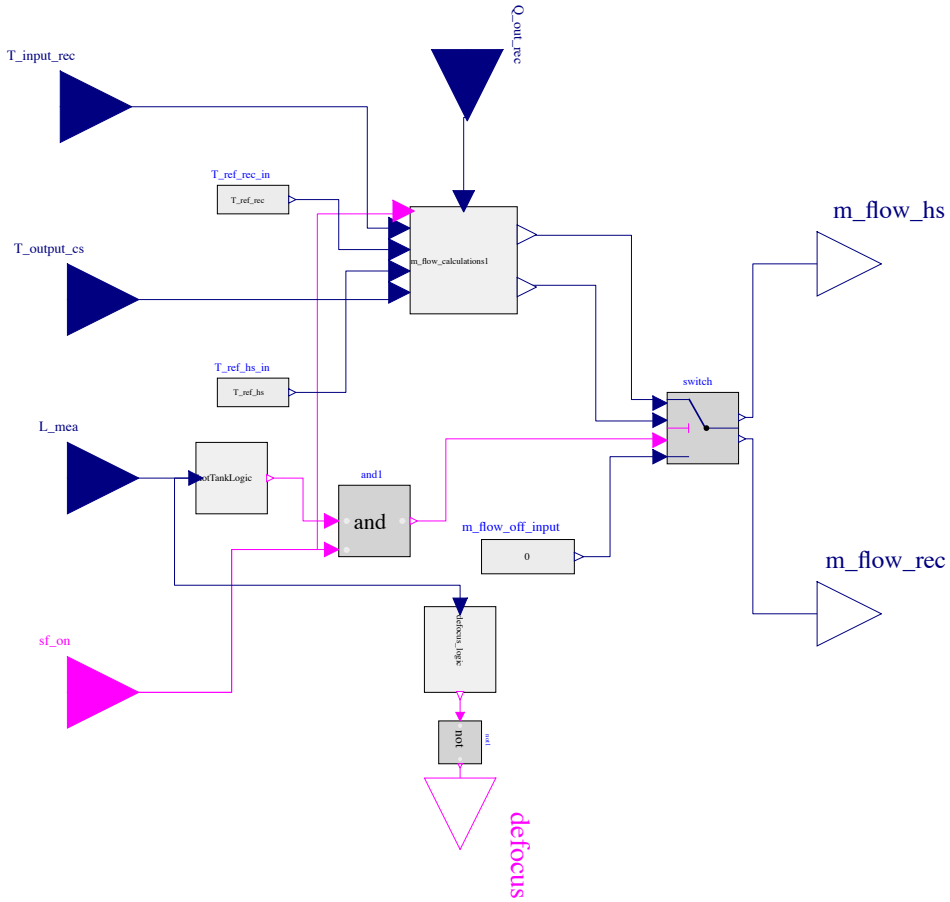

Figure 4.6.2: *HX Control* model

4.6.1 Main equations

Inside the *m_flow_calculation* block, the sodium enthalpies $h_{Na,1}$ and $h_{Na,2}$ are calculated respectively as function of the set-point temperature $T_{ref,rec}$ equal to $740\ °C$, and of the receiver inlet temperature $T_{input,rec}$. Similarly, $h_{CS,1}$ and $h_{CS,2}$ are calculated as function of $T_{ref,hs}$ equal to $720\ °C$, and $T_{output,cs}$. Then, the mass flow rates are obtain from the thermal power balances indicated in equation (4.18) and (4.19).

$$m_{flow,rec} = Q_{out,rec}/(h_{Na,1} - h_{Na,2}) \tag{4.18}$$

$$m_{flow,hs} = Q_{out,rec}/(h_{CS,2} - h_{CS,1}) \tag{4.19}$$

In the *m_flow_calculation* block, it is employed also a limiter that guarantees that the mass flow rates range and do not exceed user defined minimum and maximum limits.

4.7 Cold/Hot Tank

The *Cold/Hot Tank* model receives as inputs the pressure (p_{top}) of the circuit where it is employed, the ambient temperature (T_{amb}), and the inlet enthalpy ($h_{in,t}$) and mass-flow rate ($m_{flow,in,t}$) of the incoming fluid. The outlet mass flow rate ($m_{flow,out,t}$) is provided according to the mass flow rate imposed by the control system. Thus, the model provides as output the enthalpy value of the stored medium (h_{stored}) and the storage level (L_{mea}). In addition, it can provide the average temperature value of the stored medium (T_{medium}). In the *Cold/Hot Tank* model, the power required to heat the medium by means of an electrical heater ($W_{loss,ht}$) is estimated too.

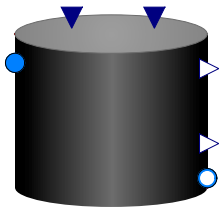

Figure 4.7.1: *Tank* model

The model needs to be customized providing the tank diameter ($D_{storage}$) and height ($H_{storage}$). Other parameters were pre-set based on NREL Gen3 SAM model v14.02.2020 and are reported in table 4.7.1.

Parameter	Description	UM	Value
α	Heat transfer coefficient with the ambient	$W/m^2/K$	0.4
$W_{max,hot,t}$	Hot tank heater capacity	MW	30
$W_{max,cold,t}$	Cold tank heater capacity	MW	15
$T_{set,hot}$	Hot tank heater set-point temperature	$°C$	575
$T_{set,cold}$	Cold tank heater set-point temperature	$°C$	450
η_{ht}	Auxiliary heater efficiency	%	99

Table 4.7.1: Technical parameters - *Cold/Hot Tank* model

4.7.1 Main equations

Equation (4.20) and equation (4.21) shows respectively the mass flow rate and the thermal power balance in the tank. m_{stored} represents the medium mass stored in the tank at the temperature of T_{stored}.

$$\frac{dm_{stored}}{dt} = m_{flow,in,t} - m_{flow,out,t} \tag{4.20}$$

$$m_{stored} \cdot \frac{dh_{stored}}{dt} + \frac{dm_{stored}}{dt} \cdot h_{stored} = m_{flow,in,t} \cdot h_{in,t} + m_{flow,out,t} \cdot h_{stored} \tag{4.21}$$

The total volume of the tank is calculated following equation (4.22) and the volume occupied at each time step is calculated as indicated in equation (4.23).

$$V_t = (H_{storage} \cdot \pi \cdot D^2_{storage})/4 \tag{4.22}$$

$$V = m_{stored}/\rho_{medium} \tag{4.23}$$

Consequently, the tank level is calculated as shown in the equation (4.24).

$$L_{mea} = V/V_t \cdot 100 \tag{4.24}$$

The exchange area ($A_{ex,t}$) and the tank thermal losses ($Q_{loss,ht}$) are calculated following equation (4.25) and (4.26).

$$A_{ex,t} = \pi \cdot D_{storage} \cdot H_{storage} \cdot (L_{mea}/100) + \pi \cdot D^2_{storage}/4 \tag{4.25}$$

$$Q_{loss,ht} = A_{ex,t} \cdot \alpha \cdot (T_{medium} - T_{amb}) \tag{4.26}$$

Thus, the electrical power losses are estimated as shown in equation (4.27).

$$W_{loss,ht} = \begin{cases} min(Q_{loss,ht}, W_{max,t})/\eta_{ht} & \text{if } T_{medium} \leq T_{set} \\ 0 & \text{if } T_{medium} > T_{set} \end{cases} \tag{4.27}$$

4.7.2 Cost function

The cost of the storage depends on the capacity ($t_{storage}$) and on the power block design thermal power ($Q_{flow,des}$). Thus the maximum tank stored energy (in kWh) can be calculated as shown in equation (4.28).

$$E_{max} = t_{storage} \cdot Q_{flow,des}/1000 \tag{4.28}$$

Therefore, the cost is estimated according to the guidelines provided in the Gen 3 CSP Down-Selection Criteria [3], assuming an energy specific cost of 40 USD/kWh.

$$C_{storage} = 40 \cdot E_{max} \tag{4.29}$$

4.8 Power Block

The *Power Block* model provides the net electric power produced (W_{net}), the electricity that can be fed into the grid (E_{net}), and the returning chloride salt enthalpy value (h_{out}). The power block receives as inputs the chloride salt mass flow rate (m_{flow}) and inlet enthalpy value (h_{in}), the ambient temperature (T_{amb}), the parasitic losses (W_{par}), and a boolean variable (PB_{ramp}) that distinguishes switch on/off dynamics from the normal operating conditions. Moreover, the design conditions need to be specified in terms of operating inlet temperature ($T_{in,ref}$), nominal gross power ($P_{gross,des}$), nominal inlet thermal power ($Q_{flow,ref}$), and cooling design power ($W_{cool,ref}$).

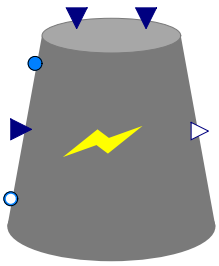

Figure 4.8.1: *Power Block* model

The model is not a physical model, but it is based on the power block model available in NREL Gen3 SAM model v14.02.2020. In detail the performances of the power block are evaluated by means of three variables k_q, k_w, and ν_w, obtained by interpolation of the SAM power block model. These parameters are a function of the ambient temperature, of the inlet chloride salt enthalpy value, and of the load of the power block.

4.8.1 Main equations

The thermal power provided to the power block can be calculated using the parameter k_q as indicated in equation (4.30). Consequently, applying the thermal power balance, equation (4.31), the outlet chloride salt enthalpy value can be calculated.

$$Q_{flow}/Q_{flow,ref} = k_q \tag{4.30}$$

$$Q_{flow} = m_{flow} \cdot (h_{in} - h_{out}) \tag{4.31}$$

The gross electric power produced is estimated using the parameter k_w as indicated in equation (4.32), whereas the cooling power is estimated by means of the parameter ν_w, equation (4.33).

$$W_{gross}/P_{gross,des} = k_w \tag{4.32}$$

$$W_{cooling}/W_{cool,des} = \nu_w \tag{4.33}$$

Consequently, the power block efficiency (η_{PB}), equation (4.34), the electric power losses, equation (4.35), and the net electric power produced, equation (4.36), can be calculated.

$$\eta_{PB} = W_{gross}/Q_{flow} \tag{4.34}$$

$$W_{loss} = W_{base} + W_{par} + W_{cooling}; \tag{4.35}$$

where W_{base} is the power consumed at all times.

$$W_{net} = W_{gross} - W_{loss} \tag{4.36}$$

In the end, the electricity fed into the grid is calculated as shown in equation (4.37).

$$\frac{dE_{net}}{dt} = (1 - \nu_{sys}) \cdot W_{net} \tag{4.37}$$

where ν_{sys} is the system availability loss factor that accounts for system outages and other events.

4.8.2 Cost function

The power block cost is estimated according to [3], assuming a specific cost of 900 USD/kWe, as indicated in equation (4.38).

$$C_{PB} = 900 \cdot P_{gross,des}/1000 \tag{4.38}$$

4.9 Power Block Control

The *Power Block Control* model provides as outputs the mass flow rate value flowing from the hot storage to the power block ($m_{flow,out}$), the boolean variable (PB_{ramp}) that distinguishes switch on/off dynamics from the normal operating conditions, and the $defocus$ boolean variable that impose defocus mode if the hot tank level is lower than the minimum or higher than the maximum acceptable. The model receives as inputs the inlet hot tank mass flow rate ($m_{flow,in}$) and the level of the hot tank (L_{mea}).

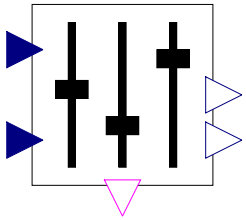

Figure 4.9.1: *Power Block Control* model

According to $m_{flow,in}$ and L_{mea} variation, the power block control distinguishes different operating conditions: start-up, discharge, charge and stand-by mode. Consequently, for each operating mode, the mass flow rate will assume a different value, fraction of the nominal mass flow rate.

Chapter 5

Design Sodium-Salt HX

In this chapter, the procedure followed to design the sodium-chloride salt shell and tube heat exchanger is provided. Essentially, this represents just a particular application of the general heat exchanger model presented in chapter 3, where sodium is the hot fluid and chloride salt is the cold one. According to figure 3.2.2, in order to customize the model, media, BCs, constraints, fluid dependent correlations, and objective function need to be defined. Therefore, the necessary steps that lead to the definition of the HX design are presented in the following.

5.1 Media

The media involved in the HX are the shell-side fluid, the tube-side fluid, and the HX material. As mentioned in section 3.2, in order to reduce thermal losses, it is recommended to place the hot fluid on the tube-side and the cold one on the shell-side. Additionally, since sodium is utilized, safety precautions need to be taken and its confinement should be guaranteed. For these reasons, sodium is placed on the tube-side, while chloride-salts are on the shell-side. Furthermore, based on the fluid considered, temperature levels, corrosion matters and durability, Haynes230 (H230) was selected as the HX material. In the following, properties and assumptions related to the media are provided.

5.1.1 Tube-side fluid

As mentioned above, sodium (Na) is the tube-side fluid. Correlations for the most relevant properties such as density, specific heat capacity, dynamic viscosity, and thermal conductivity are collected according to [46], and reported in appendix C.1, in equations (C.1), (C.2), (C.4), and (C.3). The remaining properties, such as enthalpy, entropy..., can be calculated from the ones mentioned above.

5.1.2 Shell-side fluid

The fluid collocated on the shell-side is a novel ternary eutectic chloride salt (CS) with the following composition (% in weight): NaCl – KCl – MgCl2 (24.5%–20.5%–55%) [9]. According to NREL data, the density, specific heat capacity, dynamic viscosity, and thermal conductivity can be estimated using the correlations reported in appendix C.2, in equations (C.5), (C.6), (C.8), and (C.7).

Based on the fluids adopted, the fouling resistances are assumed. In detail, for molten salt $8.808 \cdot 10^{-5}\ (m^2 \cdot K)/W$ can be adopted in agreement with [47], [48], and [49]. On the contrary, fouling can be neglected in the case of sodium according to [7], [50].

5.1.3 Heat exchanger material

The heat exchanger material is selected according to the fluids considered, taking into account corrosion issues and maximum allowable stress in the temperature range of this application.

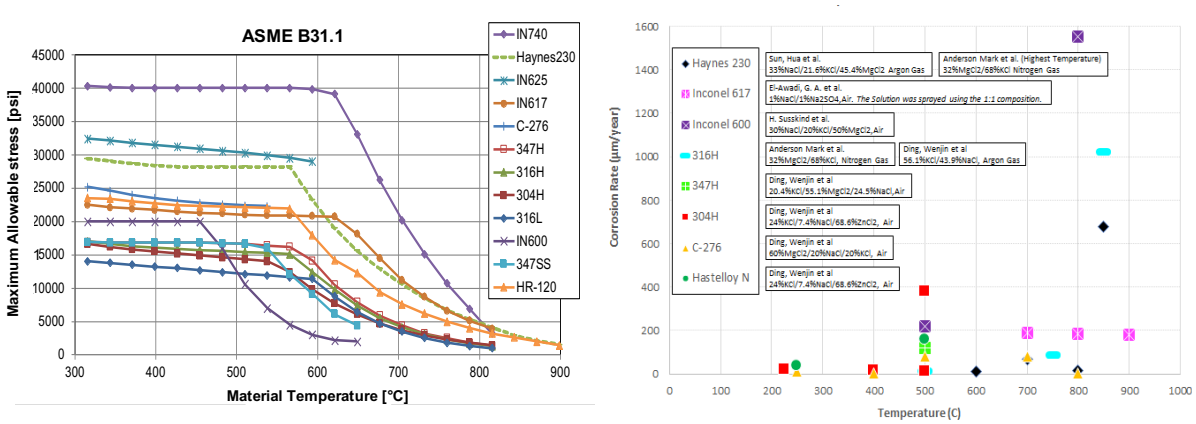

Figure 5.1.1: Maximum allowable stress (a) and corrosion rate (b) vs temperature for different candidate HX materials [51]

Figure 5.1.1 shows corrosion rate and maximum allowable stress for seamless piping for each candidate from ASME code. According to [51], no corrosion is found for Inconel 740H (In740H) in MgCl2 salt.

Besides In740H, figure 5.1.1 (b) shows that Haynes 230 (H230) presents the minimum corrosion rate in the temperature range of 700-750 °C. Additionally, figure 5.1.1 shows that In740H and H230 have also the maximum allowable stress in the same temperature range. According to [51], H230 is the recommended material for the hot side of the CSP plant. Consequently, the HX material selected is H230. In agreement with H230 brochure [52], the density, and thermal conductivity correlations are collected and reported respectively in equation (C.9) and (C.10) in appendix C.3.

The mass specific cost of H230 (c_{H230}), in congruence with NREL recommendation, can be considered equal to 84 USD/kg. Based on the mass specific material cost, the cost function provided in section 3.4.5 can be customized.

Cost Function

In line with section 3.4.5 and for the HX material assumed, the cost function can be estimated using equation (5.1).

$$C_{inv} = c_{H230} \cdot F_{ma} \cdot M_a \cdot A_{HX} \tag{5.1}$$

In order to customize the cost function, also the constants of F_{ma} correlation (equation (3.68)), c and m need to be determined. Therefore, since there are 2 unknowns, two known investment costs are necessary. The first one is calculated using Turton cost function (equation (3.66)), assuming a heat transfer area of 100 square meters and a material factor of 3.7 in line with [43]. Accordingly, the HX investment cost results:

$$C_{inv,100} = 0.278 \quad MUSD \tag{5.2}$$

The second known investment cost is calculated assuming that for a sufficiently large HX (1 $GWth$ - 20000 m^2) the manufacturing factor is equal to 1.95. The HX investment cost in million dollars is equal to:

$$C_{inv,20000} = 31.5 \quad MUSD \tag{5.3}$$

Consequently, the manufacturing factor as function of the heat transfer area is given by:

$$F_{ma} = F_{min} + 10 \cdot A_{HX}^{-0.37} \tag{5.4}$$

Therefore, the HX cost function is personalized according to the material selected.

5.2 Boundary Conditions

As mentioned in section 3.2, the boundary conditions that need to be defines are mainly temperature ranges, inlet pressures and thermal design power. Figure 5.2.1 summarizes the set-point values assumed for this particular application, at the design point. On the hot-side, sodium circulates in a closed loop from the receiver to the HX and vice-versa. On the cold side, chloride-salts stored on the cold storage flow in the HX and heated up they are store in the hot-storage. Neither of the two sides is pressurized.

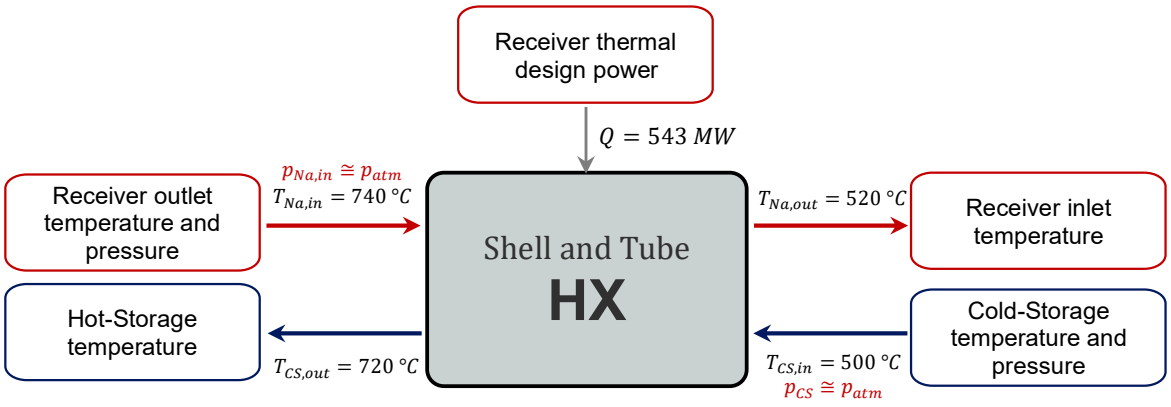

Figure 5.2.1: Boundary conditions sodium-chloride salts heat exchanger

The only two HX configurations that fit with the temperature range assumed are 1 shell pass, 1 tube pass (1:1 TEMA E STHE) and 2 shell passes, 2 tube passes (2:2 TEMA F STHE). Indeed, these configurations can be treated as pure counterflow HX and no constraints are imposed from the temperature correction factor ($F = 1$). For the other configurations, the temperature correction factor should be calculated as function of the temperatures. In particular, the temperature correction factor function implies receiver inlet temperatures higher then 630°C. Therefore, the configurations with multiple tube passes per shell pass are excluded.

5.3 Constraints

The HX length is constrained using the default value of maximum aspect ratio length over shell diameter equal to 10, while the velocity constraints are imposed in line with the media adopted and they are reported in the following.

5.3.1 Tube-side velocity constraints

Minimum and maximum sodium velocities are imposed according to [53]. In particular, recommended minimum and maximum values for sodium flowing in tubes are respectively equal to 1.2 and 2.4 m/s.

5.3.2 Shell-side velocity constraints

For the current ternary of chloride salts no pieces of indication are available for velocity constraints on the shell-side of the heat exchanger. Therefore, values for standard molten salts are considered. In detail, according to [45], a minimum salt velocity of 0.5 m/s is adopted. For the maximum salt velocity, instead, 1.5 m/s is used in line with [32] recommendation for liquid in shell-side.

5.4 Tube-side HTC

The methodology followed to estimate the tube-side HTC is shown in section 3.4.3 and the Nusselt (Nu) number as function of Reynolds (Re) and Prandtl (Pr) should be provided according to the fluid selected. In particular, due to their high conductivity, liquid metals feature low Pr number. Consequently, typical Nusselt correlations, usually expressed as a function of Re and Pr number can't be utilized. Alternatively, Nu can be found as function of the Peclet number (Pe) that is given by the product of Re and Pr [54]. In agreement with [55], the recommended correlation for liquid metals is the ChengeTak correlation [56]. Therefore, this correlation is adopted for sodium and it is presented in equation (5.5).

$$Nu = A + 0.018 \cdot Pe^{0.8} \tag{5.5}$$

with:

$$A = \begin{cases} 4.5 & \text{when } Pe \leq 1000 \\ 5.4 - 9 \cdot 10^{-4} \cdot Pe & \text{when } 1000 < Re \leq 2000 \\ 3.6 & \text{when } Pe \geq 2000 \end{cases} \tag{5.6}$$

5.5 Objective function

For this application, the objective function adopted is, by default, the TAC. Nevertheless, operating hours and cost of electricity are adapted according to the system performances. Indeed, since the pumping cost is considered a parasitic loss for the power block, the cost of electricity is assumed equal to the expected LCOE value (∼70 USD/MWhe) and the operating hours is assumed in line with the capacity factor CF (∼65%).

5.6 Design selection

In the previous sections, all the pieces of information necessary to customize the HX model are assumed. At this point, the model can be utilized to propose a specific HX design for the Na-Salt-sCO2 system and to simulate its annual performances. In order to define completely the HX design, an optimization is carried out to choose the set of design variables that minimize the TAC.

The TAC as function of tube outside diameter, pass length and number of passes is shown in figure 5.6.1. Although in table 3.4.1 the number of tubes is part of the design variables, TAC as function of the number of tubes is not shown explicitly in 5.6.1. In actual fact, the number of tubes is inversely proportional to the HX length value. Instead, for what concerns the tube arrangement, after preliminary investigations, the triangular tube layout is adopted because it leads always to a lower TAC. This results is in agreement with literature. Indeed, in [33], it is reported that triangular layouts provide better shell-side heat transfer coefficients and more compact arrangement.

Firstly, it is possible to notice that one shell - one tube pass HX configuration leads to lower TAC values compared to 2 shell passes - 2 tube passes one. Indeed, for the same overall heat transfer coefficient required (UA), in 2:2 TEMA F STHE, the shell-side velocity is two times more than that in an E shell. Consequently, shell-side pressure

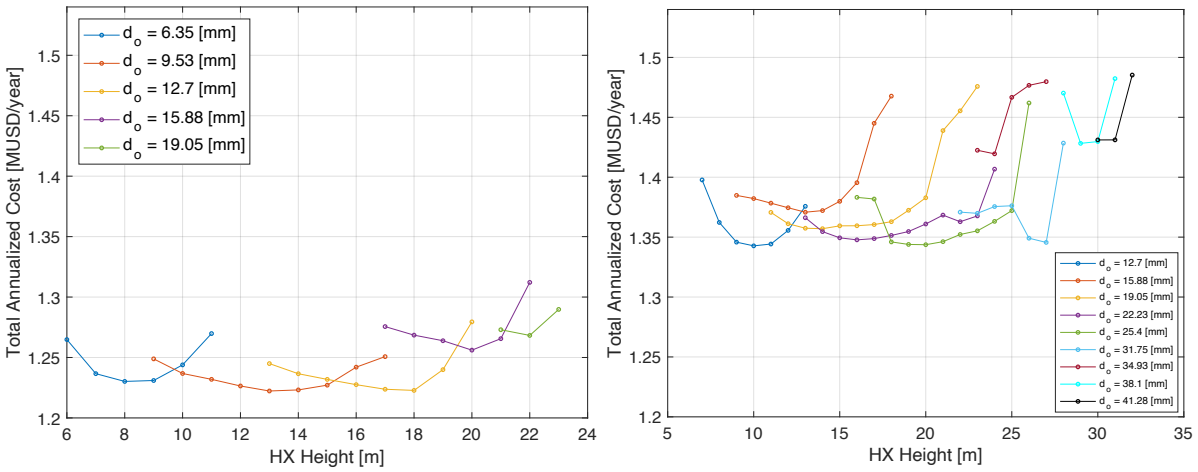

(a) 1:1 TEMA E STHE

(b) 2:2 TEMA F STHE

Figure 5.6.1: TAC function of tube outside diameter, pass length and number of passes

drop is eight times more than that in an E shell, implying higher pumping costs. On the other hand, higher shell-side velocity implies an increase in the heat transfer coefficient and a consequential reduction of the area, thus in investment cost. Since the reduction in investment cost is not as relevant as the increase in pumping cost, the 2:2 TEMA F STHE leads to higher TAC values. On top of that, according to [33], 2:2 TEMA F STHE configuration is rarely used because the shell-side longitudinal baffle will cause fluid leakage from the HP to LP side due to discontinuities in the welds between longitudinal baffle and shell. In addition, there will be a conduction heat transfer through the longitudinal baffle. These factors are not taken into account in the model, but in reality they will reduce the exchanger effectiveness.

Secondly, focusing on the TEMA E configuration, for a fixed tube outside diameter, there is always a HX length that represents the best compromise between investment cost and pumping cost, both shown in figure 5.6.2. Moreover, larger tube outside diameters lead to taller HX designs. This is due to the opposite effects of these variables on the tube-side velocity. Indeed, for the same heat transfer area, if on one hand longer tubes imply fewer number of tubes and consequently higher tube-side velocity, on the other hand larger tube outside diameters reduce the velocity. In this way, it is possible to keep sodium velocity between minimum and maximum values imposed. Based on the HX length adopted, the number of baffles will vary to fit the shell-side velocity constraints. Due to the maximum aspect ratio imposed, configurations with high HX length are excluded. Therefore, the maximum HX length is reached for minimum number of tubes, thus minimum shell diameter.

In the end, it is possible to notice that the minimum TAC is given by an HX length almost equal to 13 m and a tube outside diameter of 9.53 mm. This result is in agreement with [36], that assess that 9.53 mm and 19.05 mm are the most popular tube outside diameter sizes because they give the best performances and are the most economical in most applications. A detailed description of the HX design proposed is provided in table 5.6.1 and a graphical representation is available in figure 5.6.4.

Figures 5.6.2a and 5.6.2b, show respectively the investment cost and annual pumping cost as function of tube outside diameter and tube tube length for a single shell - single tube HX configuration.

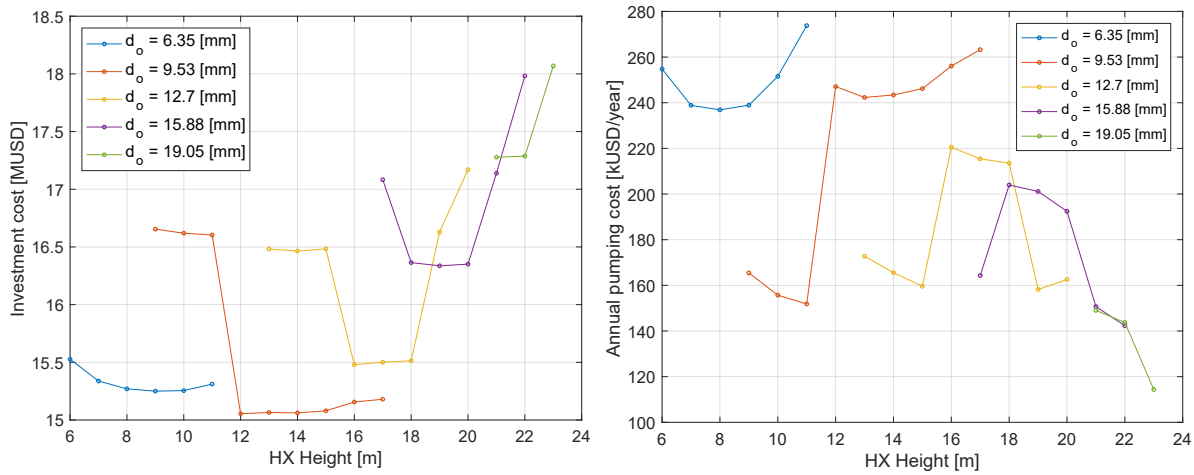

(a) HX investment cost

(b) Annual pumping cost

Figure 5.6.2: Investment cost and pumping cost function of tube outside diameter, pass length and number of passes

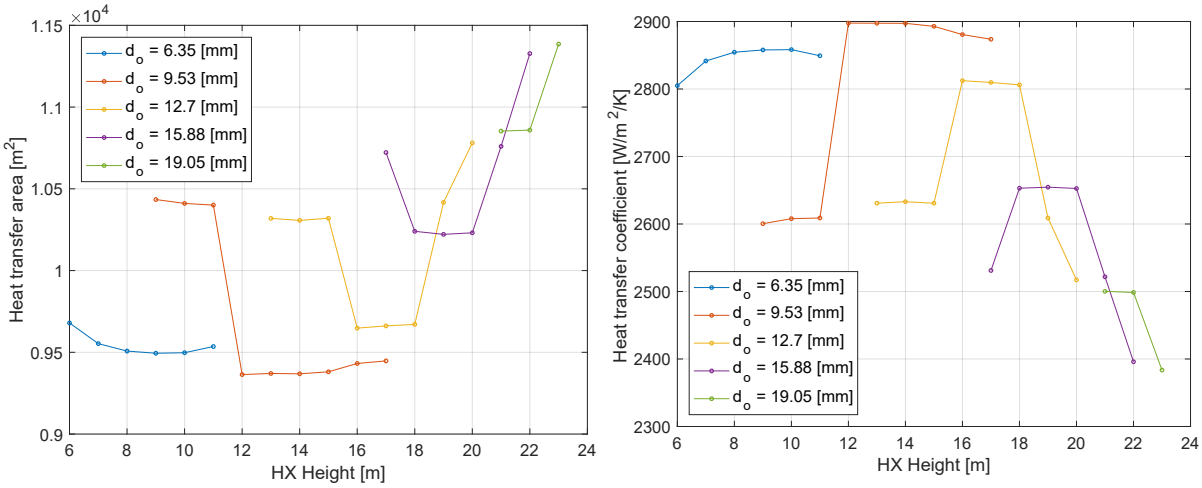

(a) Heat transfer area

(b) Heat transfer coefficient

Figure 5.6.3: Heat transfer area and heat transfer coefficient function of tube outside diameter, pass length and number of passes

As general trend, the investment cost increases with larger tube outside diameters and tube lengths, while the pumping cost presents the opposite behaviour. The investment cost and pumping cost tendency reflect respectively the heat transfer area and heat transfer coefficient behaviour, shown in figure 5.6.3.

In practice, for larger tube outside diameters and longer tubes, the tube thickness increases, resulting in a reduction of the heat transfer coefficient. Moreover, since the tube-side velocity decreases with larger tube diameters, the heat transfer coefficient decreases accordingly. Indeed, although shell-side velocity increases due to an increase in the number of baffles, combining all the effects, the heat transfer coefficient and annual pumping cost decrease. Consequently, for a fixed overall heat transfer coefficient required (UA), the heat transfer area needs to increase to compensate lower U value. In the end, the step changes in U and A, and consequently in C_{inv} and C_{pump}, are due to the unavoidable step change of the number of baffles, that impacts strongly on the shell-side velocity.

In Appendix C.4, number of tubes (figure C.4.2a), number of baffles (figure C.4.2b) and velocities (figure C.4.1a and C.4.1b) behaviours are reported as function of HX length and tube outside diameter.

Variable	Value	UM
Design Thermal Power	543	MW
Heat transfer area	9400	m^2
Design heat transfer coefficient	2900	$W/(m^2K)$
Material	Haynes230	–
Weight	87	$tons$
Overall Volume	35	m^3
Overall Length	15	m
Tube pass Length	13	m
Shell Diameter	1.83	m
Number of tubes	23500	–
Tube outside diameter	9.53	mm
Tube arrangement	Triangular	–
Number of baffles	3	–
Baffle tilt angle	15	deg
Design sodium velocity	1.9	m/s
Design chloride-salt velocity	1.2	m/s
Investment Cost	15	$MUSD$
Design annual pumping cost	240	$kUSD$

Table 5.6.1: Summary of most relevant HX variables

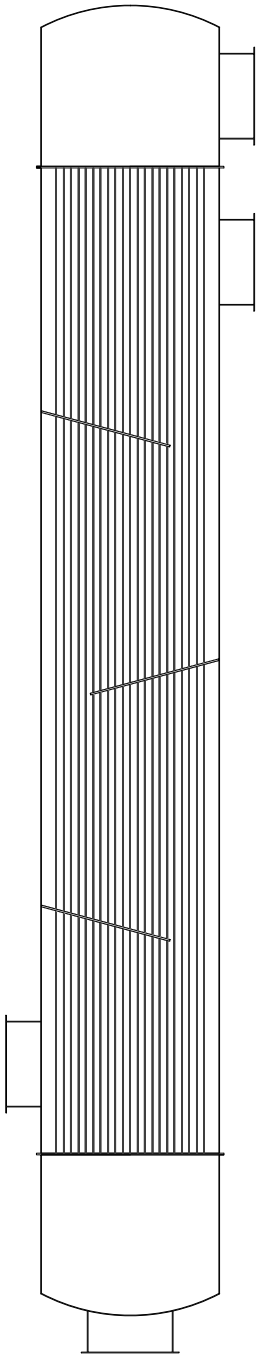

Figure 5.6.4: Graphical representation of the HX design

The provided shell and tube heat exchanger design is the result of a component level optimization, where although BCs, media, fluid dependent assumptions, and constraints are set according to the particular application, the objective function is the TAC and doesn't take into account the impact of the HX on the Na-Salt-sCO2 system model. Therefore, in chapter 6, a system-level optimization is performed and the impact of the HX on the global system is investigated.

Chapter 6

Sodium-Salt HX system-level optimization and sensitivity analysis

In this chapter, the impact of the heat exchanger on the performances and cost of the CSP system is analysed. Moreover, heat exchanger system-level optimizations and sensitivity analysis are presented.

6.1 Reference case

The system configuration selected as reference case is a 100 MWe CSP plant located in in Daggett, CA, defined following the guidance provided in the Gen 3 CSP Down-Selection Criteria [3]. The system model implemented in chapter 4 was set accordingly and the HX design proposed in chapter 5 was utilized.
The capacities of the principal system components and the most relevant parameters are summarized in the table 6.1.1.

Variable	Value	UM
Solar field size	976500	m^2
Receiver thermal design power	543	MW
Tower Height	150	m
HX thermal design power	543	MW
Storage hours	12	h
Solar Multiple (SM)	2.5	-
Power block net power	100	MWe

Table 6.1.1: Most relevant parameters of the CSP system reference case

By using the *NaSaltsCO2System* model, annual energy performances and costs were estimated. Three important key-parameters are provided in table 6.1.2. Moreover, in order to highlight the impact of the heat exchanger cost on the total system capital cost, the pie chart in figure 6.1.1 is presented.

Variable	Value	UM
Energy per year (EPY)	560	GWh
Levelized Cost of Electricity (LCOE)	72.66	USD/MWh
Capacity Factor (CF)	64	%

Table 6.1.2: Annual energy performances and cost parameters of the reference case

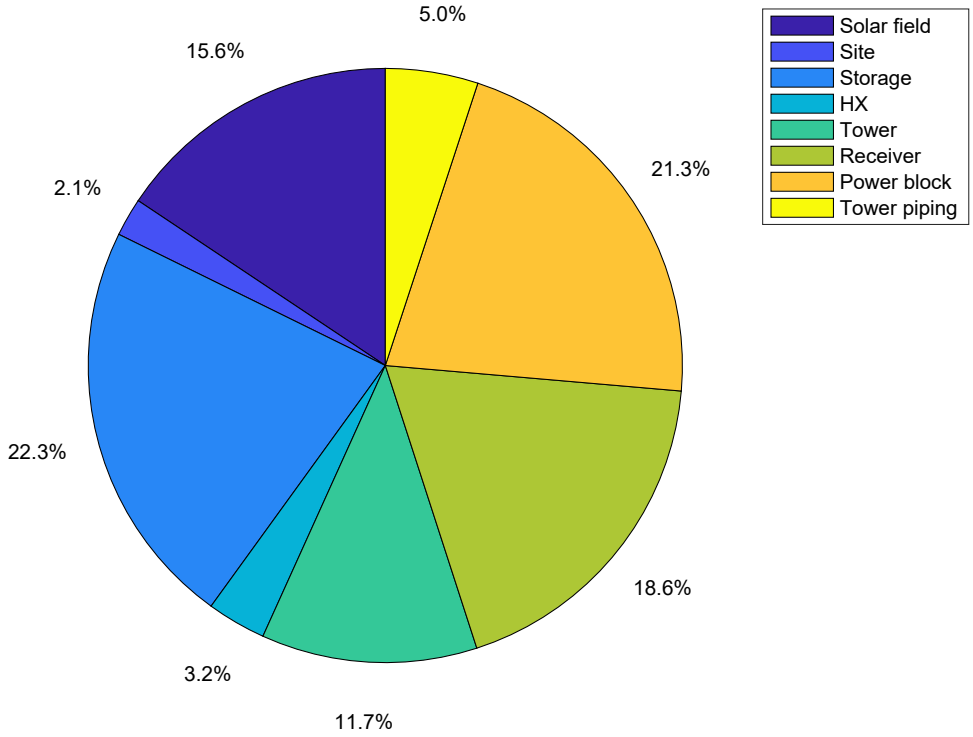

Figure 6.1.1: CSP system cost breakdown

It is possible to notice that the component that constitutes the largest share of the pie-chart is the thermal energy storage (22.3%). On the other side, the smallest share of the cost is represented by the site preparation costs that amount to 2.1% of the total. For what concerns the heat exchanger, it is the components that costs the least and it represents the 3.2% of the total cost. Consequently, limited reduction of the LCOE can be achieved acting only on the HX, while more relevant improvements can be obtained by acting on the combined receiver-heat exchanger block that together represents about the 22% of the total cost.

6.2 Heat exchanger system-level optimizations

In this section, the main assumptions and results of the heat exchanger system-level investigations are presented.

6.2.1 HX internal configuration optimization

This investigation aimed to individuate the HX geometrical configuration that minimizes the LCOE of the CSP plant. As mentioned in section 6.1, the selected HX is characterized by the geometrical configuration that minimizes the TAC. For this analysis, the heat exchanger internal optimization was disabled in the model and the design variables, such as number of tubes, tube outside diameters, tube layout, number of shell passes, and number of tube passes,were provided as inputs.

Figure 6.2.1a shows the LCOE as function of the tube pass lengths and of the tube outside diameters. In particular, The triangular pitch and the single shell pass/single tube pass were adopted since they led always to lower LCOE values compared to square pitch and to the two shell passes/two tube passes configuration. On the other side, figure 6.2.1b shows TAC as function of the same design variables adopted in figure 6.2.1a.

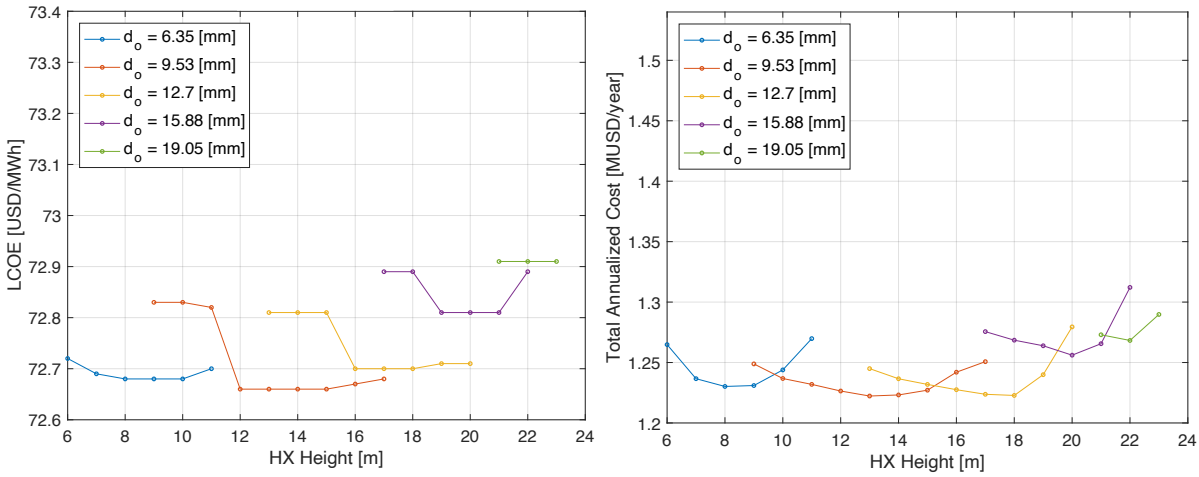

(a) Levelized Cost of Electricity (LCOE) (b) Total Annualized Cost (TAC)

Figure 6.2.1: Levelized Cost of Electricity and Total Annualized Cost function of tube outside diameter and tube pass length

Figure 6.2.1 shows a comparison between the LCOE and the TAC function. The interesting results that can be highlighted is that the HX configuration that minimizes the TAC coincides with the HX configuration that minimizes the LCOE. Therefore,

the HX design included in the reference case represents already the configuration that minimizes the plant LCOE.
Generally, it is possible to assess that the design that minimizes the TAC represents a good guess of the one that minimizes the LCOE and in line with this result, from this point onward, the HX configuration will be defined by means of the model internal optimization.

6.2.2 HX LMTD optimization

This investigation aimed to highlight the potential reduction of the LCOE of the CSP plant that can be achieved by acting on the HX LMTD. The analysis was carried out on the combined receiver-heat exchanger block by varying the sodium-side temperatures of the LMTD. For what concerns the salt-side, the nominal temperatures of 500-720°C were preserved. The reference case was slightly modified, optimizing the receiver capacity. The most relevant parameters of the reference case are summarized in table 6.2.1.

Component	Variable	Value	UM
Heat Exchanger and Receiver	Design Thermal Power	535	MW
	Cold sodium temperature	520	$°C$
	Hot sodium temperature	740	$°C$
Heat Exchanger	LMTD	20	$°C$
	Heat transfer area	9172	m^2
	Tube pass Length	13	m
	Shell Diameter	1.83	m
	Number of tubes	23506	$-$
	Tube outside diameter	9.53	mm
	Number of baffles	3	$-$
	Investment cost	15	$MUSD$
Receiver	Diameter	14.7	m
	Height	22.0	m
	Design thermal efficiency	88.5	%
	Investment cost	77	$MUSD$
System	Levelized Cost of Electricity	70.00	USD/MWh
	Electricity produced per year	571.3	GWh
	Capacity Factor	65.2	%

Table 6.2.1: Definition of the reference case of the LMTD optimization

In this study, the impact of the sodium temperatures on the CSP system performances was analysed assuming two approaches: fixed inlet-outlet temperature change(figure

6.2.2a) and variable inlet-outlet temperature change (figure 6.2.2b). In detail, the fixed inlet-outlet temperature change was chosen equal to 220°C (reference case), whereas in the case of the variable one, the maximum sodium temperature was fixed equal to 740°C .

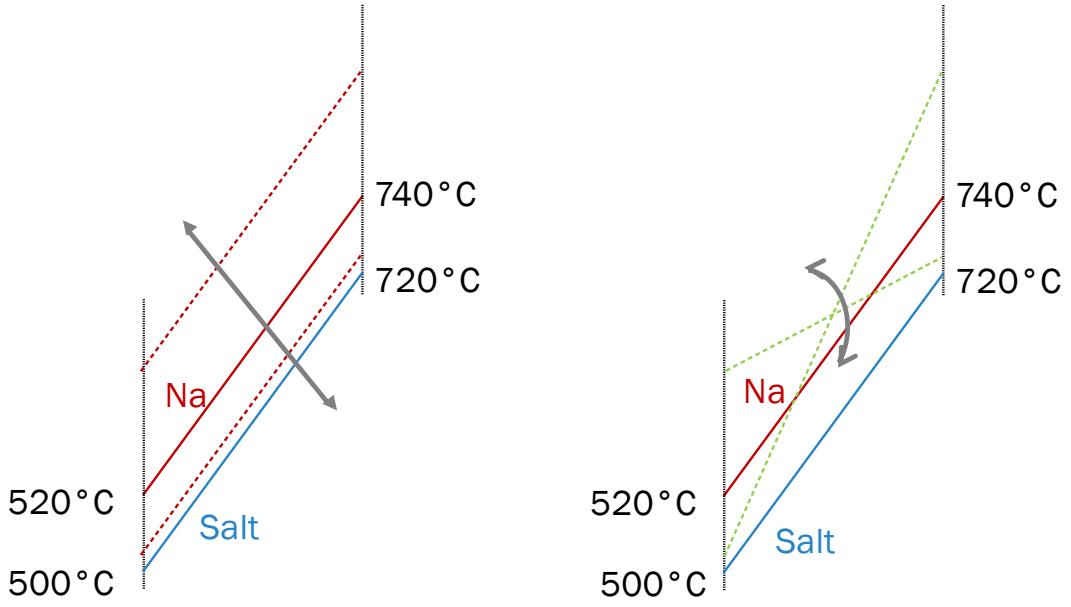

(a) Fixed inlet-outlet temperature change (b) Variable inlet-outlet temperature change

Figure 6.2.2: Approaches adopted for the LMTD optimization

The variation of the sodium temperatures affects both the heat exchanger and the receiver design. As for the heat exchanger, in comparison to the reference case, keeping the same thermal design power, a larger LMTD implies a more compact heat exchanger design. On the other side, for what concerns the receiver, assuming a fixed solar field size, the maximum allowable flux that the receiver material can withstand is function of the receiver area and operating temperatures. Hence, by increasing the sodium temperatures, the receiver dimensions need to increased as well in order to preserve the maximum allowable flux. Moreover, larger receivers lead also to higher thermal losses and consequently lower thermal efficiencies.

For each combination of inlet-outlet sodium temperatures analysed in this study, the new HX design was defined by means of the internal optimization implemented in the HX model, whereas in the case of the receiver, the new design was manually updated as a result of complimentary investigations performed in the ANU Solar Thermal Group. In appendix D.3, figure D.3.1 provides the heat flux on the receiver surface and the maximum allowable value as function of the flow path length and of the flow path type for the reference case.

Fixed inlet-outlet temperature change approach

The sodium inlet-outlet temperature was fixed equal to 220°C in line with the reference case. The minimum heat exchanger pinch point temperature difference was assumed equal to 2°C, admitting 502°C as minimum sodium temperature. Figure 6.2.3a shows the plant LCOE as function of the receiver outlet temperature. The receiver and the heat exchanger investment costs are presented in figure 6.2.3b.

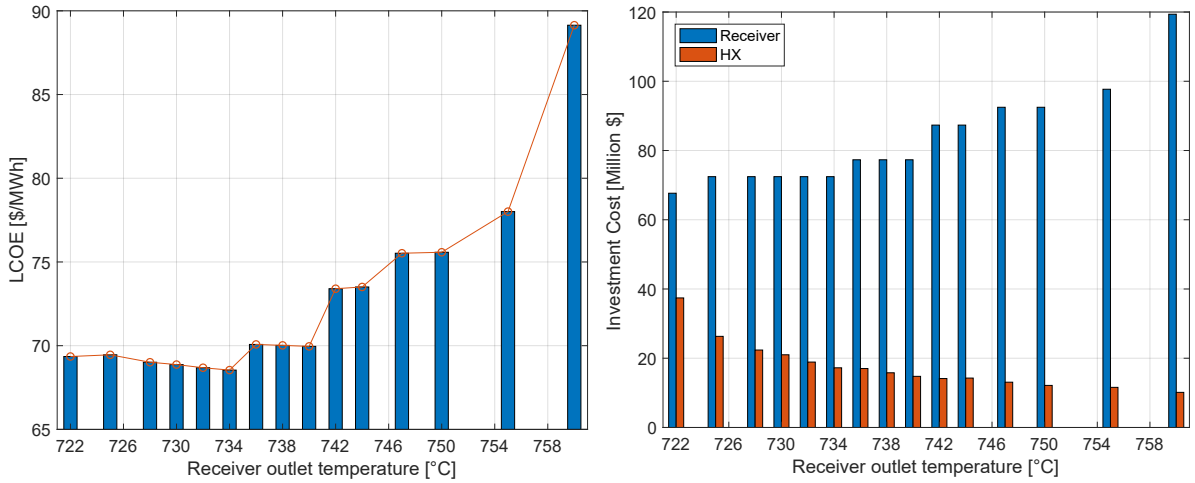

(a) Levelized Cost of Electricity

(b) Receiver and HX investment cost

Figure 6.2.3: LCOE and investment costs as function of the receiver outlet temperature (fixed inlet-outlet temperature approach)

The minimum LCOE value resulted equal to 68.54 USD/MWh and it was obtained adopting an inlet-outlet sodium temperatures equal to 514-734°C. Thus, by reducing the LMTD from 20°C (reference case) to 14°C, the receiver investment cost decreased whereas the heat exchanger one increased. Since the receiver cost, compared to the heat exchanger one,constituted a larger share of the total capital cost, this results respected the expectations. Respect to the reference case, a cheaper receiver and a more expensive heat exchanger minimized the plant LCOE.
The variations of the heat exchanger area and of the receiver dimensions are shown respectively in figure 6.2.4a and figure 6.2.4b.

In particular, as for the receiver, figure 6.2.4b shows that, varying the receiver outlet temperature from 722 to 760°C, both the diameter and the height of the receiver increased proportionally. On the other side, for what concerns the heat exchanger, compared to the reference case, reducing the LMTD the overall heat transfer coefficient (UA) decreased in order to fit the design thermal power. More details on the variation of the HX design are presented in figure 6.2.5.

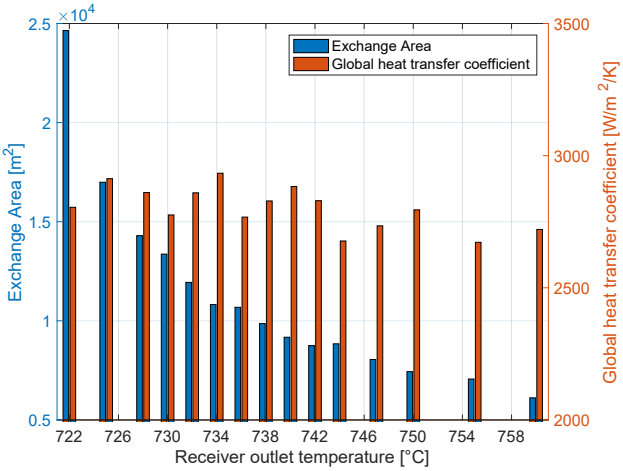

(a) Exchange area and heat transfer coefficient

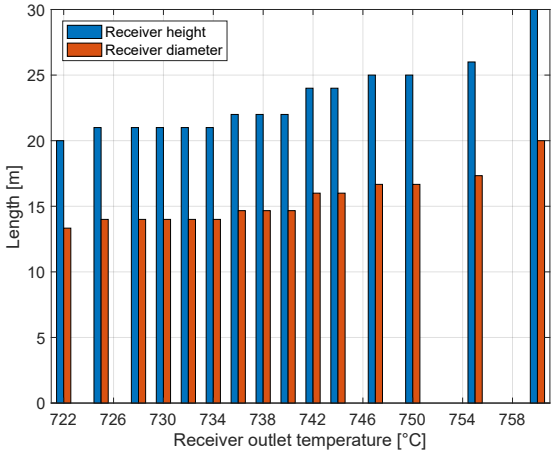

(b) Height and diameter of the receiver

Figure 6.2.4: Heat transfer area, heat transfer coefficient, and receiver size as function of the receiver outlet temperature (variable inlet-outlet temperature approach)

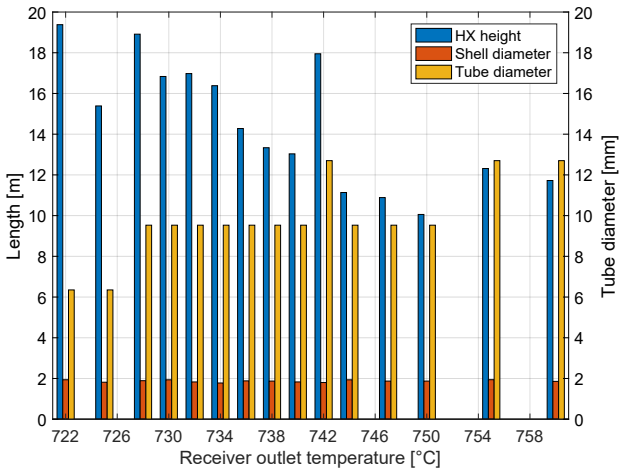

(a) HX configuration

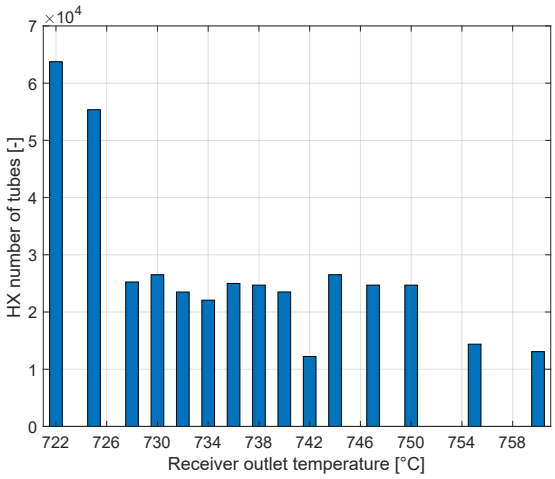

(b) Number of tubes

Figure 6.2.5: HX configuration variation

Figure 6.2.4a shows that the increase of the LMTD was compensated by a reduction of the heat exchanger heat transfer area. In addition, the reduction in area was obtained by means of a reduction of the number of tubes (6.2.5b) or for similar number of tubes values, the area was reduced by acting on the tube pass length. The tube outside diameter varied, in order to fit the velocity constraints and in order to minimize the TAC of the HX.

Sodium and chloride salt velocities variations are presented in figure D.2.1, in appendix D.2. In addition, also the shell-side and tube side pressure losses are presented in the same figure.

In the end, table 6.2.2 summarizes the principal parameters that characterize the

optimum configuration of the receiver-heat exchanger block.

Component	Variable	Value	UM
Heat Exchanger and Receiver	Design Thermal Power	529	MW
	Cold sodium temperature	514	$°C$
	Hot sodium temperature	734	$°C$
Heat Exchanger	LMTD	14	$°C$
	Heat transfer area	10824	m^2
	Tube pass Length	16	m
	Shell Diameter	1.78	m
	Number of tubes	22070	$-$
	Tube outside diameter	9.53	mm
	Number of baffles	4	$-$
	Investment cost	17	$MUSD$
Receiver	Diameter	14.0	m
	Height	21.0	m
	Design Receiver Efficiency	89.3	%
	Investment cost	72	$MUSD$
System	Levelized Cost of Electricity	68.54	USD/MWh
	Electricity produced per year	581.0	GWh
	Capacity Factor	66.3	%

Table 6.2.2: Principal parameters that characterize the optimum configuration of the receiver-heat exchanger block (fixed inlet-outlet temperature approach)

Variable inlet-outlet temperature change approach

In this investigation, the maximum sodium temperature was fixed equal to the design value (740°C), whereas the receiver inlet sodium temperature was varied between 502 and 540°C. Figure 6.2.6a shows the plant LCOE as function of the receiver inlet temperature. The receiver and the heat exchanger investment costs are presented in figure 6.2.6b.

The latter shows that keeping constant the maximum sodium temperature, no variations in the receiver cost were found as function of the receiver inlet temperature. Hence, the receiver design was preserved and increasing the LMTD, the HX cost and consequently of the LCOE decreased.

The minimum LCOE resulted 69.68 USD/MWh and was obtained for the maximum receiver inlet temperature considered.

Future works need to be conducted to deeply explore the impact on the HX and receiver design for higher inlet temperatures.

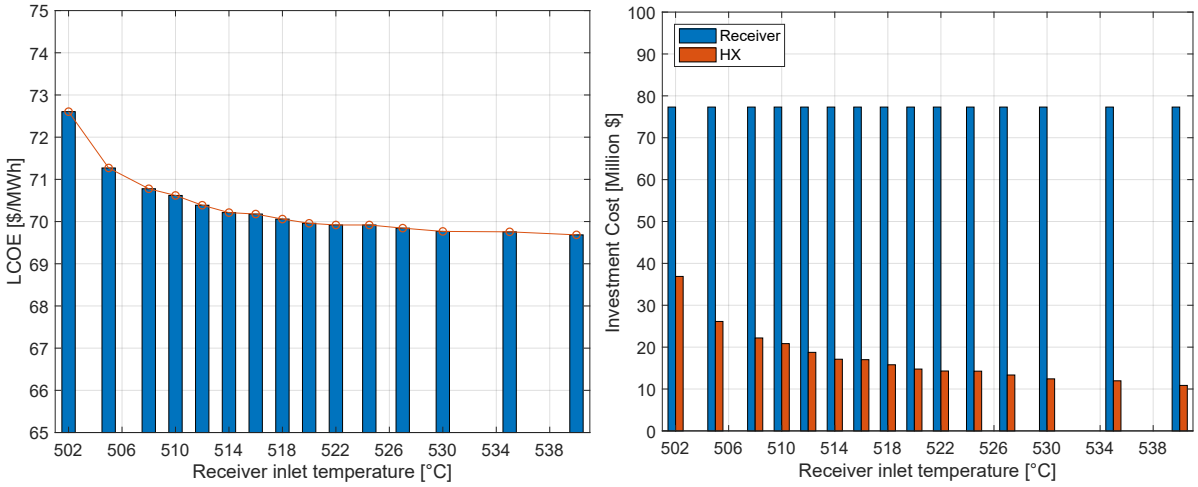

(a) Levelized Cost of Electricity (b) Receiver and HX investment cost

Figure 6.2.6: LCOE and investment costs as function of the receiver inlet temperature (variable inlet-outlet temperature approach)

Similarly to the fixed inlet-outlet temperature change approach, the increase in LMTD was compensated by a reduction of the UA value. In detail, figure 6.2.7a shows that the heat transfer coefficient was more or less preserved, whereas the heat transfer area decreased. Comparing figure 6.2.7b and figure 6.2.5b, a similar trend can be identified. Consequently, a similar trend was found also for the tube pass length, the HX height, and the tube outside diameter as function of the receiver inlet temperature.
This behaviour is represented in figure D.2.2a, in appendix D.2, along with the fluid velocities and pressure losses as function of the inlet receiver temperature (figure D.2.2b).

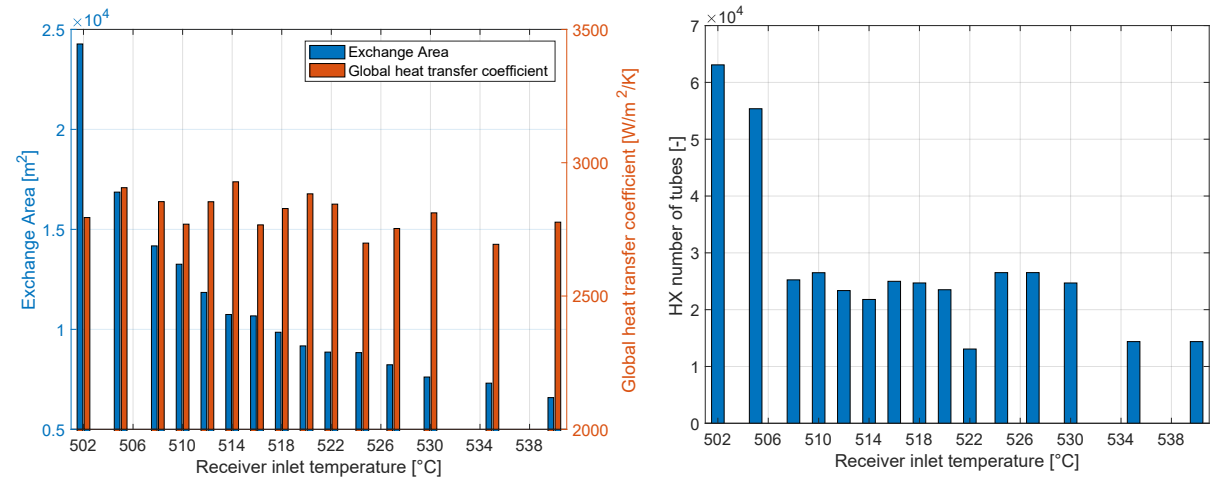

(a) Exchange area and heat transfer coefficient (b) Number of tubes

Figure 6.2.7: Heat transfer area, heat transfer coefficient, and number of tubes as function of the receiver inlet temperature (variable inlet-outlet temperature approach)

In the end, table 6.2.3 summarizes the most relevant parameters that characterize the optimum configuration of the receiver-heat exchanger block for the variable inlet-outlet temperature change approach.

Component	Variable	Value	UM
Heat Exchanger and Receiver	Design Thermal Power	532	MW
	Cold sodium temperature	540	$°C$
	Hot sodium temperature	740	$°C$
Heat Exchanger	LMTD	–	$°C$
	Heat transfer area	6587	m^2
	Tube pass Length	11	m
	Shell Diameter	1.94	m
	Number of tubes	14379	$-$
	Tube outside diameter	12.70	mm
	Number of baffles	3	$-$
	Investment cost	11	$MUSD$
Receiver	Diameter	14.7	m
	Height	22.0	m
	Design Receiver Efficiency	88.2	%
	Investment cost	77	$MUSD$
System	Levelized Cost of Electricity	69.68	USD/MWh
	Electricity produced per year	569.4	GWh
	Capacity Factor	65.0	%

Table 6.2.3: Most relevant parameters of the CSP system reference case

In conclusion, the two investigations conducted on the HX LMTD pointed out the potential LCOE reductions that can be achieved acting on the receiver-heat exchanger block. However, the problem was not fully analysed and future works are necessary in order to propose an optimized HX design.

6.2.3 Investigation on the downsizing of the HX

This analysis aimed to investigate the potential LCOE reduction that can be achieved by downsizing the HX compared to the nominal receiver capacity. The idea that motivated this analysis is that employing a smaller HX, the annual electricity production will not be strongly influenced, whereas a reduction of the HX cost and then of the plant LCOE can be obtained.

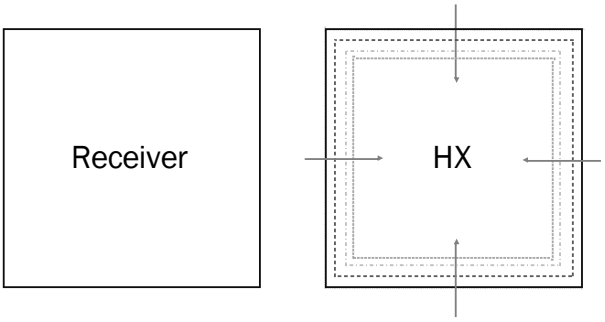

Figure 6.2.8: Heat exchanger downsizing investigation

Moreover, in order to maximizes the HX performances, a thermal power larger then the nominal power, was accepted during the HX operating conditions. If the thermal power exceeds the maximum acceptable thermal power, the thermal power production can be curtailed by defocusing the heat flux. For the purpose of presenting the main results obtained, two key parameters were defined: the *Downsizing factor* (DSF) and the *Maximum acceptable thermal power factor* ($MATPF$) and they are presented respectively in equation (6.1) and equation (6.2).

$$DSF = \frac{Q_{HX,design}}{Q_{receiver,design}} \tag{6.1}$$

$$MATPF = \frac{Q_{max,HX}}{Q_{HX,design}} \tag{6.2}$$

When the maximum thermal power exceeds the design value, the operating mass flow rates and consequently the fluid velocities could exceed the design values. In this study, the maximum acceptable thermal power was limited in order to guarantee that the operating fluid velocities, on both shell and tube sides, never exceeded the maximum acceptable velocities. Moreover, the maximum fluid temperatures should never exceed the maximum design values and, in particular, the sodium-side operating temperatures shouldn't significantly differ from the receiver design values in order to

preserve the receiver performances.

Figure 6.2.9a and figure 6.2.9b show the HX operating thermal power for a typical summer week as function of the downsizing factor. In particular, in figure 6.2.9a, the maximum acceptable thermal power was assumed equal tot the design value, whereas in figure 6.2.9b, the maximum power was increased by 25%.

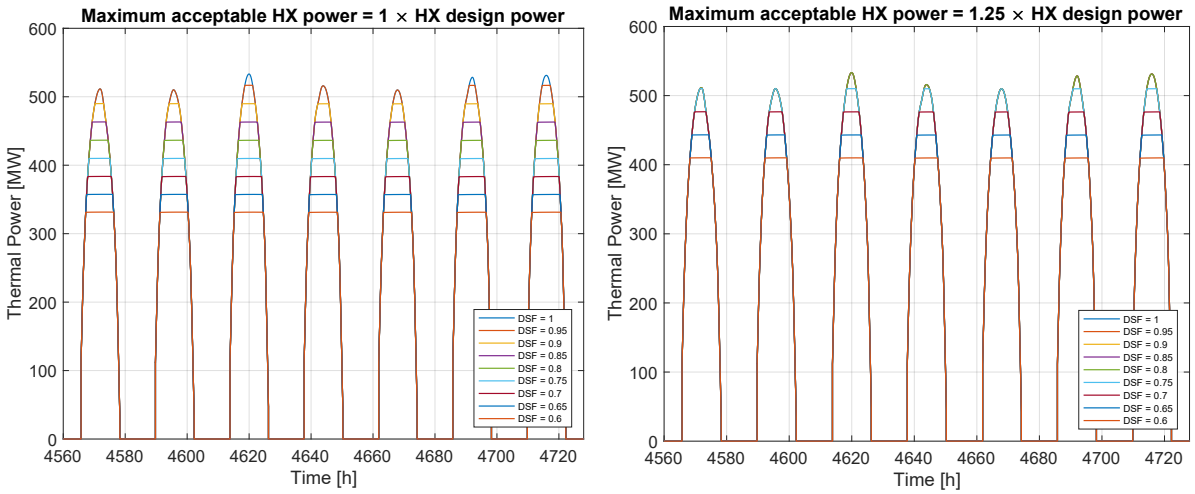

(a) MATPF equal to 1

(b) MATPF equal to 1.25

Figure 6.2.9: Heat exchanger thermal power during typical summer week

From figure 6.2.9, it can be noticed that in the case of MATPF equal to 1.25, the curtailment of the thermal power was necessary only for DSF smaller than 0.8. On the other hand, in the case of MATPF equal to 1, the defocus of the solar radiation was always necessary for DSF smaller then 1.

The LCOE and the electricity produced per year as function of the maximum acceptable thermal power factor and of the downsizing factor are provided respectively in figure 6.2.10a and figure 6.2.10b. It can be noticed that, as expected, the electricity per year always decreased for MATPF values ranging from 1 to 1.25, for any downsizing factor, while, for what concerns the MATPF equal to 1.3 and DSF equal to 0.7 the electricity produced per year resulted higher than the reference case. This results was found because, for that point, the operating velocities exceeded the maximum acceptable velocities. For this reason the curve for MATPF equal to 1.3 was excluded from the analysis. Hence, the optimum point was considered to be the configuration characterized by a MATPF equal to 1.25 and a DSF equal to 0.8, that led to a LCOE value of 72.38 USD/MWh.

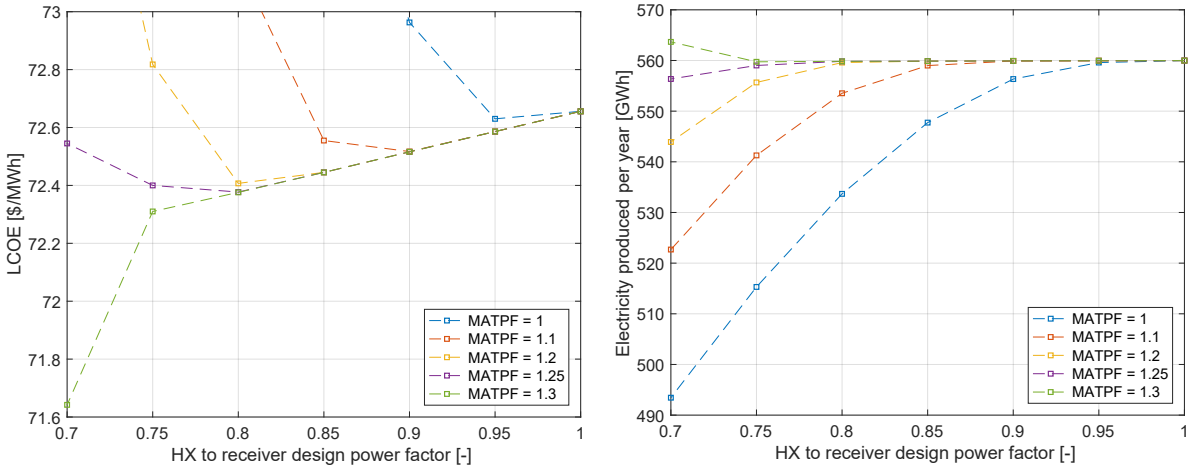

(a) Levelized Cost of Electricity (b) Electricity produced per year

Figure 6.2.10: Levelized cost of electricity and electricity produced per year as function of the DSF

Figure 6.2.11a shows how the HX area and heat transfer coefficient changed by varying the downsizing factor. Instead, figure 6.2.11b shows pressure losses and fluid velocities as function of the downsizing factor. Decreasing the HX capacity, the heat transfer

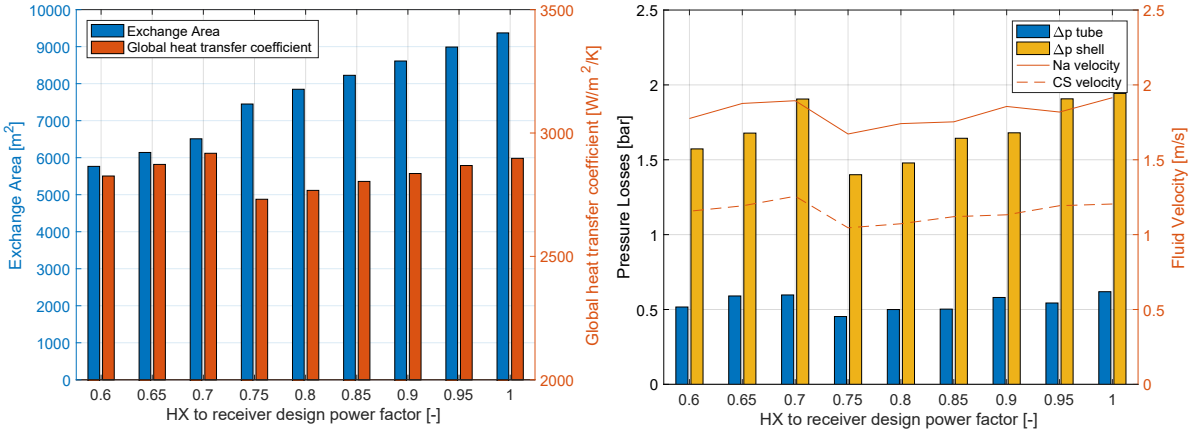

(a) Exchange area and heat transfer coefficient (b) Pressure losses and fluid velocities

Figure 6.2.11: Pressure losses, fluid velocities, exchange area, and heat transfer coefficient as function of the DSF

area decreased proportionally, whereas the heat transfer coefficient was preserved according to the velocities that were subject to limited variations. The factor that limited the MATPF to a maximum of 1.25 was the shell-side velocity that for any DSF values was not too far from the maximum acceptable velocity (1.5 m/s).

The heat exchanger configuration, in terms of tube outside diameter, shell diameter, tube pass length, and number of tubes as function of the DSF is presented in appendix D.1, figure D.1.1.

6.3 Sensitivity analysis on the HX investment cost

This sensitivity analysis aimed to show how the HX cost value impacts on the total plant cost and on the plat LCOE. Thus, assuming the same plant configuration presented in section 6.1, the HX cost was modified by varying the heat exchanger mass specific material cost (c_{H230}) from half to three times of the reference cost value (84 USD/kg). For each value of c_{H230}, a different heat exchanger design was proposed by means of the internal optimization implemented in the HX model.
Figure 6.3.1 presents the system LCOE and the acHX investment cost as function of the material specific cost normalized respect to the reference value.

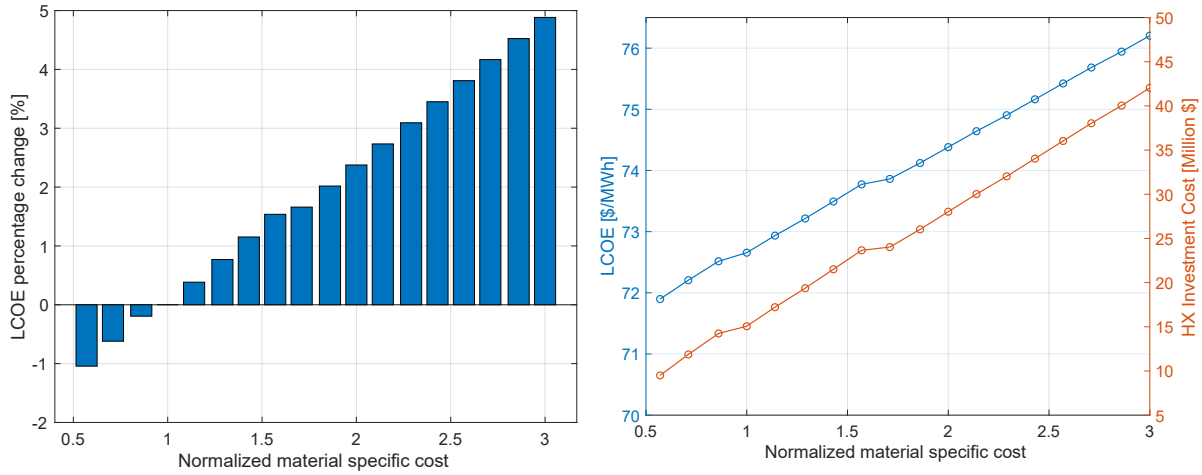

(a) LCOE percentage change

(b) LCOE and HX investment cost

Figure 6.3.1: LCOE percentage change, LCOE values, and HX investment cost as function of the normalized material mass specific cost

By varying the normalized material mass specific cost from 0.5 to 3, the share of the HX cost on the total plant investment cost ranged from 2% to 9%. Instead, the LCOE varied from 71.90 to 76.20 USD/MWh.

Figure 6.3.2a shows the exchange area and heat transfer coefficient of the heat exchanger as function of the normalized mass specific cost. For high material costs, the internal optimization of the HX model led to designs characterized by small exchange area and large heat transfer coefficient. On the other side, figure 6.3.2b shows the pressure losses and fluid velocities as function of the normalized mass specific cost. For high material costs the fluid velocities increased and consequently also the pressure losses. Therefore, it can be noticed that increasing the material cost the TAC, that generally represents a good compromise between HX investment cost and pressure

losses, moved towards the minimum investment cost.

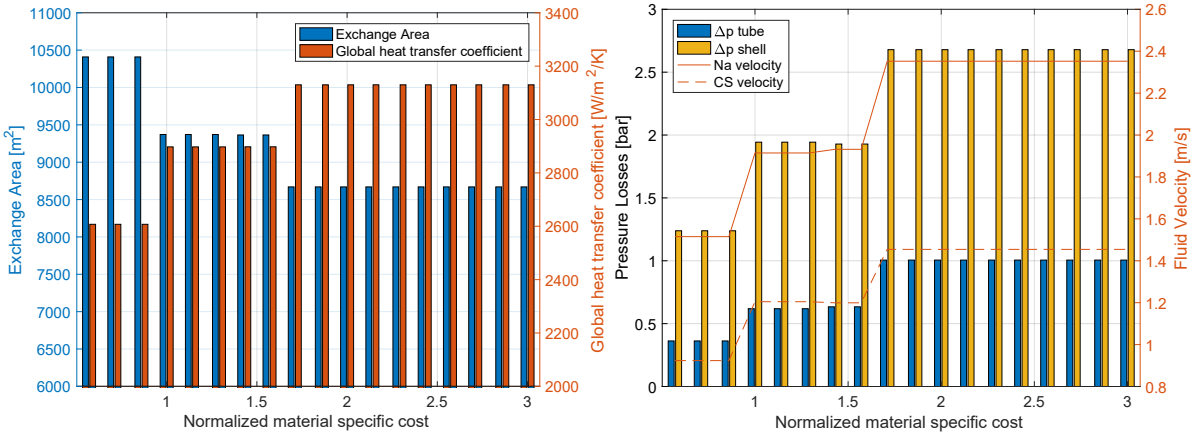

(a) Exchange area and heat transfer coefficient (b) Pressure losses and fluid velocities

Figure 6.3.2: Exchange area, heat transfer coefficient, pressure losses, and fluid velocities as function of the normalized material mass specific cost

In the end, figure 6.3.3, shows the heat exchanger configuration, in terms of tube outside diameter, shell diameter, tube pass length, and number of tubes as function of the normalized material specific cost.

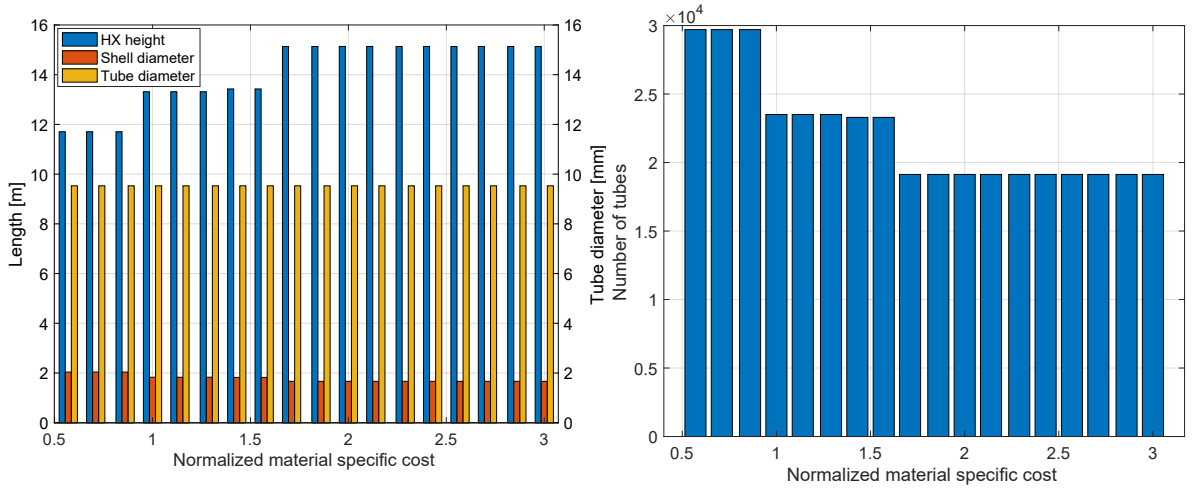

(a) HX configuration (b) Number of tubes

Figure 6.3.3: Tube outside diameter, shell diameter, tube pass length, and number of tubes as function of the normalized material mass specific cost

It is possible to notice that the reduction in area was driven by a reduction in the number of tubes, while the tube pass length increased and the tube outside diameter was kept constant.

Chapter 7

Discussion of the results

7.1 Considerations on the HX model

In this research work, the developed shell and tube heat exchanger model was customized in order to design the most suitable sodium-salt heat exchanger. Moreover, the present model allowed to simulate the performances of the designed heat exchanger, for variable operating conditions. The HX model provided a detailed design, defining the heat transfer area, the nominal heat transfer coefficient, the nominal pressure losses, the investment cost, the expected annual pumping cost, the overall dimensions and the weight. In this study, the TAC was adopted as objective function for the HX model. The performed HX system-level optimizations showed that the HX configuration that minimized the TAC resulted to be a good guess of the HX design that minimized the LCOE of the sodium-salt-sCO2 CSP system. Therefore, the TAC approach turned out to be advantageous and allowed to save computational time. The selected HX design resulted to be a single-shell/single tube pass configuration, with vertical alignment, characterized by an overall height of 15 m, and a shell diameter of 1.8 m. The very high aspect-ratio and the proposed tube diameter (9.53 mm) respected the literature recommendations [33]. In addition, several techno-economic investigations, for different heat exchanger capacities, temperatures and costs pointed out the model robustness, stability, and flexibility.

7.2 Considerations on the *NaSaltsCO2System* model

The developed *NaSaltsCO2System* model allowed to estimate the energy performances of the CSP plant, as well as the LCOE. The model resulted robust and able to perform annual simulations for different plant sizes, Solar Multiple (SM) values, TES hours and operating conditions. Considering the sodium-salt-sCO2 CSP system characterized by a receiver capacity of 543 MWth, 12 hours of TES, and a 100 MWe power block, the LCOE resulted equal to 72.66 USD/MWh. The model represented a fundamental tool utilized during the investigation about the value of liquid sodium for CSP application and lays the groundwork to explore potential improvements of this new generation of CSP systems in future works.

7.3 Considerations on the HX optimizations and sensitivity analysis

The most interesting system-level optimization was carried out on the combined receiver-heat exchanger block. Acting only on the sodium-side temperatures, the LMTD of the HX was varied and consequently the design of both heat exchanger and receiver was modified. The techno-economic analysis didn't aim to find the exact optimum receiver-heat exchanger configuration, but to investigate the potential LCOE reduction. The present analysis showed that, keeping a fixed inlet-outlet temperature difference, the reduction of the maximum sodium temperature from 740°C to 734°C decreased the LCOE value down to 68.54 USD/MWh. This gain was achieved by a reduction of the receiver size and an increase of the HX area. On the other hand, fixing the output sodium receiver temperature (740°C) and varying the inlet one from 520°C up to 540°C, it was shown that the receiver configuration was preserved while the HX area decreased and consequently its cost. The resulted LCOE was equal to 69.68 USD/MWh. The determination of the local minimum LCOE values didn't complete the optimization, but highlighted that the HX LMTD offers room for further improvements and LCOE reductions. For what concerns the HX downsizing analysis, it proved to be of secondary importance. Indeed, downsizing the HX by 20% and increasing the maximum thermal power by 25% of the nominal value, just a marginal LCOE reduction, from 72.66 to 72.38 USD/MWh, was achieved.
In the end, the sensitivity analysis pointed out that doubling the heat exchanger cost, the plant LCOE passed from 72.66 to 74.38 USD/MWh.

Chapter 8

Conclusion and future work

The chapter concludes and answers the purpose of research. Limitations of the study and future work also will be outlined for further possible research and development.

8.1 Conclusions

In this research work, a sodium-chloride salt heat exchanger for the sodium-salt-sCO2 CSP system was designed. A completely new Modelica-based *HX* model, implementing TEMA guidelines, was developed and added to the *SolarTherm* library. Furthermore, as an extension of earlier models, the *NaSaltsCO2System* model was implemented in *SolarTherm*, by incorporating the *HX* model and linking it with other new and existing component models.

In this work, the sodium-salt-sCO2 CSP system considered as the reference case is located in Daggett, CA and it is characterized by a receiver and a HX capacity of 543 MWth, 12 hours of TES, and a 100 MWe power block. The sodium-salt heat exchanger was designed aiming at minimizing the LCOE of the plant. The most cost-effective design selected for the sodium-salt HX is a shell and tube HX disposed vertically and characterized by single shell pass, single tube pass configuration with a very high height-to-diameter aspect ratio. The LCOE of the plant resulted equal to 72.66 USD/MWh and, in reference to the total capital cost, the share of the HX cost resulted equal to 3.2%. The system-level optimization carried out on the combined receiver-heat exchanger block highlighted the possibility to reduce the LCOE down to

68.54 USD/MWh, by acting on the HX LMTD. This relevant result points out that there is still room for further improvements and consequential LCOE reductions.
In reality, another significant achievement is the implemented *HX* model which was developed as a general model for shell and tube heat exchangers, with the possibility of being customized in terms of media adopted, constraints, boundary conditions, and correlations. During several investigations carried out in this work, the model proved its flexibility, robustness, and versatility, providing a complete geometry description, and an estimation of the performances and costs for different boundary conditions and techno-economic assumptions.

Another important outcome of this study is the developed *NaSaltsCO2System* model, that, up to date, is the unique model able to simulate the energy performances, the capital cost and the LCOE of the sodium-salt-sCO2 CSP plant. By means of this model, it was possible to highlight the potential reduction of the LCOE plant down to 68.5 USD/MWh. From a modelling perspective, the *NaSaltsCO2System* resulted a robust and stable model capable to estimate the plant performances for any solar field sizes, receiver and HX dimensions, storage hours and power block capacities.

The *NaSaltsCO2System* and the *HX* models constitute two important tools that can pave the way to future research studies and lay the groundwork to explore potential improvements of this new generation of CSP systems, which can play a fundamental role in the future global energy mix.

8.2 Limitations and future works

Although the models developed for shell and tube HX and for the CSP system turned out to be useful and important tools, there is still room for possible improvements. Some of the limitations and planned future works are presented below.

- The HX model was implemented only for shell and tube heat exchangers, based on standard procedures and correlations available in literature. As future work, other configurations should be investigated and modelled, and a comparison should be proposed;
- The HX model was developed as quasi-static model, neglecting the switch on/off dynamic considered of secondary importance respect to the simulation of the main operating conditions. Moreover, since the fluid properties do not vary

more than 5% in the temperature range proposed, a lumped-parameter model was implemented. These assumptions limited the investigation, precluding the possibility of studying relevant aspects such as the thermal stresses along the heat exchanger that could strongly impact on the design. A possible investigation of these aspects could be performed in a one-dimensional model and further constraints can be included in the current HX model.

- The HX system-level optimization regarding the LMTD variation was conducted keeping unchanged the storage set-point temperatures. In future works, it would be interesting to investigate the impact of the LMTD variation on the global CSP system to foster additional LCOE reductions.
- In the end, a verification and/or validation of the HX model was not carried out in this study and should be performed in future works.

Bibliography

[1] Fritsch, A., Frantz, C., and Uhlig, R. “Techno-economic analysis of solar thermal power plants using liquid sodium as heat transfer fluid”. In: *Solar Energy* 177.November 2018 (2019), pp. 155–162. ISSN: 0038092X. DOI: 10.1016/j.solener.2018.10.005. URL: https://doi.org/10.1016/j.solener.2018.10.005.

[2] Mehos, M., Turchi, C., Vidal, J., Wagner, M., Ma, Z., Ho, C., Kolb, W., Andraka, C., and Kruizenga, A. *Concentrating Solar Power Gen3 Demonstration Roadmap*. National Renewable Energy Laboratory (NREL): Golden, CO, USA, 2017.

[3] United States Department of Energy. “Gen 3 CSP Topic 1 - Phase 3 Test Facility Down-Selection Criteria”. In: *Archives* April (2019), pp. 5–8.

[4] Ho, C.K. and Iverson, B.D. *Review of high-temperature central receiver designs for concentrating solar power*. Renew. Sustain. Energy Rev. 29, 2014.

[5] Fritsch, A., Flesch, J., Geza, V., Singer, Cs, Uhlig, R., and Hoffschmidt, B. “Conceptual Study of Central Receiver Systems with Liquid Metals as Efficient Heat Transfer Fluids”. In: *Energy Procedia* 69.0 (2015), pp. 644–653. ISSN: 18766102. DOI: 10.1016/j.egypro.2015.03.074. URL: http://dx.doi.org/10.1016/j.egypro.2015.03.074.

[6] Coventry, J., Andraka, C., Pye, J., Blanco, M., and Fisher, J. “A review of sodium receiver technologies for central receiver solar power plants”. In: *Solar Energy* 122 (2015), pp. 749–762. ISSN: 0038092X. DOI: 10.1016/j.solener.2015.09.023. URL: http://dx.doi.org/10.1016/j.solener.2015.09.023.

[7] Pacio, J., Singer, C., Wetzel, T., and Uhlig, R. “Thermodynamic evaluation of liquid metals as heat transfer fluids in concentrated solar power plants”. In: *Applied Thermal Engineering* 60 (2013), pp. 295–302.

[8] Sequeira, C. *Fundamentals of molten salt corrosion*. Switzerland, 2003.

[9] Mohan, G., Venkataraman, M., Gomez-Vidal, J., and Coventry, J. "Assessment of a novel ternary eutectic chloride salt for next generation high-temperature sensible heat storage". In: *Energy Conversion and Management* 167 (2018), pp. 156–164. ISSN: 01968904. DOI: 10.1016/j.enconman.2018.04.100.

[10] Mecheri, M. and Le Moullec, Y. "Supercritical CO2 Brayton cycles for coal-fired power plants". In: *Energy 103* (2016), pp. 758–771.

[11] Musgrove, G., Rimpel, A.M., and Wilkes, J.C. "Fundamentals of Supercritical CO2." In: *Symp., Supercrit. CO2 Power Cycle*. 2016.

[12] Rochau, G.E. *Supercritical CO2 Brayton cycle*. 2011.

[13] U.S. Department of Energy. "SunShot Vision Study". In: (2012). DOI: DOE/GO-102012-3037.

[14] William Penn, O. *Supercritical Carbon Dioxide Brayton Cycle Energy Conversion R &D Workshop*. 2014.

[15] Polimeni, S., Binotti, M., Moretti, L., and Manzolini, G. "Comparison of sodium and KCl-MgCl2 as heat transfer fluids in CSP solar tower with sCO2 power cycles". In: *Solar Energy* 162.January (2018), pp. 510–524. ISSN: 0038092X. DOI: 10.1016/j.solener.2018.01.046.

[16] Binotti, M., Astolfi, M., Campanari, S., Manzolini, G., and Silva, P. "Preliminary as- sessment of sCO2 cycles for power generation in CSP solar tower plants". In: *Applied Energy* (2017). URL: http://dx.doi.org/10.1016/j.apenergy.

[17] Iverson, B.D., Conboy, T.M., Pasch, J.J., and Kruizenga, A.M. "Supercritical CO2 Brayton cycles for solar-thermal energy". In: *Applied Energy* (2013), pp. 111, 957–970.

[18] Oko, C.O.C. *Engineering computational method: An algorithmic approach*. University of Port Harcourt Press, Port Harcourt.: 1st Edition, 2008.

[19] Eke, G B and Ebieto, Corresponding Author. "Performance Analysis of Shell and Tube Heat Exchangers : A case study". In: *Journal of Emerging Trends in Engineering and Applied Sciences* 3.5 (2012), pp. 899–903.

[20] Menendez, S.d.I.H. and Interviewee. *Experience on SGS maintenance*. 2017.

[21] Pelle, J.T., Sørensen, S.S., Soliman, H.A., and Larsen, S.L. *Lowering Levelized Cost of Energy (LCOE) with Technical and Commercial CSP Paradigms*. Tech. rep. Aalborg CSP - Changing Energy, 2019.

[22] Mochizuki, Hiroyasu and Takano, Masahito. “Heat transfer in heat exchangers of sodium cooled fast reactor systems”. In: *Nuclear Engineering and Design* 239.2 (2009), pp. 295–307. ISSN: 00295493. DOI: 10.1016/j.nucengdes.2008.10.013.

[23] Prakash, V., Thirumalai, M., Prabhakar, R., and Vaidyanathan, G. “Assessment of flow induced vibration in a sodium-sodium heat exchanger”. In: *Nuclear Engineering and Design* 239.1 (2009), pp. 169–179. ISSN: 00295493. DOI: 10.1016/j.nucengdes.2008.10.007.

[24] Prahlad, B., Kale, R. D., and Rajan, K. K. “Thermal Performance Tests on a Sodium-to-Sodium Heat Exchanger”. In: *Journal of Nuclear Science and Technology* 27.6 (1990), pp. 547–553. ISSN: 00223131. DOI: 10.3327/jnst.27.547.

[25] Aoto, Kazumi, Uto, Nariaki, Sakamoto, Yoshihiko, Ito, Takaya, Toda, Mikio, and Kotake, Shoji. “Design study and R&D progress on japan sodium-cooled fast reactor”. In: *Journal of Nuclear Science and Technology* 48.4 (2011), pp. 463–471. ISSN: 00223131. DOI: 10.1080/18811248.2011.9711720.

[26] NREL. *Concentrating Solar Power Projects*. 2013. URL: http://www.nrel.gov/csp/solarpaces/by%20technology.cfm.

[27] Bonilla, Javier, Calle, Alberto de la, Rodríguez-García, Margarita M., Roca, Lidia, and Valenzuela, Loreto. “Study on shell-and-tube heat exchanger models with different degree of complexity for process simulation and control design”. In: *Applied Thermal Engineering* 124 (2017), pp. 1425–1440. ISSN: 13594311. DOI: 10.1016/j.applthermaleng.2017.06.129.

[28] Bonilla, J., Rodrìguez-Garcìa, M.M., Roca, L., and Valenzuela, L. *Object-Oriented Modeling of a Multi-Pass Shell-and-Tube Heat Exchanger and its Application to Performance Evaluation*. Saint Petersburg, Russia, 2015.

[29] Du, Bao Cun, He, Ya Ling, Wang, Kun, and Zhu, Han Hui. “Convective heat transfer of molten salt in the shell-and-tube heat exchanger with segmental baffles”. In: *International Journal of Heat and Mass Transfer* 113 (2017), pp. 456–465. ISSN: 00179310. DOI: 10.1016/j.ijheatmasstransfer.2017.

05.075. URL: http://dx.doi.org/10.1016/j.ijheatmasstransfer.2017.05.075.

[30] González-Gómez, Pedro Ángel, Petrakopoulou, Fontina, Briongos, Javier Villa, and Santana, Domingo. “Steam generator design for solar towers using solar salt as heat transfer fluid”. In: *AIP Conference Proceedings* 1850 (2017). ISSN: 15517616. DOI: 10.1063/1.4984363.

[31] Incropera, Frank P. and Dewitt, David P. *Fundamentals of Heat Transfer*. 4th. Wiley, New York, 1981.

[32] Sinnott, R. K. *Coulson & Richardson’s Chemical Engineering: Chemical Engineering Design: Volume 6, 3rd Edition*. Butterworth-Heinemann, 1999. ISBN: 0 7506 4142 8.

[33] Thulukkanam, Kuppan. *Heat Exchanger Design Handbook, 2nd Edition*. CRC Press, 2013, pp. 237–336. ISBN: 9781439842126.

[34] TEMA. *Standards of the Tubular Exchanger Manufacturers Association, 8th Edition*. 25 North Broadway, Tarrytown, New York 10591, USA: Tubular Exchanger Manufacturers Association Inc., 1999.

[35] Saunders, E. A. D. “Features relating to thermal design”. In: *Heat Exchanger Design Handbook, Vol. 4*. Ed. by E. U. Schlunder. Washington, DC: Hemisphere, 1983, Section 4.2.5.

[36] Drake, C. E. and Carp, J. R. *Shell and tube heat exchangers*. Chemical Engineering, 1960, pp. 165–170.

[37] Palen, J. W. and Taborek, J. *Solution of shellside flow, pressure drop and heat transfer by stream analysis method*. Philadelphia: Chem. Eng., Symp. Ser., No. 92, Heat Transfer, 1969, pp. 53–63.

[38] Minton, P. E. “Process heat transfer”. In: *Proceedings of the 9th International Heat Transfer Conference*. Paper No. KN-22, 1990, Vol. 1, Jerusalem, Israel, 1990, pp. 355–362.

[39] Fanaritis, John P. and Bevevino, James W. “Designing Shell-and-Tube Heat Exchangers”. In: *Chemical Engineering (New York)* 83.14 (1976), pp. 62–71. ISSN: 00092460.

[40] Bott, T. R., Hewitt, G. F., and Shires, G. L. *Process Heat Transfer*. CRC-Press, 1994. ISBN: 0849399181.

[41] Shweta, Y Kulkarni, Jagadish, S. B., and Manjunath, M. B. “Analysis Comparing Performance of a Conventional Shell and Tube Heat Exchanger Using Kern, Bell and Bell Delaware Method”. In: *International Journal of Research in Engineering and Technology* 03.15 (2014), pp. 486–496. ISSN: 23217308. DOI: 10.15623/ijret.2014.0315093.

[42] Bell, K. J. “Delaware method for shellside design”. In: *Heat Transfer Equipment Design (R. K. Shah, E. C. Subbarao, and R. A. Mashelkar)*. Washington, DC: Hemisphere, 1988, pp. 145–166.

[43] Turton, Richard, Bailie, Richard C., Wallace B. Whiting, Joseph A. Shaeiwitz, and Debangsu Bhattacharyya. “Cost Equations and Curves for the CAPCOST Program”. In: *Analysis, Synthesis and Design of Chemical Processes*. 2012.

[44] Jenkins, Scott. “Chemical Engineering Plant Cost Index: 2018 Annual Value”. In: *Chemical Engineering* (Mar. 2019).

[45] González-Gómez, Pedro Ángel, Gómez-Hernández, Jesús, Briongos, Javier Villa, and Santana, Domingo. “Assessment of evaporators using solar salt as heat transfer fluid”. In: *AIP Conference Proceedings* 2033 (2018). ISSN: 15517616. DOI: 10.1063/1.5067051.

[46] Mikityuk, Konstantin. “Heat transfer to liquid metal: Review of data and correlations for tube bundles”. In: *Nuclear Engineering and Design* 239.4 (Apr. 2009), pp. 680–687. ISSN: 0029-5493. DOI: 10.1016/J.NUCENGDES.2008.12.014. URL: https://www.sciencedirect.com/science/article/pii/S0029549308006316?via%7B%5C%%7D3Dihub.

[47] Rodríguez-Sánchez, M.R., Soria-Verdugo, A., Almendros-Ibánez, J.A., Acosta-Iborra, A., and Santana, D. “Thermal design guidelines of solar power towers”. In: *Applied Thermal Engineering* 63 (2014), pp. 428–438.

[48] Zavoico, A. B. *Solar power tower design basis document, Tech. rept. SAND2001-2100 Rev 0*. Tech. rep. California.: Sandia National Laboratories, 2001.

[49] Holman, J. P. *Heat Transfer, 8th edn*. McGraw-Hill, Inc., 1997.

[50] Fernandes, P. J. L., Clegg, R. E., and Jones, D. R. H. “Failure by liquid metal induced embrittlement”. In: *Engineering Failure Analysis* 1 (1994), pp. 51–63.

[51] Armijo, Ken. *Design Basis for a 2.0MWth Liquid-HTF Pilot- Scale CSP System*. Presentation - Asia-Pacific Solar Research Conference, 2019.

[52] Haynes International Inc. *HAYNES® 230® alloy Principal Features*. 2019.

[53] Fous, O. J. "Sodium-NaK Engineering Handbook". In: I (1972), p. 339. URL: https://www.osti.gov/servlets/purl/4631555.

[54] M. Romero, J. González-Aguilar. "Next generation of liquid metal and other high-performance receiver designs for concentrating solar thermal (CST) central tower systems". In: *Advances in Concentrating Solar Thermal Research and Technology*. Ed. by Manuel J. Blanco and Lourdes Ramirez, Santigosa. Woodhead Publishing. ISBN: 9780080444017.

[55] Benoit, H, Spreafico, L, Gauthier, D, and Flamant, G. "Review of heat transfer fluids in tube- receivers used in concentrating solar thermal systems: properties and heat transfer coefficients". In: *Renewable and Sustainable Energy Reviews* 55 (2016), pp. 298–315.

[56] Cheng, X and Tak, N. "Investigation on turbulent heat transfer to lead-bismuth eutectic flows in circular tubers for nuclear applications". In: *Nuclear Engineering and Design* (2006), pp. 236–385.

[57] Towler, Gavin and Sinnott, Ray. *Legge Breast Unit.pdf*. 2013. ISBN: 9780080966595. DOI: 10.1016/B978-0-08-096659-5.00022-5. arXiv: arXiv:1011.1669v3.

Appendices

Appendix A

HX model

A.1 Temperature correction factor

The correction factor is a function of the shell and tube fluid temperatures, and the number of tube and shell passes. It is normally correlated as a function of two dimensionless temperature ratios:

$$R = \frac{T_1 - T_2}{t_2 - t_1} \tag{A.1}$$

$$S = \frac{t_2 - t_1}{T_1 - t_1} \tag{A.2}$$

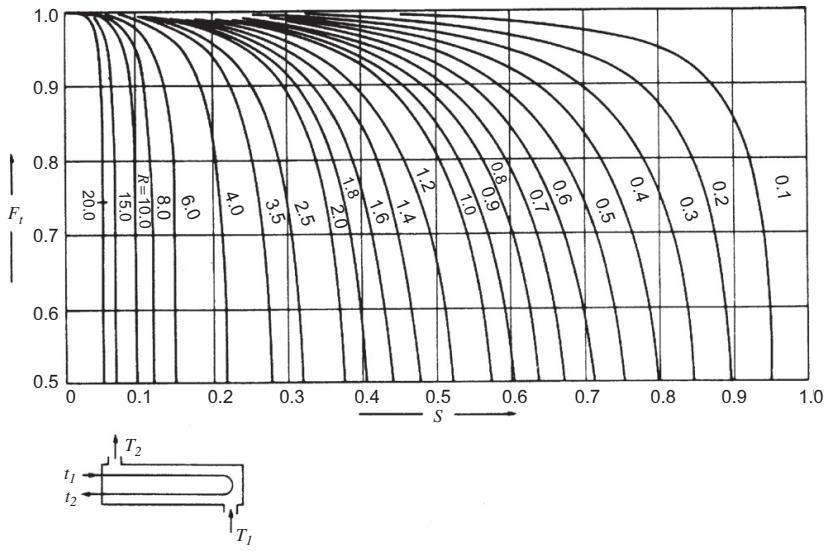

Figure A.1.1: Temperature correction factor: one shell pass, two or more even tube passes [57]

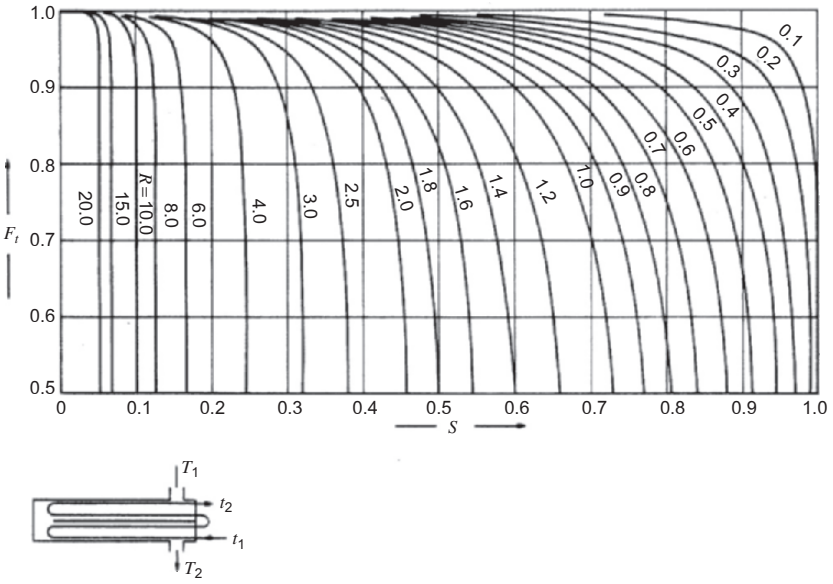

Figure A.1.2: Temperature correction factor: two shell passes, four or multiples of four tube passes [57]

A.2 Auxiliary shell-side calculations

Firstly, it is necessary to distinguish between ideal and real tube bundle flow. Theoretically, the shell-side fluid flows entirely across the tube bundle. In practice, there are several partial streams due to geometrical clearances and practical gaps between different components. Figure A.2.1 shows some of the stream distribution patterns.

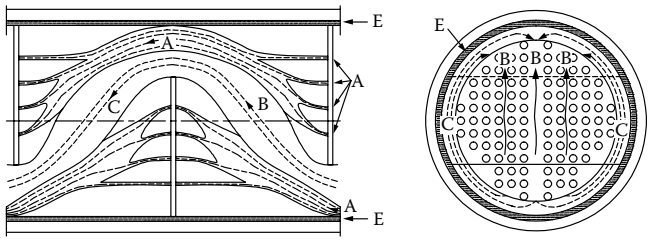

Figure A.2.1: Shell-side flow distribution patterns trough the tube bundle [33]

In details, the auxiliary calculations regard the following shell-side regions:

- Baffle window flow area;
- Shell-side crossflow area (*B stream*);
- Bundle-to-shell bypass area (*C stream*);
- Shell-to-baffle leakage area (*E stream*);

- Tube-to-baffle-hole leakage area (*A stream*).

Baffle window flow area: Figure A.2.2 shows the segmental baffle geometry. The parameters related to this region are presented and calculated in the following.

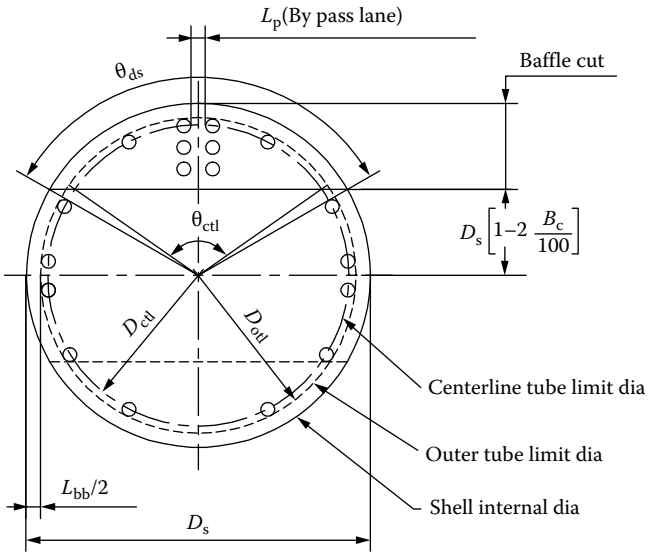

Figure A.2.2: Basic segmental baffle geometry [33]

The centriangle of baffle cut (θ_{ds}) can be calculated as indicated in equation (A.3).

$$\theta_{ds} = 2\cos^{-1}(1 - 2 \cdot B_c) \tag{A.3}$$

Instead, equation (A.4) provides the upper centriangle of baffle cut (θ_{ctl}).

$$\theta_{ctl} = 2\cos^{-1}\left(\frac{D_s - 2 \cdot L_c}{D_b}\right) \tag{A.4}$$

The gross window flow area (S_{wg}) can be calculated as indicated in equation (A.5).

$$S_{wg} = \frac{\pi}{4}\frac{D_s^2}{N_{sp}}\left(\frac{\theta_{ds}}{2\pi} - \frac{\sin(\theta_{ds})}{2\pi}\right) \tag{A.5}$$

From the upper centriangle of baffle cut, fraction of number of tubes in the baffle window (F_w) can be found (equation (A.6))

$$F_w = \frac{\theta_{ctl}}{2\pi} - \frac{\sin\theta_{ctl}}{2\pi} \tag{A.6}$$

Thus, the fraction of tubes in pure crossflow is given by equation (A.7)

$$F_c = 1 - 2F_c \tag{A.7}$$

The number of tubes in the window (N_{tw}) can be calculated (equation (A.8)) for a fixed number of tubes and using (A.6).

$$N_{tw} = N_t \cdot F_w \tag{A.8}$$

Thus, the segmental baffle window area occupied by the tubes (S_{wt}) can be found according to the following equation:

$$S_{wt} = \frac{N_{tw}}{N_{sp}} \frac{\pi}{4} d_o^2 \tag{A.9}$$

Using (A.5) and (A.9), the net crossflow area through one baffle window (S_w) results:

$$S_w = S_{wg} - S_{wt} \tag{A.10}$$

The number of effective tube rows in crossflow (N_c) can be calculated as follow:

$$N_c = \begin{cases} D_s \frac{1-2L_c/D_s}{P_t} & \text{if } square\ layout \\ D_s \frac{1-2L_c/D_s}{0.866 \cdot P_t} & \text{if } square\ layout \end{cases}$$

Consequently, the number of sealing strips per side (N_{ss}) can be calculated as:

$$N_{ss} = SS \cdot N_c \tag{A.11}$$

In the end, the number of effective tube rows in baffle window (N_{cw}) is given by:

$$N_{cw} = \begin{cases} \frac{0.8}{P_t}\left(L_c - \frac{D_s - D_b}{2}\right) & \text{if } square\ layout \\ \frac{0.8}{0.866 \cdot P_t}\left(L_c - \frac{D_s - D_b}{2}\right) & \text{if } triangular\ layout \end{cases}$$

Shell-side crossflow area: Stream B in figure A.2.1 shows the shell-side fluid flowing in crossflow through the tube bundle. The shell-side crossflow area can be calculated as:

$$S_m = \frac{l_b}{N_{sp}}\left(L_{bb} + \frac{D_b}{P_t}(P_t - d_o)\right) = \frac{l_b}{N_{sp}} \cdot L_{cf} \tag{A.12}$$

where L_{cf} is the crossflow free length.

Bundle-to-shell bypass area: Stream C in figure A.2.1 is the shell-side fluid flow through the the annular spaces between the tube bundle and the shell. Relevant parameters for this shell region are calculated in the following.

The bypass area between the shell and the tube bundle within one baffle (S_b) can be calculated as:

$$S_b = L_{bb}\frac{l_b}{N_{sp}} \tag{A.13}$$

The bypass correction factor (F_{bp}) is given by:

$$F_{bp} = \frac{S_b}{S_m} \tag{A.14}$$

Shell-to-baffle leakage area: The E stream, figure A.2.1, represents the stream due to the shell-to-baffle leakage, between the edge of a baffle and the shell. The shell-to-baffle leakage area is calculated as:

$$S_{sb} = \frac{\pi D_s}{N_{sp}}\frac{L_{sb}}{2}\left(\frac{2\pi - \theta_{ds}}{2\pi}\right) \tag{A.15}$$

Tube-to-baffle-hole leakage area: Stream A in figure A.2.1 is the shell-side fluid flow through the clearance between tubes and tube baffle holes. The tube-to-baffle-hole leakage area for one baffle is given by:

$$S_{tb} = \frac{N_t}{N_{sp}}\frac{\pi}{4}((d_o + L_{tb})^2 - d_o^2)(1 - F_w) \tag{A.16}$$

A.3 Heat transfer coefficient

A.3.1 Shell-side heat transfer coefficient

The segmental baffle window correction factor, J_C, is given by:

$$J_C = 0.55 + 0.72 \cdot F_c \tag{A.17}$$

where F_c is calculated in equation (A.7). In order to calculate the second correction factor, J_L, three parameters need to be calculated: r_{lm}, r_s, and x.

$$r_{lm} = \frac{S_{sb} + S_{tb}}{S_m} \tag{A.18}$$

$$r_s = \frac{S_{sb}}{S_{sb} + S_{tb}} \tag{A.19}$$

$$x = 0.8 - 0.15 \cdot (1 + r_s) \tag{A.20}$$

Thus, the correction factor for baffle leakage effects for heat transfer J_L is given by:

$$J_L = 0.44 \cdot (1 - r_s) + (1 - 0.44 \cdot (1 - r_s)) \cdot \exp\left(-2.2 \cdot r_{lm}\right) \tag{A.21}$$

In the end, the correction factors for bundle bypass effects for heat transfer J_B can be calculated according to equation (A.22).

$$J_B = \exp(-1.35 \cdot F_{bp} \cdot (1 - (2 \cdot r_{ss})^{1/3})) \tag{A.22}$$

where r_{ss} is the ratio N_{ss}/N_c.

A.4 Pressure losses calculation

A.4.1 Tube-side pressure drop

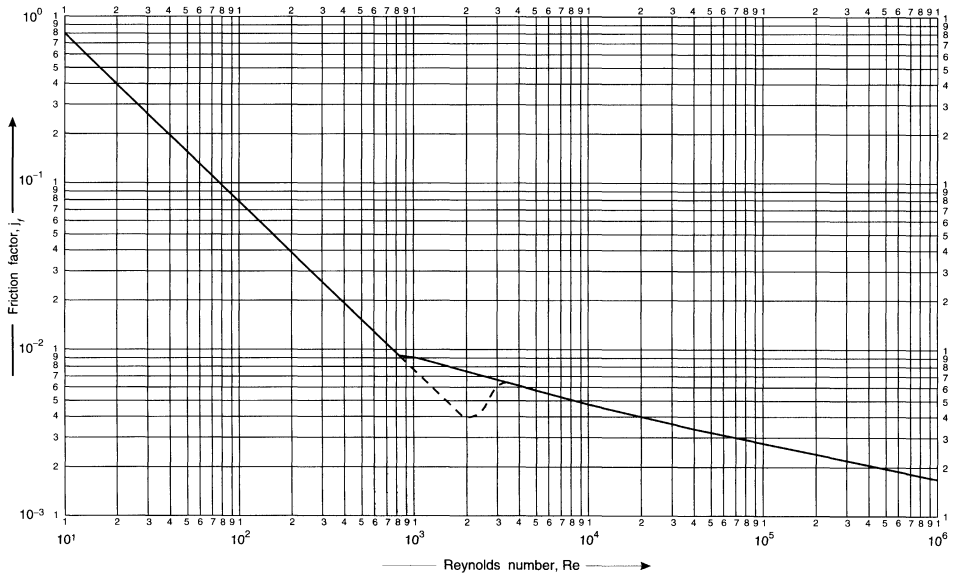

Figure A.4.1: Tube-side friction factor [32]

A.4.2 Shell-side pressure drop

$$R_B = \exp\left(-3.7 \cdot F_{bp} \cdot (1 - r_{ss}^{1/3})\right) \tag{A.23}$$

$$R_L = \exp\left(-1.33 \cdot (1 + r_s)\right) \cdot (r_{lm})^x \tag{A.24}$$

For square tube layout:

$$K_f = \begin{cases} 0.272 + \dfrac{0.207 \cdot 10^3}{Re} + \dfrac{0.102 \cdot 10^3}{Re^2} - \dfrac{0.286 \cdot 10^3}{Re^3} & \text{if } Re \leq 2300 \\ 0.267 + \dfrac{0.249 \cdot 10^4}{Re} - \dfrac{0.927 \cdot 10^7}{Re^2} + \dfrac{10^{10}}{Re^3} & \text{if } 2300 < Re \leq 2 \cdot 10^6 \end{cases} \tag{A.25}$$

For triangular tube layout:

$$K_f = \begin{cases} 11.474 \cdot Re^{-0.34417} & \text{if } Re \leq 4000 \\ 0.245 + \dfrac{0.339 \cdot 10^4}{Re} - \dfrac{0.984 \cdot 10^7}{Re^2} + \dfrac{0.133 \cdot 10^{11}}{Re^3} - \dfrac{0.599 \cdot 10^{13}}{Re^4} & \text{if } 4000 < Re \leq 2 \cdot 10^6 \end{cases} \tag{A.26}$$

A.5 Turton Cost Function: Material factor

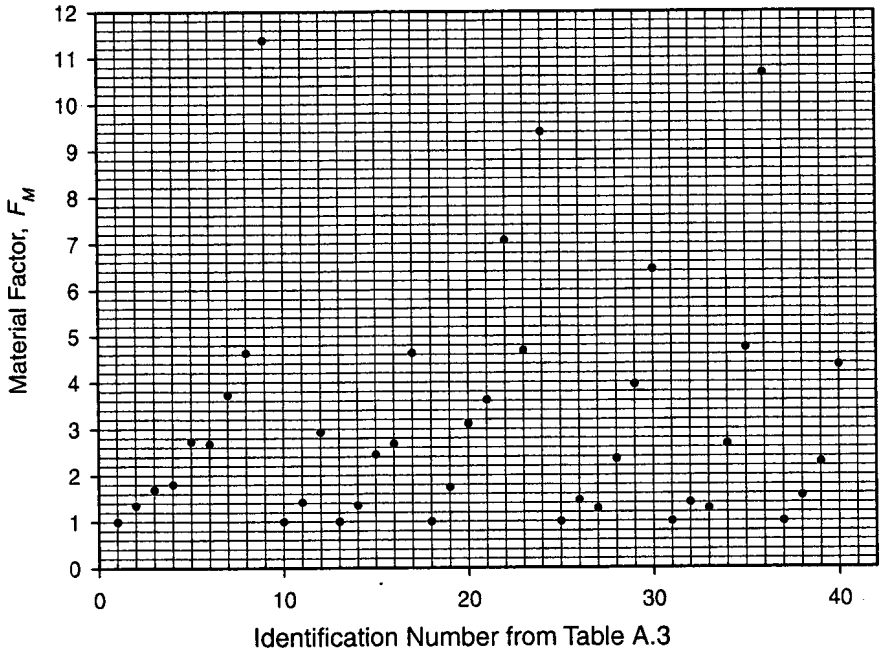

Figure A.5.1: Material Factors for Heat Exchangers in table A.5.2 [43]

Identification Number	Equipment Type	Equipment Description	Material of Construction
1	Heat exchanger	Double pipe, multiple pipe,	CS-shell/CS-tube
2		fixed tube sheet, floating head,	CS-shell/Cu-tube
3		U-tube, bayonet, kettle reboiler, scraped	Cu-shell/Cu-tube
4		wall, and spiral tube	CS-shell/SS-tube
5			SS-shell/SS-tube
6			CS-shell/Ni alloy tube
7			Ni alloy, shell/Ni alloy-tube
8			CS-shell/Ti-tube
9			Ti-shell/Ti-tube
10		Air cooler	CS tube
11		Air cooler	Al tube
12		Air cooler	SS tube
13		Flat plate and spiral plate	CS (in contact with fluid)
14		Flat plate and spiral plate	Cu (in contact with fluid)
15		Flat plate and spiral plate	SS (in contact with fluid)
16		Flat plate and spiral plate	Ni alloy (in contact with fluid)
17		Flat plate and spiral plate	Ti (in contact with fluid)

Figure A.5.2: Identification numbers for Material Factors for Heat Exchangers [43]

Appendix B

Sodium-Salt-sCO2 System Model

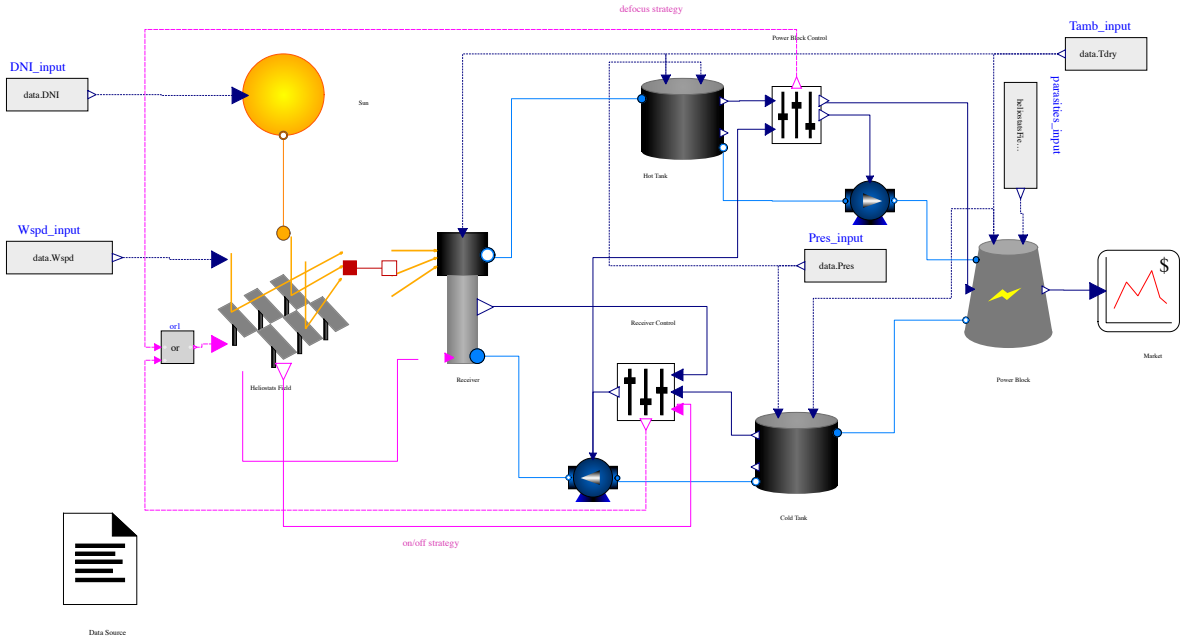

Figure B.1.1: Salt-sCO2 System

Appendix C

HX design definition

C.1 Tube-side fluid main properties

$$\rho = 219 + 275.32 \cdot \frac{1 - T}{2503.7} + 511.58 \cdot \left(\frac{1 - T}{2503.7}\right)^{0.5} \tag{C.1}$$

$$c_p = 1658.2 - 0.84790 \cdot T + 4.4541 \cdot 10^{-4} \cdot T^2 - 2.9926 \cdot 10^{-6} \cdot T^{-2} \tag{C.2}$$

$$\lambda = 124.67 - 0.11381 \cdot T + 5.5226 \cdot 10^{-5} \cdot T^2 - 1.1842 \cdot 10^{-8} \cdot T^3 \tag{C.3}$$

$$\ln(\mu) = -6.4406 - 0.3958 \cdot \ln\ (T) + \frac{556.835}{T} \tag{C.4}$$

C.2 Shell-side fluid main properties

$$\rho = -0.406 \cdot T + 1992.9 \tag{C.5}$$

$$c_p = -0.528 \cdot T + 1538.7 \tag{C.6}$$

$$\lambda = -0.0001 \cdot T + 0.5355 \tag{C.7}$$

$$\mu = a \cdot T^4 + b \cdot T^3 + c \cdot T^2 + d \cdot T + e \tag{C.8}$$

where $a = 1.685 \cdot (10)^{-13}$ $b = -6.577 \cdot (10)^{-10}$ $c = 9.764 \cdot (10)^{-7}$ $d = -6.590 \cdot (10)^{-4}$, and $e = 0.1745$.

C.3 HX material main properties

$$\rho = 8970 \tag{C.9}$$

$$\lambda = 0.01996 \cdot T + 2.981 \tag{C.10}$$

C.4 HX internal optimization

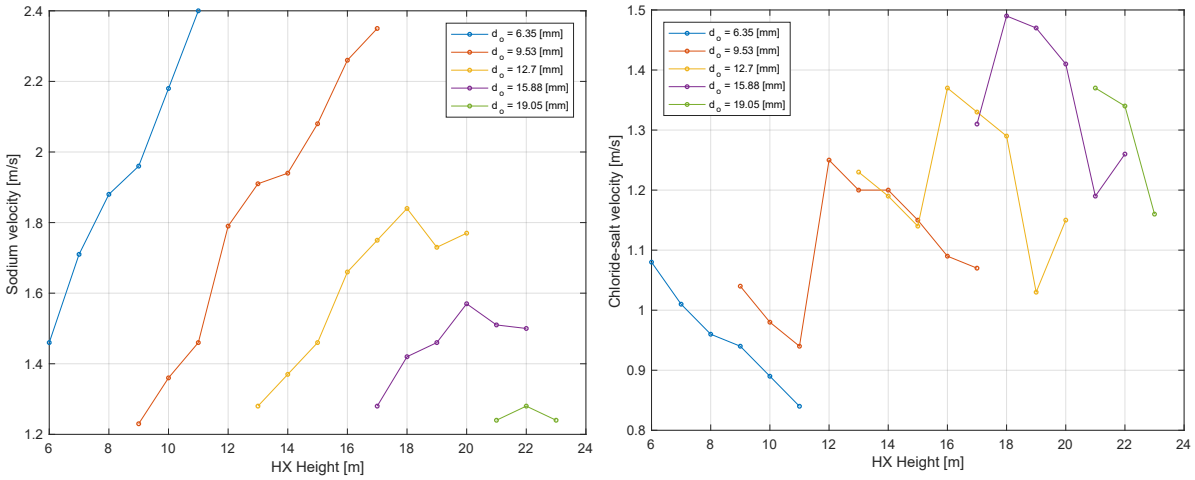

(a) Sodium velocity

(b) Chloride salt velocity

Figure C.4.1: Sodium velocity and chloride-salt velocity function of tube outside diameter, pass length and number of passes

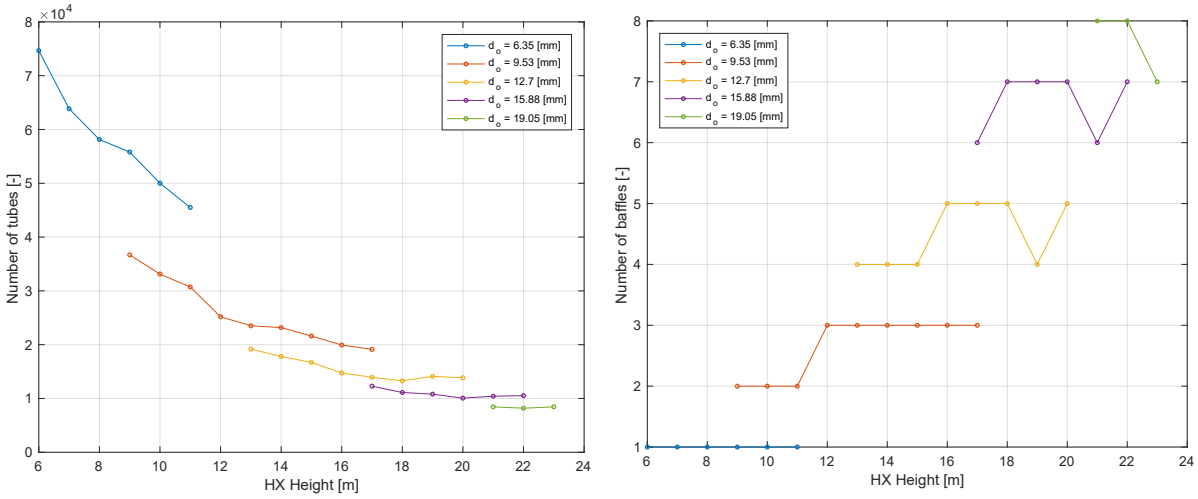

(a) Number of tubes

(b) Number of baffles

Figure C.4.2: Number of tubes and number of baffles function of tube outside diameter, pass length and number of passes

Appendix D

HX system-level optimization

D.1 HX Downsizing investigation

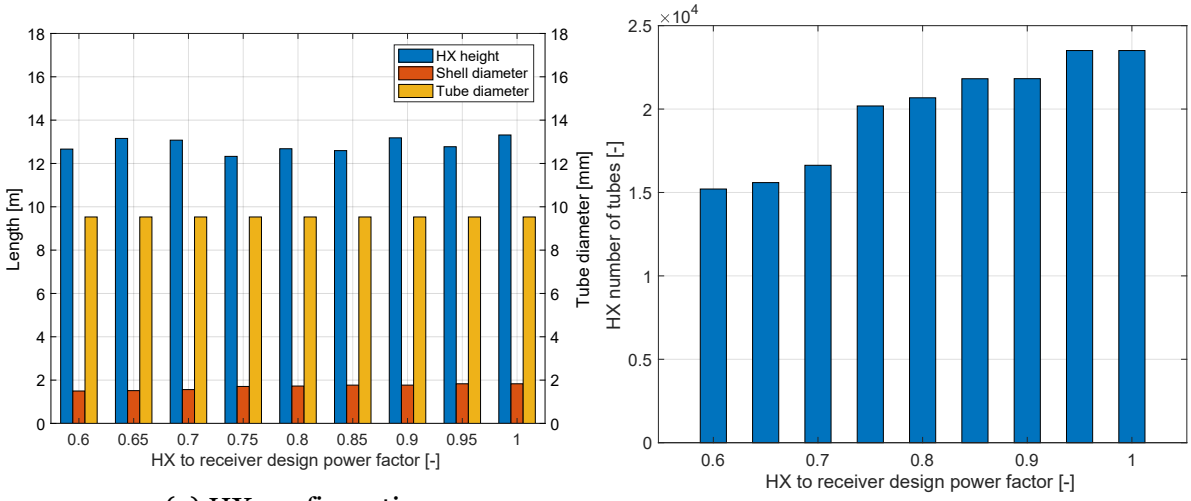

(a) HX configuration

(b) Number of tubes

Figure D.1.1: Tube outside diameter, shell diameter, tube pass length, and number of tubes as function of the DSF

D.2 LMTD optimization

D.2.1 Fixed inlet-outlet sodium temperature change

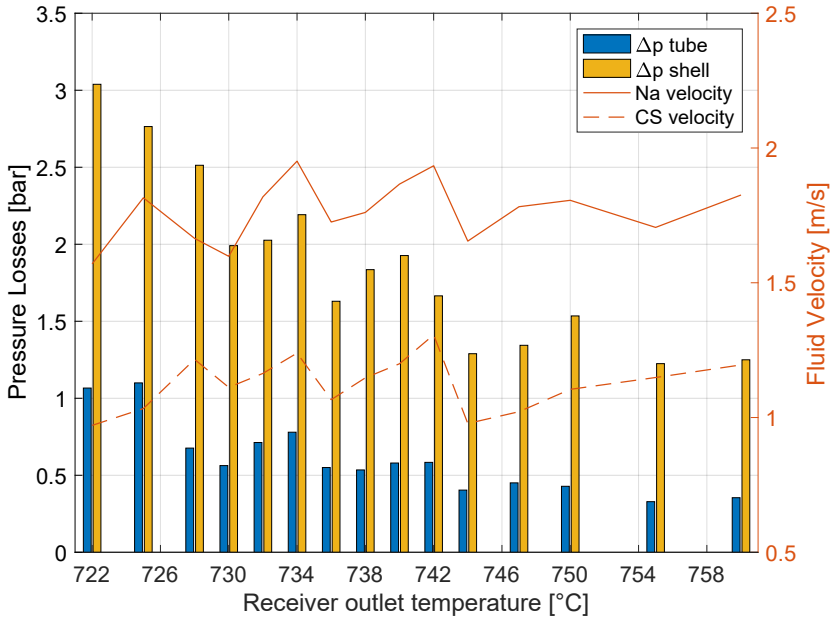

Figure D.2.1: Fluid velocities and pressure losses as function of the outlet receiver temperature

D.2.2 Variable inlet-outlet sodium temperature change

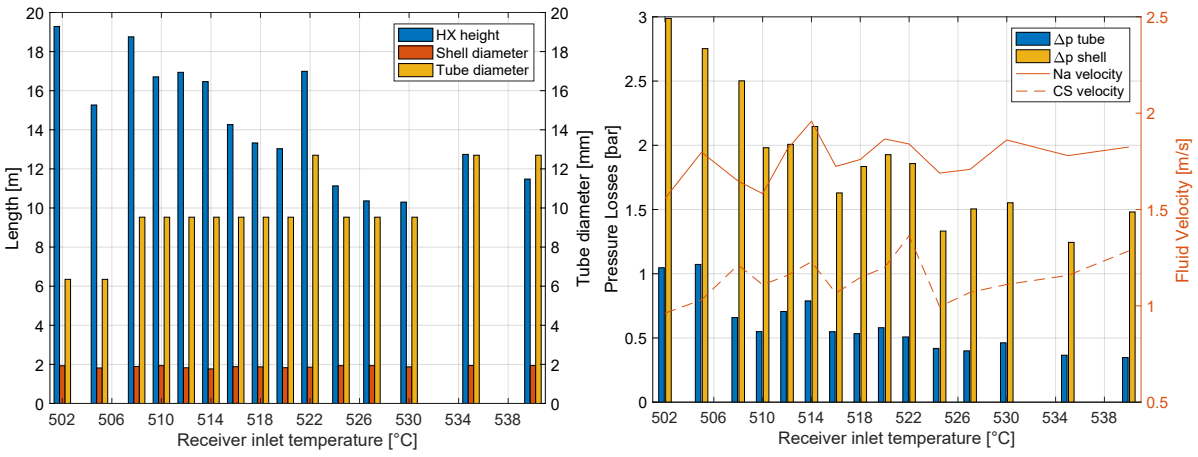

(a) HX configuration

(b) Fluid velocities and pressure losses

Figure D.2.2: HX configuration, fluid velocities, and pressure losses as function of the receiver inlet temperature

D.3 Maximum allowable flux on the receiver

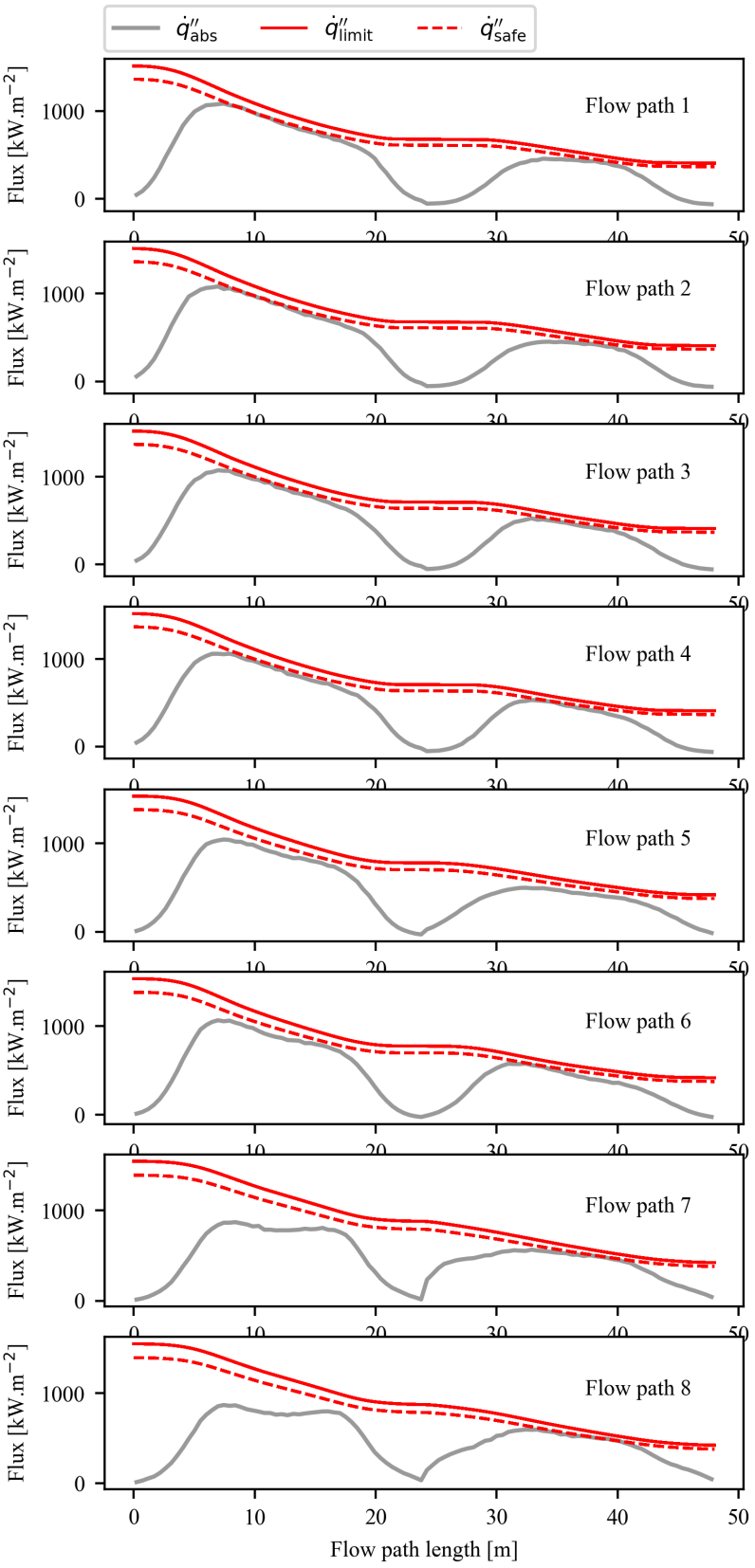

Figure D.3.1: Maximum allowable value as function of the flow path length and of the flow path type for the reference case

TRITA ITM-EX 2020:108

www.kth.se